uOttawa

L'Université canadienne
Canada's university

FACULTÉ DES ÉTUDES SUPÉRIEURES ET POSTOCTORALES

uOttawa

L'Université canadienne
Canada's university

FACULTY OF GRADUATE AND POSDOCTORAL STUDIES

Sébastien Blais
AUTEUR DE LA THÈSE / AUTHOR OF THESIS

M.A.Sc. (Electrical Engineeing)
GRADE / DEGREE

School of Information Technology and Engineering
FACULTÉ, ÉCOLE, DÉPARTEMENT / FACULTY, SCHOOL, DEPARTMENT

Design and Realization of a Bragg Grating Prism on Planar Integrated Optical Waveguides for Wideband Photonic True Time-Delay Beamforming.

TITRE DE LA THÈSE / TITLE OF THESIS

J. Yao
DIRECTEUR (DIRECTRICE) DE LA THÈSE / THESIS SUPERVISOR

CO-DIRECTEUR (CO-DIRECTRICE) DE LA THÈSE / THESIS CO-SUPERVISOR

EXAMINATEURS (EXAMINATRICES) DE LA THÈSE / THESIS EXAMINERS

J. Albert

P. Berini

Gary W. Slater
LE DOYEN DE LA FACULTÉ DES ÉTUDES SUPÉRIEURES ET POSTDOCTORALES /
DEAN OF THE FACULTY OF GRADUATE AND POSTDOCORAL STUDIES

Design and Realization of a Bragg Grating Prism on Planar Integrated Optical Waveguides for Wideband Photonic True Time-Delay Beamforming

By

Sébastien Blais

A thesis submitted in partial
fulfillment of the requirements for
the degree of

Master of Applied Science

Ottawa-Carleton Institute of Electrical and Computer Engineering
School of Information Technology and Engineering
Faculty of Engineering
University of Ottawa

August 2005

Your file Votre référence
ISBN: 0-494-11222-0
Our file Notre référence
ISBN: 0-494-11222-0

ABSTRACT

This thesis presents a simulation and experimental study of a true time-delay (TTD) beamforming network using a Bragg grating prism on Ge-doped silica-on-silicon planar integrated optical waveguide for application in phased array antennas (PAA). The Bragg grating prism is designed and fabricated on planar optical waveguides and the true time-delay beamforming module is implemented using the fabricated waveguide Bragg grating prism and other photonic components.

To implement the waveguide Bragg grating prism, several practical issues must be addressed. First, the fluence of the Bragg writing system and the photosensitivity of the optical waveguides must be adjusted so that Bragg gratings can be written in the waveguides. Second, coupling issues between a single mode fiber (SMF) and the waveguide must be addressed. In this thesis, the design of the waveguide is optimized in order to maximize the coupling between the fiber and the waveguide modes. A lensed fiber is used in order to couple light into the waveguide and to capture the light reflected from the Bragg gratings. Finally, since the waveguides are birefringent, the polarization state of the light must be carefully controlled.

Experimental results of the constructed waveguide Bragg grating prism are presented. The Bragg gratings are characterized and the time delays are measured for different microwave frequencies. The experimental results are then compared with the theory and a good

agreement is found between theory and experimental data. Radiation pattern of a four-element phased array antenna are simulated considering the measured time delays.

When dealing with a remotely controlled PAA, the dispersive properties of a standard single mode fiber must be taken under consideration. To this effect, a simulation study has been carried out and is detailed in this thesis. The Bragg grating prism used in the beamformer is composed of chirped gratings of different lengths but of same total chirp in order to produce a true time-delay progression. Two modulation techniques are considered, single sideband (SSB) and double sideband (DSB) modulation. SSB modulation is shown to be well suited for broadband operations with little impact on the orientation of the mainlobe resulting from chromatic dispersion.

ACKNOWLEDGEMENT

I would like to thank my supervisor, Dr. Jianping Yao, for his patience, support and guidance throughout this research project. I thank him for his valuable suggestions and for his guidance throughout my progression.

Part of this research has been carried out in collaboration with the Communications Research Centre of Canada. I am very grateful to Dr. Claire Callender who provided me with help, resources and her expertise. I also like to thank Patrick Dumais and Chris Ledderhof, also from the Communications Research Centre of Canada.

I am also thankful to the following people who have supported me and helped me, not only as coworkers, but also as friends: Mr. Fei Zeng, Mr. Zhichao Deng, Mr. Guohua Qi, Mr. Jun Wang and Mr. Howard Rideout.

Last, but certainly not least, I would like to thank my family and my fiancée, Karine. They were always behind me, looking over my shoulder, giving me support and encouragement.

TABLE OF CONTENTS

LIST OF FIGURES

LIST OF TABLES

LIST OF ACRONYMS

AF	Array Factor
APD	Avalanche Photodetector
BGP	Bragg Grating Prism
BPM	Beam Propagation Method
CRC	Communications Research Centre
DBR	Distributed Bragg Reflector
DFB	Distributed Feedback
DSB	Double Sideband
EMI	Electromagnetic Interference
EOM	Electro-Optic Modulator
FBG	Fiber Bragg Grating
IM	Intensity Modulation
IM/DD	Intensity Modulation/Direct Detection
MEMS	Micro-Electro-Mechanical Systems
MZM	Mach-Zehnder Modulator
PAA	Phased Array Antenna
PC	Polarization Controller
PD	Photodetector
PECVD	Plasma Enhanced Chemical Vapor Deposition
RF	Radio Frequency
RIE	Reactive Ion Etching

SMF	Single Mode Fiber
SSB	Single Sideband
TLS	Tunable Laser Source
TMM	Transfer Matrix Method
TTD	True Time Delay
UV	Ultraviolet
VCSEL	Vertical Cavity Surface Emitting Lasers

LIST OF PUBLICATIONS

1. S. Blais and J. P. Yao, "Effects of Chromatic Dispersion in a Waveguide Bragg Grating Prism Based True Time-Delay Beamforming Module," Oral presentation at the Canadian Conference on Electrical and Computer Engineering 2005, Saskatoon, Canada, May 2005.

2. S. Blais and J. P. Yao, "Simulation study of photonic true time-delay techniques using waveguide Bragg grating prism," Proceedings of SPIE, vol. 5577, pp. 784-792, Dec. 2004 (**Best poster award**).

3. S. Blais and J.P. Yao, "Single sideband modulation scheme employing an equivalent phase shifted Bragg grating for a remotely controlled photonic true time-delay beamforming system," Oral presentation at Photonics North 2005, Toronto, Canada, Sept. 2005.

Chapter 1

INTRODUCTION

1.1 Background review

High performance radars and wireless systems call for ever increasing beamforming capabilities as well as increasingly more challenging requirements concerning the size, weight and loss of the beamforming systems.

In high performance radar applications, high sensitivity, enhanced portability, increased performance of the receivers and exciters, improved resolution, large bandwidths and wider angular scans are primary areas of performance improvement [1-4]. Phased array antennas (PAA) play a key role in such applications as they provide low visibility, high directivity, beam pointing agility and dynamic beam pattern shaping [5-6]. The true time-delay (TTD) systems controlling these antennas need to answer many design constraints and performance requirements. The performance of a radar system is strongly related to its available bandwidth. In the electrical domain, this bandwidth is often limited to a few hundred megahertz. The acquisition and effective processing of multi-gigahertz radar signals is required to achieve improved range resolution [2] [7-9].

Given the recent massive expansion in wireless communication technology, the problems of interference, cost, maintainability, reliability and weight grow in importance. Solutions to

these problems may come in part from multiple functions provided by antennas, such as changes in carrier frequencies, bandwidths and radiation pattern [4] [10-11]. Such multifunction antennas rely on their controlling circuitry to meet their operational goals. This circuitry must be easily tunable and reconfigurable. Also, an ever increasing demand for higher data rates pushes the development of systems presenting a large available bandwidth. Other design challenges include low insertion losses, low power consumption, low production cost, light weight and small size [12].

The use of optical means to construct a true time-delay beamforming module has been extensively researched recently as it offers many obvious benefits [2] [3] [4] [5] [13-31]. For example, since the propagation of the optical signal is done via silica optical fibers, the system is immune to electromagnetic interference (EMI). Also, electrical microwave phase delay devices tend to be very bulky. Using optical fibers or optical waveguides can lead to small-size and light-weight systems which eases their implementation in airborne or satellite applications. Since many of the proposed configurations for optical beamforming modules employ true time delay modules, the instantaneous bandwidth is thus very large, which is a requirement for multi-frequency communication and radar systems. The use of true time-delay technique also solves the problem know as "beam squint" in which different microwave frequencies produce different radiation beams, leading to an important signal degradation and a broadening of the overall antenna beam. Finally, in the case of a remotely controlled phased array antenna, an optical signal sent through an optical fiber will suffer very low loss compared with electrical means as optical fibers present losses in the range of 0.2 dB/km.

The implementation of a photonics-based module to control phased array antennas also has some difficulties, mostly related to the development state of the technology. Since photonic technologies are not as mature as electrical techniques, fabricating a precise and reliable photonic TTD beamformer may be more difficult technologically and the costs associated with the development of such a module may be higher than for an electrical module. The packaging of the photonic module must be designed with precision in order to eliminate the influences of both temperature and mechanical vibration. As the technology matures, however, these limiting factors will become less significant and the advantages of a photonic approach over an electrical approach can be fully exploited.

In recent years, several configurations of photonic and optical true time-delay systems have been presented. Some systems used bulk optics [2] [32-34]. Such systems are bulky, sensitive to temperature changes, mechanical movement and vibration. Another configuration [27] uses optical heterodyne to generate and control the microwave signal. The instantaneous bandwidth of this system is limited since the configuration is not a true time-delay architecture. More recent configurations are using intensity modulation/direct detection (IM/DD) and serial or parallel delay lines [9] [19] [35-38]. Some systems using serial delay lines [19] [39] employ optical switches which only offer relatively low on/off ratios. This brings high losses and interchannel interference which degrades the performance of the system. Several IM/DD systems using parallel delay lines have been proposed in the past [8-9] [37]. One disadvantage of using parallel delay lines and an optical switching matrix comes from the fact that the optical fibers which transport the modulated optical signals and the electrical cables which transport the microwave signal must be of the same length. Failure to respect this condition will introduce a phase error in the recovered

microwave signal. Another technique utilizes wavelength dependent optical delay lines that produce relative delays among the different wavelengths due to optical path dispersion [1] [30] [40]. Finally, recent configurations employ Bragg gratings to achieve the required time delays [3] [14-19] [21-26] [29] [41-46]. Several configurations have been proposed. One configuration employs a multiple optical carriers and a chirped Bragg grating [16-17] [19] [23-24] [41]. The number of wavelengths in this system is equal to the number of antenna elements. In the proposed configuration, the wavelengths are generated by tunable laser sources. Instead of using multiple tunable laser sources, a multiwavelength tunable laser source can be used [41]. In both cases, Bragg gratings must be tuned mechanically either to produce the time delay progression or to filter out the unwanted wavelengths before the photodetector. Another true time-delay system employs a discrete fiber grating prism [3] [18] [29] [41-42] [45]. This allows discrete beamsteering at microwave frequencies less than 3 GHz. When the grating prism consists of chirped gratings [14] [21], continuous beam forming is possible at microwave frequencies up to 20 GHz [14]. One problem with these configurations is that they employ fiber Bragg gratings. Fiber Bragg gratings are known to be extremely sensitive to environmental changes, such as temperature and vibration, which affect greatly the performance of the TTD beamforming systems [47]. In addition, the fibers and the fiber Bragg gratings in the TTD beamforming systems are bundled manually, which increase the size and restricts the feasibility for mass production.

1.2 Objectives of this research project

In order to overcome the problems associated fiber Bragg grating prisms, techniques to produce Bragg grating prisms on Ge-doped silica-on-silicon planar integrated waveguides will be investigated. This will allow the development of more stable and more compact TTD beamforming systems for wideband phased array antenna applications. The enhanced stability can be achieved through proper packaging of the integrated device as its overall size is reduced when compared to the approach based on optical fibers. It is to be noted that the presented research projects includes many polarization controllers which contributes significantly to the overall size of the beamforming module based on a waveguide Bragg grating prism. Such devices would not be required if further integration of photonic components is carried out. This research project will focus on the theoretical and experimental investigation of the inscription of a discrete Bragg grating array for operation at microwave frequencies up to 3 GHz [18]. The optical and microwave properties of the prism will be characterized.

Firstly, the inscription of discrete grating prism using uniform gratings on silica-on-silicon planar waveguide will be investigated. A TTD system using the developed grating prism will be build. The Ge-doped SiO_2/Si waveguides will be fabricated using plasma-enhanced chemical vapour deposition (PECVD) and reactive ion etching (RIE). Ultraviolet (UV) inscription of the grating structures onto the waveguides will be implemented using the zero-order-nulled phased mask technique, which was invented at the Communications Research Centre (CRC). The prism produced at this stage will be characterized in terms of accuracy,

stability and tunability. Other issues such as the coupling between the waveguides and optical fibers will also be investigated.

A theoretical study of the effects of chromatic dispersion on the true time-delay beamforming system using a Bragg grating prism composed of chirped gratings will also be carried out. The effects of the chromatic dispersion induced by the single mode fiber will be considered. The true time-delay beamforming system considered is linked to the base station with a length of optical fiber such that the effects of chromatic dispersion induced by the fiber are considerable.

1.3 Major contributions

1. A photonic true time-delay system based on a waveguide Bragg grating prism is proposed. A simulation study of a Bragg grating prism constructed of chirped Bragg gratings strategically positioned in order to achieve quasi-continuous beam steering capabilities is developed. The effects of double- and single-sideband modulation on the performance of the system are studied. The effects of apodization of the gratings are also investigated.

2. A waveguide Bragg grating prism offering discrete true time-delay capabilities is fabricated and characterized. Ge-doped silica-on-silicon planar optical waveguides are designed and optimized by simulation and are developed. The fabrication of the Bragg gratings using a frequency-doubled argon ion laser emitting at 244 nm is investigated and pursued. Hydrogen loading is found to increase the photosensitivity of the waveguides

enough to write gratings. The time delays are measured using a microwave network analyzer.

3. Dispersion effects on the performance of the waveguide Bragg grating based true time-delay module are discussed. It is demonstrated that the effects of chromatic dispersion are eliminated when a single-sideband modulation scheme is used. Double-sideband modulation is not well suited for a remotely controlled phased array antenna as the chromatic dispersion will induce important power penalties at discrete radio frequencies (RF) and also at discrete wavelengths.

1.4 Organization of this thesis

This thesis contains six chapters. Chapter 1 reviews the historical background of photonic true time-delay techniques and presents the motivations behind this research project. The objectives and the major contributions of this project are presented. In Chapter 2, the theory behind the photonic true time-delay module based on a waveguide Bragg grating prism is detailed. The theoretical model for linear phased array antennas is firstly presented, starting with a 2-element linear array and continuing to the more general case of an N-element linear array. The mathematical model of the waveguide Bragg grating is presented in this chapter. The optical properties of Ge-doped silica-on-silicon planar optical waveguides are introduced. Chapter 3 details the key components of the true time-delay beamforming module including optical source, electro-optic modulators and photodetector. In Chapter 4, a waveguide Bragg grating prism is implemented. The Bragg grating prism realized consists

of four delay lines with three uniform Bragg gratings on each line. The characterization of this Bragg grating prism is carried out. The parameters investigated include insertion losses, birefringence, and time-delay measurements. Radiation patterns of a phased array antenna are obtained based on the experimental time delays. The effects of chromatic dispersion on the performance of a remotely controlled phased array antenna with a photonic true time-delay beamforming module are introduced in Chapter 5. Two different modulation schemes are presented and their performances are discussed. Finally, conclusions are drawn in Chapter 6. Recommendations for future work are also given in this chapter.

Chapter 2

OVERVIEW

2.1 Phased array antennas

Antenna arrays are essentially a group of simple antennas called the array elements that are combined together to operate as a single antenna with a desired radiation pattern. The array elements may be many kind of antenna, such as dipoles, dielectric resonators or microstrip patches to only name a few. In order to shape the overall radiation pattern of the linked elements, several parameters can be controlled. These parameters include the number of elements in the array, the spatial location of each element with respect to the others, the orientation of each element as well as the parameters of the feed signals.

Since the feed signals parameters can be used to achieve a particular radiation pattern of the antenna array, it is then possible to dynamically control the shape of this radiation pattern. Furthermore, this control can be done without having any physical movement from the antenna. In other words, one possible extension of this is the possibility to scan the mainlobe of the radiation pattern without moving the antenna. This is the principle behind phased array antennas.

2.1.1 Two-elements array

Let us consider the case of an antenna array composed of two array elements as a simple theoretical case. The elements are spaced by a distance of d and are placed along the z-axis as shown in figure 2.1.

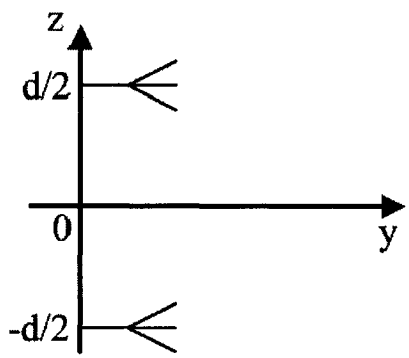

Fig. 2.1 Antenna array composed of two elements.

If we assume that each element is an isotropic source, i.e., the radiation pattern of each element is spherical with uniform amplitude, then the electric field of each element can be expressed as:

$$E = \frac{1}{r} e^{-j(kr+\beta)} \tag{1}$$

For the antenna array considered in Fig. 2.1, the total electric field in the far field would be the sum of the individual isotropic elements.

$$E = E_1 + E_2 = \frac{1}{r_1} e^{-j(kr_1+\beta/2)} + \frac{1}{r_2} e^{-j(kr_2-\beta/2)} \tag{2}$$

where r_1 and r_2 are defined in Fig. 2.2 and $\beta/2$ and $-\beta/2$ are the phase of the feed signals.

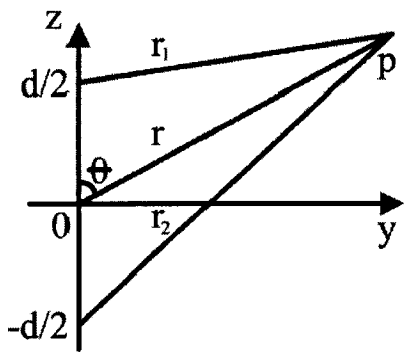

Fig. 2.2 Electric field in the far field.

In the far field, the following approximations can be made:

for the amplitude terms:

$$\theta_1 \approx \theta_2 \approx \theta \tag{3}$$

$$r_1 \approx r_2 \approx r \tag{4}$$

for the phase terms:

$$\theta_1 \approx \theta_2 \approx \theta \tag{5}$$

$$r_1 \approx r - \frac{d}{2}\cos(\theta), \quad r_2 \approx r + \frac{d}{2}\cos(\theta) \tag{6}$$

Thus, the total electric field in the far-field region can be expressed as

$$E = \frac{e^{-jkr}}{r}\left(2\cos(kd/2\cos(\theta)+\beta/2)\right) \tag{7}$$

The first part of this expression, $\frac{e^{-jkr}}{r}$, corresponds to the element pattern (for an isotropic source) and the second part is called the array factor. Thus, for antenna arrays, the total array pattern is the product of the element pattern and the array factor

$$\textit{Array Pattern} = \textit{Element Pattern} \cdot \textit{Array Factor} \tag{8}$$

In general, the array factor is considered alone when discussing antenna arrays. This is a way of "normalizing" the effect of the array regardless of the type of antenna used.

2.1.2 *N*-element linear array

The concept of a linear array can be extended from two elements to N elements. The elements are uniformly spaced and located at positions $(n\text{-}1)\,d$ for $n = 1, 2, 3, \ldots, N$ along the z axis. If each element is excited by a current I_n, then the array factor can be expressed as

$$AF = \sum_n AF_n = \sum_n I_n e^{j(n-1)kd\cos\theta} \tag{9}$$

If the exciting currents have a magnitude and phase given by

$$I_n = A_n e^{j\beta_n} \tag{10}$$

and if the phase β_n is linear with respect to n, it can be expressed as

$$\beta_n = (n-1)\beta \tag{11}$$

If the current has the same amplitude A for each element, the array factor can then be expressed as [48]

$$AF = A\sum_n e^{j(n-1)\psi} \tag{12}$$

where $\psi = kd\cos\theta + \beta$

The normalized amplitude of the array factor can thus be shown to be

$$af(\psi) = \frac{\sin(N\psi/2)}{N\sin(\psi/2)} \tag{13}$$

where the lowercase *af* represents a normalized value.

2.1.3 Planar array

It is possible to extend further more the concept of linear arrays to planar arrays. These arrays can be represented either as a linear combination of linear arrays (for a rectangular lattice) or as a combination of elements arranged in a regular pattern. These planar arrays present an even greater degree of control over the far-field pattern. The elements in planar arrays can be arranged in various configurations as depicted in Fig. 2.3.

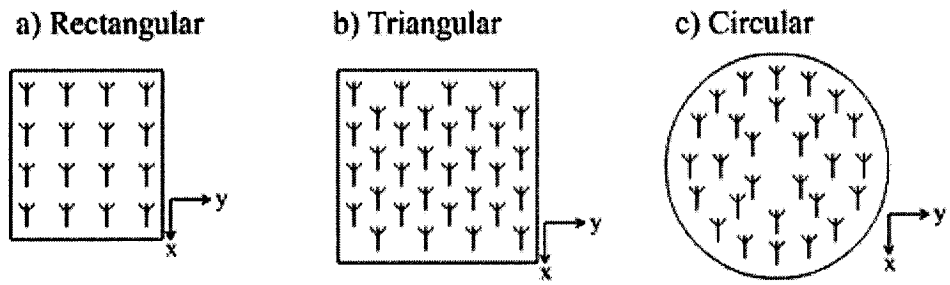

Fig. 2.3 Common disposition of planar array elements.

The most commonly used disposition for planar arrays is the rectangular lattice. For such a lattice, using the same principles as for the linear arrays, it can be shown that the normalized array factor can be expressed as [48]

$$af(\psi) = \frac{\sin(M \cdot \psi_x/2) \cdot \sin(N \cdot \psi_y/2)}{M \cdot N \cdot \sin(\psi_x/2) \cdot \sin(\psi_y/2)} \tag{14}$$

where $\psi_x = kd_x \sin\theta\cos\phi + \beta_x$ and $\psi_y = kd_y \sin\theta\sin\phi + \beta_y$.

Therefore, the radiation pattern of the overall array can be controlled by imposing different phase progressions along the x- and y-axis.

2.1.4 Far-field radiation pattern

In this report, only linear arrays will be considered in order to simplify the theory presented and still give a general overview of the behavior of phased array antennas. It has been demonstrated that the normalized array factor for such antennas is given by

$$af(\psi) = \frac{\sin(N\psi/2)}{N\sin(\psi/2)} \tag{15}$$

where $\psi = kd\cos\theta + \beta$. k is the wave number in free space (which is equal to $2\cdot\pi/\lambda$ and where λ is the free space wavelength). From the equations, the angle and the shape of the main beam of the antenna, θ, can be controlled by adjusting the distance between the antennas' array elements, the phase progression in the feed signals and by changing the number of elements. The following graph shows the influence of the distance between elements on the array pattern when there is no phase progression.

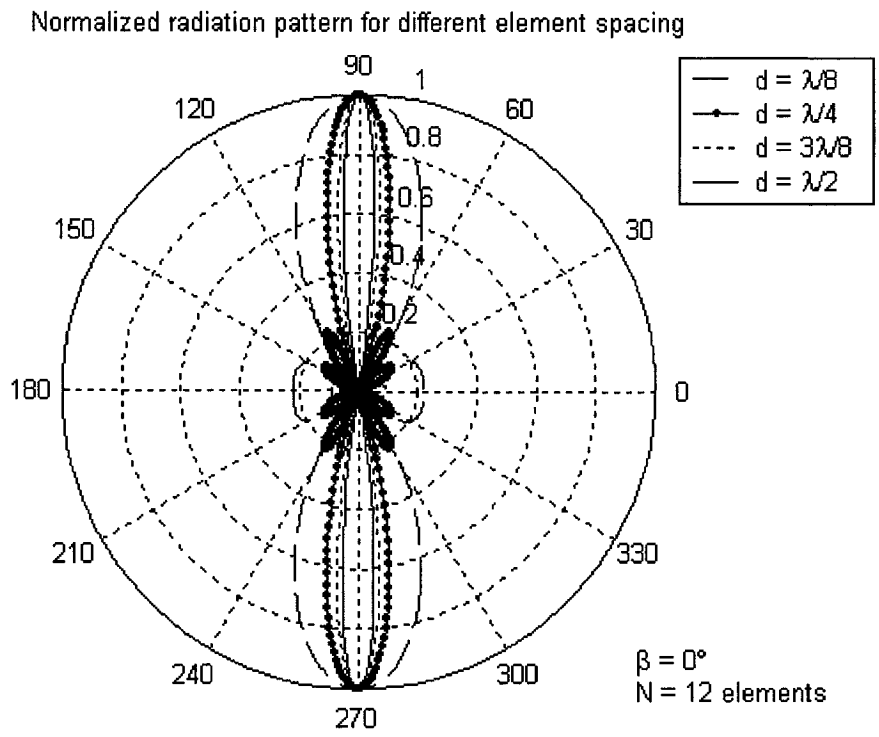

Fig. 2.4 Normalized radiation pattern for different element spacing ($\beta = 0°$, $N = 12$).

As can be seen, the spacing between elements influences only the directivity and the width of the mainlobe. This next graph shows the influence of the number of elements on the normalized far-field radiation pattern when there is no phase progression and when the spacing between elements is kept constant and equal to $\lambda/4$.

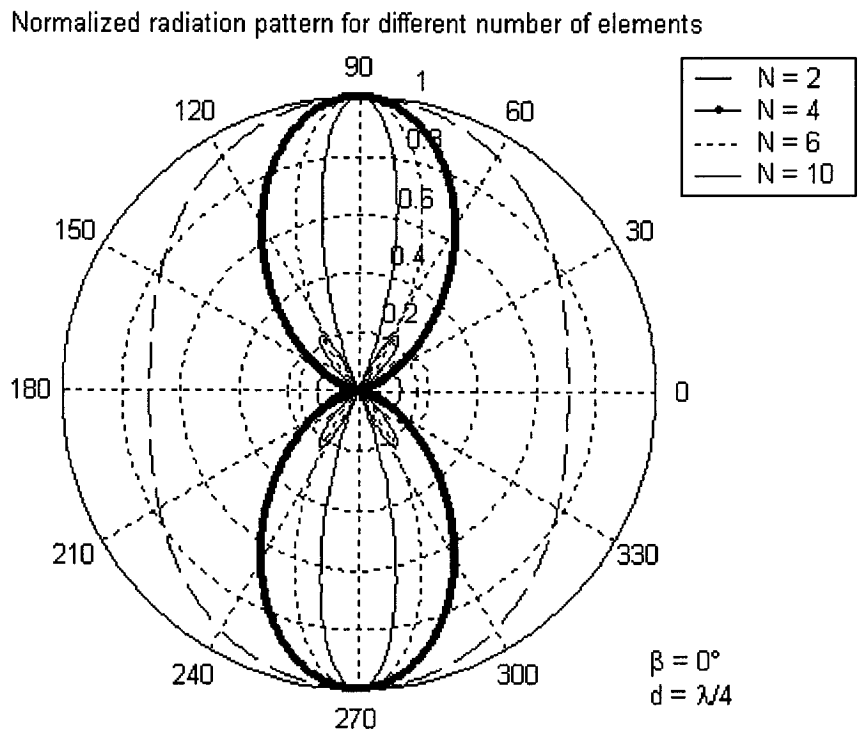

Fig. 2.5 Normalized radiation pattern for different number of elements ($\beta = 0°$, d = $\lambda/4$).

From Fig. 2.5, the number of elements also influences the overall shape of the radiation pattern and the directivity of the antenna and the width of the mainlobe. Along with the element spacing, the number of elements also plays a role in determining the number of sidelobes present in the array factor. This third graph shows the influence of the phase progression on the far-field radiation pattern when the number of elements and the distance between them are kept constant and equal to 12 and $\lambda/4$ respectively.

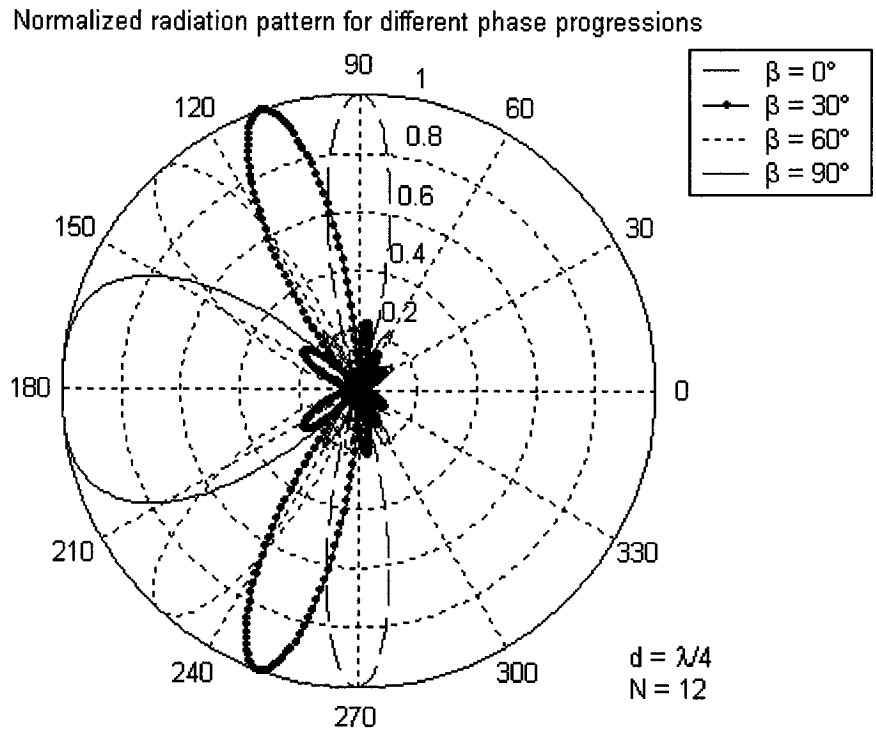

Fig. 2.6 Normalized radiation pattern for different phase progressions ($N = 12$, $d = \lambda/4$).

From Fig. 2.6, it is possible to see that the phase progression directly influences the position of the mainbeam with respect to the angle θ. Thus, for a fixed antenna (d and N constant), it is possible to scan the beam of the antenna by varying the phase progression of the feed signals for each element of the antenna.

2.1.5 True time delay

Phase shifters are components which adjust the appropriate phase of each feed signal going to the radiating elements of a phased array antenna. Different approaches to realizing such

components have been proposed and tested in the past (e.g., [10] [49-51]). Some of these approaches are very simple in nature while other are quite complex. A main criterion directly related to the complexity of the phase shifters is the tunability of such devices. In other words, the need to dynamically scan the mainlobe of the antenna radiation pattern increases the level of complexity required for the phase shifters.

Conventional phase shifters introduce a certain phase to the incoming signals regardless of the frequency of this signal. The above theory presented on phased array antennas were considering such devices as the phase progression β was considered constant for all frequencies.

One major drawback of this approach in realizing phased array antennas is a phenomenon known as "beam squint". This phenomenon is characterized by the position of the mainlobe of the array factor being oriented at different angles θ for different signal frequencies. In other words, the energy associated with different frequencies is oriented in different directions and thus restricts the use of the antenna for narrowband applications. The following graphs give an example of an antenna of 6 elements separated by a distance of 0.75 cm operating at a central frequency f_0 of 15 GHz. For the purposes of illustrating the beam squint effect, the bandwidth of the antenna will be assumed to be 10 GHz. Thus, the behavior of the antenna will be studied for the frequencies from 10 to 20 GHz.

The far-field radiation pattern of the array factor (considering isotropic elements) for the central frequency f_0 is given in Fig. 2.7.

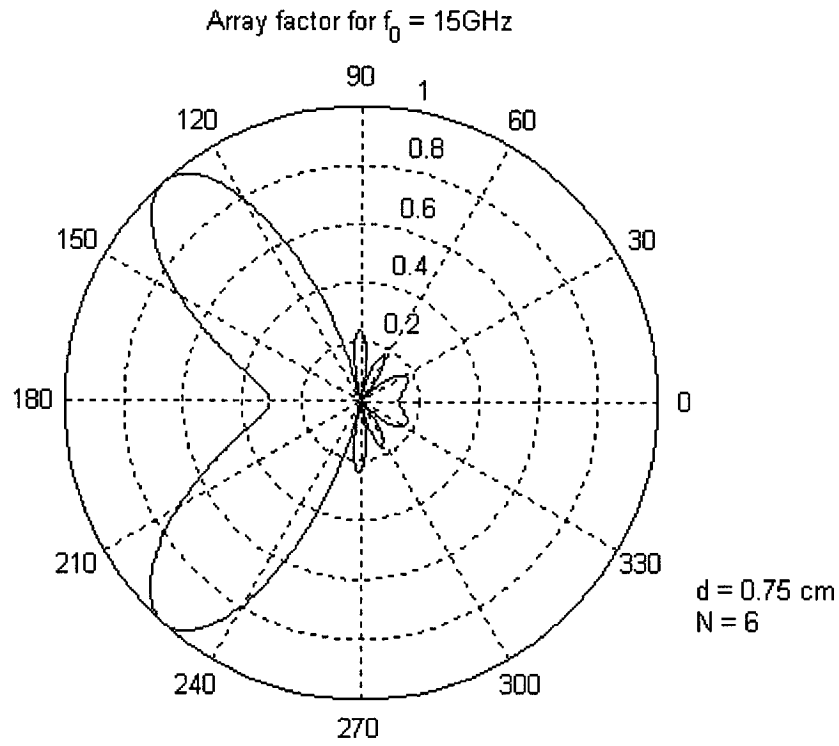

Fig. 2.7 Array factor for a PAA of 6 elements with d = 0.75 cm at f_0 = 15 GHz.

Fig. 2.8 illustrates the far-field radiation pattern of the array factor for frequencies between 10 and 20 GHz by intervals of 2 GHz for a phase progression of $\beta = \pi/2$.

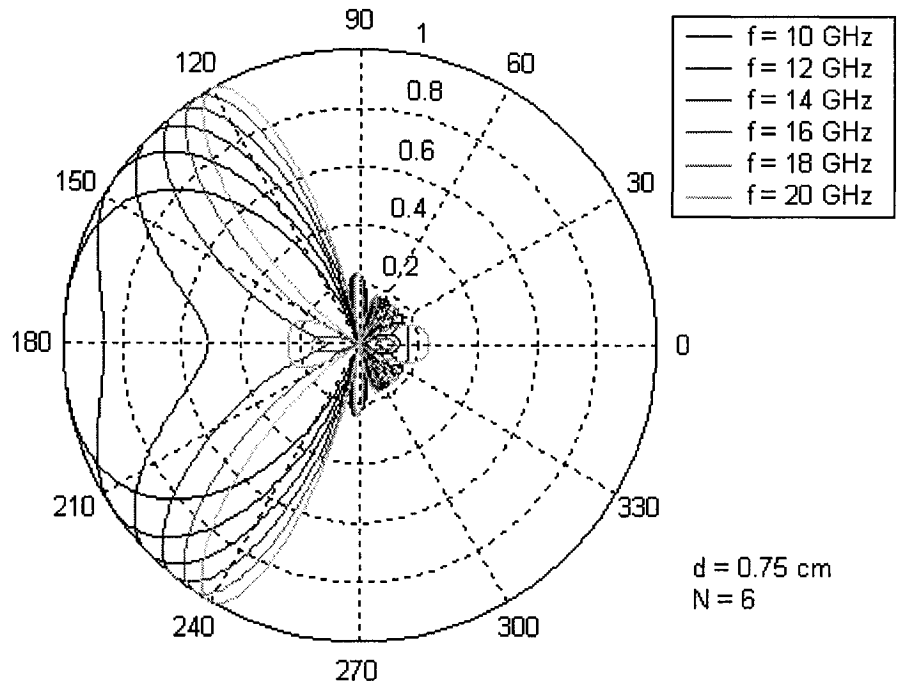

Fig. 2.8 Beam squint effect for a PAA operating at frequencies between 10-20 GHz.

From Fig 2.8, one can clearly see that the orientation of the mainlobe varies with the feed signal frequency. This phenomenon decreases significantly the performance of the overall system. The next figure resumes the beam squint effect by showing the orientation of the mainlobe for the frequency range 10-20 GHz for the PAA studied.

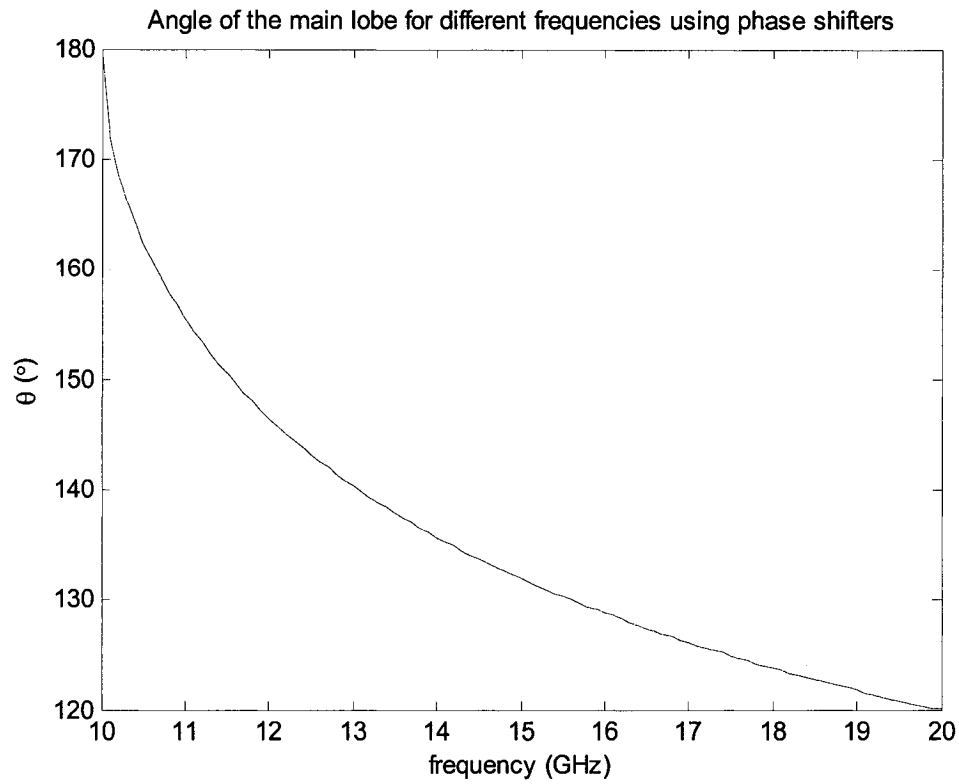

Fig. 2.9 Angle of the mainlobe for a PAA operating frequencies between 10-20 GHz.

From Fig. 2.9, it can be seen that the mainlobe orientation varies from approximately 120° to 180° over the range of frequencies observed.

A way to eliminate the beam squint is to use a method called true time-delay. This method consists of introducing a time delay Δt progression to the feed signals instead of a phase progression. This time delay is constant for all frequencies and thus translates into a variable phase shift with respect to frequency. In free space, this phase shift can be expressed as

$$\beta = 2 \cdot \pi \cdot f \cdot \Delta t \tag{16}$$

The following figures use the same PAA example as for the conventional phase shifters (N = 6 elements separated by a distance of 0.75 cm) operating at the same central frequency f_0 of 15 GHz. The behavior of the antenna is studied for the frequencies from 10 to 20 GHz. This time, true time-delays components are used instead of conventional phase shifters. These elements introduce a time progression of Δt = 16.67 ps which corresponds to the same phase of $\pi/2$ at a frequency of 15 GHz. Fig 2.10 illustrates the far-field radiation pattern of the array factor for frequencies between 10 and 20 GHz by intervals of 2 GHz which uses true time-delay components.

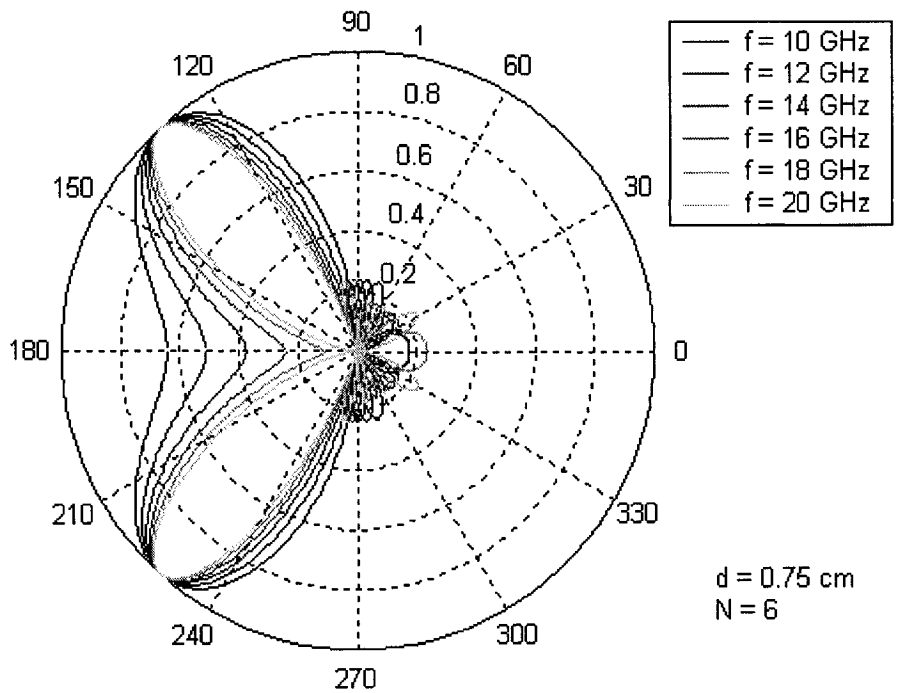

Fig. 2.10 Array factor of a PAA operating at frequencies between 10-20 GHz.

Fig. 2.10 clearly shows that the orientation of the mainlobe does not vary with the feed signal frequency. The next figure shows the orientation of the mainlobe for the frequency range 10-20 GHz for the PAA studied.

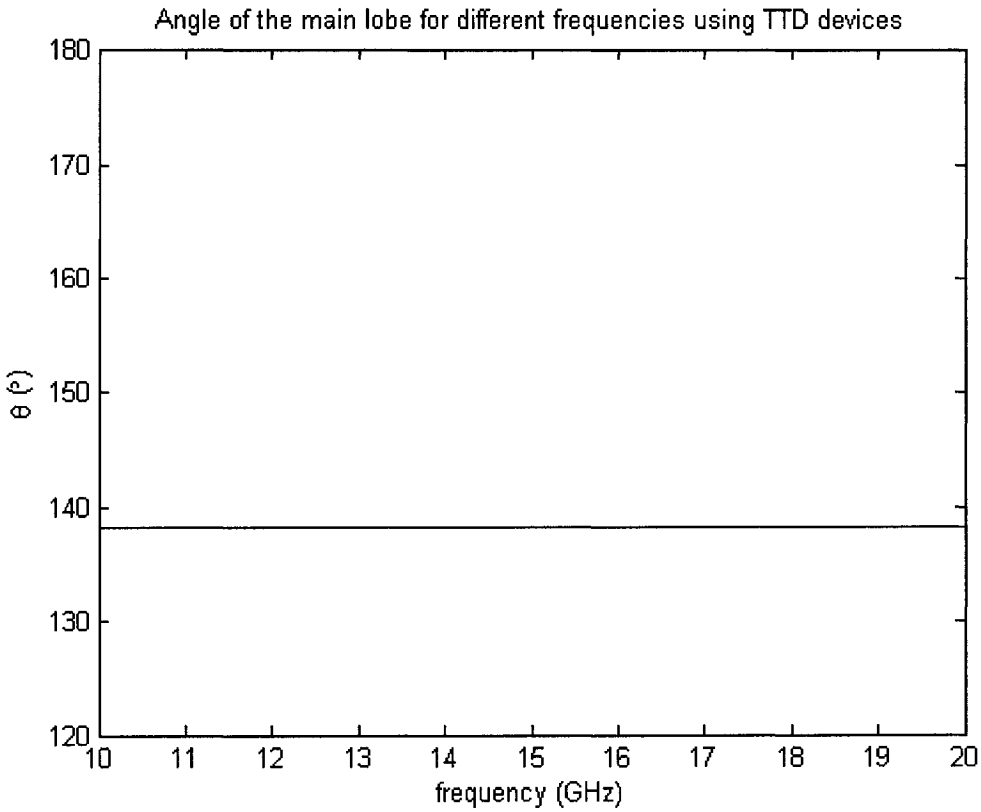

Fig. 2.11 Angle of the mainlobe for a PAA with TTD components at frequencies between 10-20 GHz.

The angle of the mainlobe stays at exactly the designed angle, 138°. This angle can be modified by adjusting the time delay accordingly. To find the time delay required for a certain angle, the following formula can be used

$$\Delta t = -\frac{d}{c}\cos(\theta) \tag{17}$$

where c is the speed of light in vacuum and d is the spacing between the antenna elements.

It can be noticed that the time delay required to orient the mainlobe of the antenna does not depend on the frequency, which proves furthermore that TTD components do not introduce "squint" in the far-field pattern of the antenna array.

2.1.6 Photonic true time delay

Traditionally, feed networks and phase shifters for phased array antennas were using microwave electronic components. This was the most intuitive approach since antennas work on an electrical driving source. With the advancement of technology, severe limitations were observed in electrical devices. For example, copper wires display high losses at high frequencies resulting in a limited bandwidth for the feed signals. Furthermore, electrical beamforming networks have a relatively high weight, thus limiting their use in airborne applications.

Optical components, with key advantages such as immunity to electromagnetic interference, low loss, small size and light weight (especially if integrated optics are used), are being considered as a promising alternative for wideband phased array antennas. Many photonic true time-delay techniques have been proposed in the past. An important criterion for a good true time-delay unit is the ability of tuning the time delay in order to steer the mainlobe of the antenna.

The true time-delay beamforming module considered in this research project uses a waveguide Bragg grating prism in order to delay the optical feed signals by a certain amount. The Bragg prism is composed of discrete Bragg grating delay lines, thus allowing discrete beamsteering capabilities. Chapter 3 will describe this technique in more details and present the theory associated with each component of this photonic true time-delay system.

2.2 Bragg gratings

Fiber Bragg gratings were discovered by Ken Hill and his coworkers at the Communications Research Centre in Ottawa, Canada in 1978 [52-54]. In 1989, an important breakthrough in its fabrication technique was made by Gerry Meltz and his coworkers [55]. The technique demonstrated by Meltz and his team uses interferometric superposition of ultraviolet beams coming from the side of the fiber. The angle between the beams allows controlling the Bragg wavelength. Another technique for fabricating Bragg gratings consists of the two ultraviolet beams being generated by exposing a periodic phase mask with a single UV

beam. The fabrication techniques for Bragg gratings will be discussed in further details in Section 2.2.2.

A fiber Bragg grating (FBG) can be defined as a section of an optical fiber where a perturbation of the refractive index exists at periodic intervals so that certain wavelengths are transmitted and others are reflected. Typical FBGs have grating periods of a few hundred nanometers, allowing coupling between counter-propagating modes of the optical fiber. Another type of FBGs is called long-period Bragg gratings [56]. Such gratings have periods in the order of hundreds of microns, coupling a core mode to cladding modes. In this case, the core mode and the cladding modes are propagating in the same direction. Since long-period gratings couple light to cladding modes, they are often fabricated with tilted grating planes in order to increase this coupling.

2.2.1 Mathematical model of Bragg gratings

The fiber Bragg gratings studied in this research project have grating periods of a few hundred nanometers and reflect light over a narrow wavelength range and transmit all other wavelengths. The center wavelength of reflection of such gratings is called the Bragg wavelength and is related to its period by

$$\Lambda = \frac{\lambda_B}{2 n_{eff}} \tag{18}$$

where Λ is the grating period, λ_B is the Bragg wavelength and n_{eff} is the mode effective refractive index of the optical waveguide.

Coupled-mode theory [57-60] is a powerful tool for obtaining quantitative information on the spectrum and phase of an FBG. A fiber Bragg grating fabricated in a single-mode fiber will see a mode of amplitude $A(z)$ be coupled into a counter-propagating mode of amplitude $B(z)$ near the Bragg wavelength. The coupled-mode theory equations may be simplified by retaining only terms that are related to the amplitudes of the two counter-propagating modes and neglect terms that contribute only slightly to the variations of the amplitudes. The resulting equations are the following [58]

$$\begin{aligned} \frac{dR}{dz} &= j\hat{\sigma} R(z) + j\kappa S(z) \\ \frac{dS}{dz} &= -j\hat{\sigma} S(z) - j\kappa^* R(z) \end{aligned} \tag{19}$$

where $R(z) = A(z)e^{j\delta z - \phi/2}$, $S(z) = B(z)e^{j\delta z + \phi/2}$, κ is the "ac" coupling coefficient and $\hat{\sigma}$ is a general "dc" self-coupling coefficient given by

$$\hat{\sigma} = \delta + \sigma - \frac{1}{2}\frac{d\phi}{dz} \tag{20}$$

where δ is the detuning and is independent of z for all gratings and is given by

$$\delta = \beta - \frac{\pi}{\Lambda} \tag{21}$$

where $\beta = \frac{2\pi\, n_{eff}}{\lambda}$ is the mode propagation constant. Substituting this in Eq. 21, we get

$$\delta = 2\pi\, n_{eff}\left(\frac{1}{\lambda} - \frac{1}{\lambda_B}\right) \tag{22}$$

The "ac" and "dc" coupling coefficients are given by

$$\sigma = \frac{2\pi}{\lambda}\overline{\delta n_{eff}} \tag{23}$$

$$\kappa = \kappa^* = \frac{\pi}{\lambda} v\,\overline{\delta n_{eff}} \tag{24}$$

where $\overline{\delta n_{eff}}$ is a "dc" index change spatially averaged over a grating period and v is the fringe visibility of the index change.

For a uniform grating, $\overline{\delta n_{eff}}$ is a constant and $\frac{d\phi}{dz} = 0$. Thus, from Eqs. 20, 23 and 24, σ, $\hat{\sigma}$ and κ are constants. In such a case, the amplitude reflection coefficient, ρ, for a Bragg grating of length L is given by

$$\rho = \frac{-\kappa \sinh\left(\sqrt{\kappa^2 - \hat{\sigma}^2}\, L\right)}{\hat{\sigma} \sinh\left(\sqrt{\kappa^2 - \hat{\sigma}^2}\, L\right) + j\sqrt{\kappa^2 - \hat{\sigma}^2} \cosh\left(\sqrt{\kappa^2 - \hat{\sigma}^2}\, L\right)} \tag{25}$$

The following figure shows a simulated response of a 4-mm long uniform FBG having an "ac" index change of 2×10^{-4}.

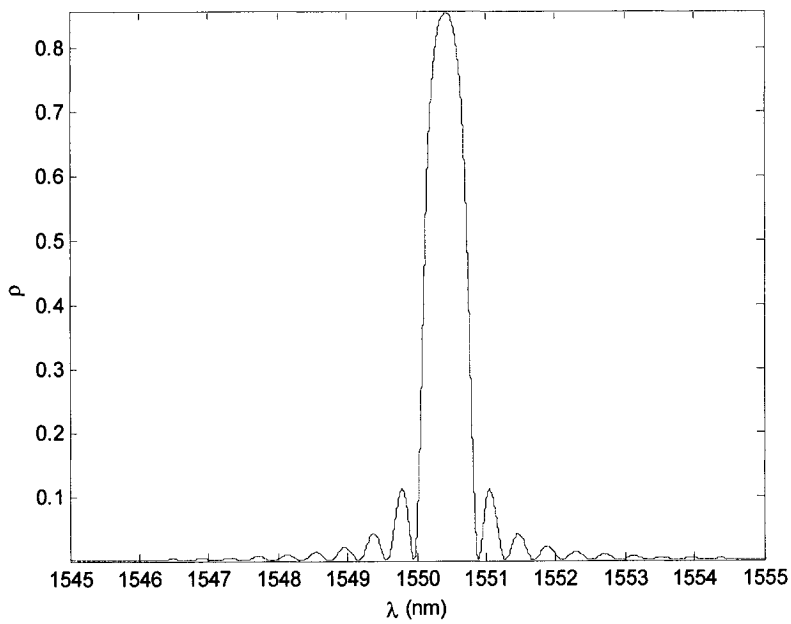

(a)

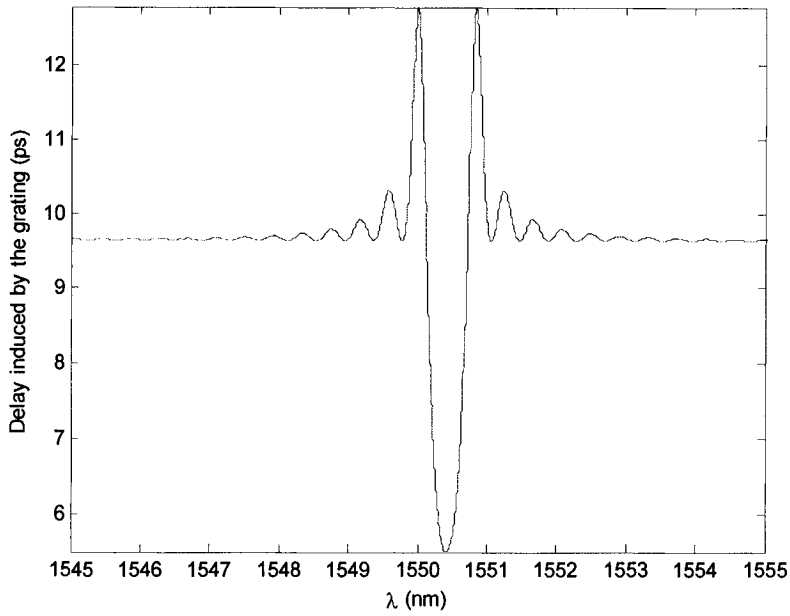

(b)

Fig. 2.12 Simulation results of the (a) reflection spectrum and (b) delay induced by a 4-mm long Bragg grating with an "ac" index change of 2×10^{-4}.

The delay induced by the Bragg grating is calculated by multiplying the derivative of the phase of the reflection coefficient with respect to the wavelength by $\lambda^2/(2\pi c)$.

In order to shape the spectral characteristics of an FBG, a technique called apodization can be used. Apodization consists of profiling the periodical perturbation in an optical waveguide such that the grating coupling coefficient varies spatially along its length [61-66]. Several apodization profiles (e.g. Gaussian, raised-cosine, sinc and more) can be used to reduce the sidelobes in the reflection spectrum [56] [67-68].

A uniformly-apodized Bragg grating begins and ends abruptly. Such a grating is also known as non-apodized. It can be expressed as a rectangular function of space. It is well known that the Fourier transform of a rectangular function yields a *sinc* function. Thus, a uniformly-apodized grating presents important sidelobes in its reflection spectrum. Knowing that the Fourier transform of a Gaussian function yields another Gaussian function which does not have any sidelobes, this characteristic can be exploited to produce a Gaussian-apodized Bragg grating with suppressed sidelobes [56] [69].

Apodization can also be beneficial in the dispersion characteristics of chirped Bragg gratings, which is a grating with nonuniform period along its length, by attenuating considerably a strong ripple present in the group delay of a uniformly-apodized chirped grating.

When considering apodization for a Bragg grating, if the refractive index modulation amplitude is simply changed without considering the average refractive index, a distributed Fabry-Perot interferometer is formed [70] and the Bragg wavelength is changed. This leads to an asymmetrical reflection spectrum which contains a Fabry-Perot resonance ripple on the short wavelength side. To avoid this complication, the average refractive index should be kept constant throughout the entire length of the Bragg grating. Fig. 2.13 shows the refractive index profile of a uniform Bragg grating, a Gaussian-apodized Bragg grating with simple refractive index modulation amplitude change and a Gaussian-apodized Bragg grating with a constant average refractive index. Fig. 2.14 shows the reflectivity of these gratings and Fig. 2.15 shows their group delays.

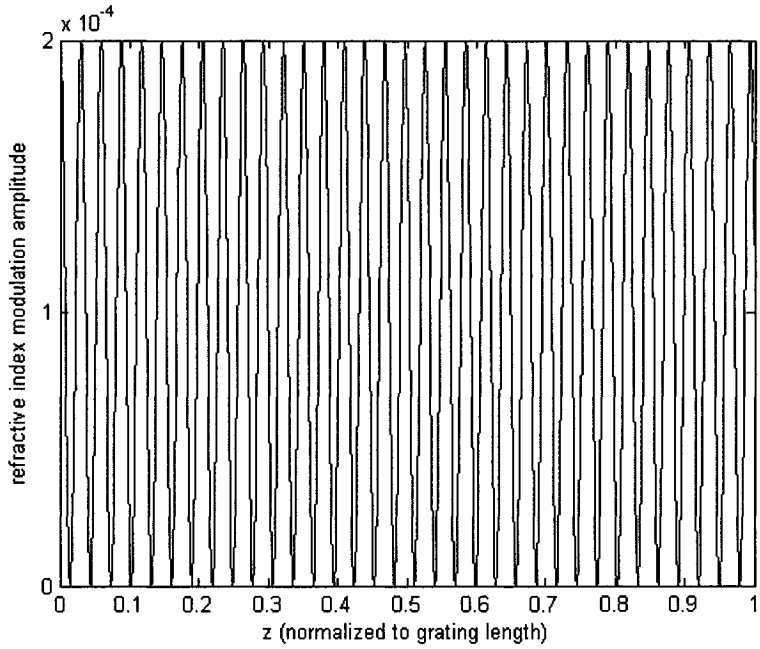
x 10^-4
2
1
0
refractive index modulation amplitude
0 0.1 0.2 0.3 0.4 0.5 0.6 0.7 0.8 0.9 1
z (normalized to grating length)

(a)

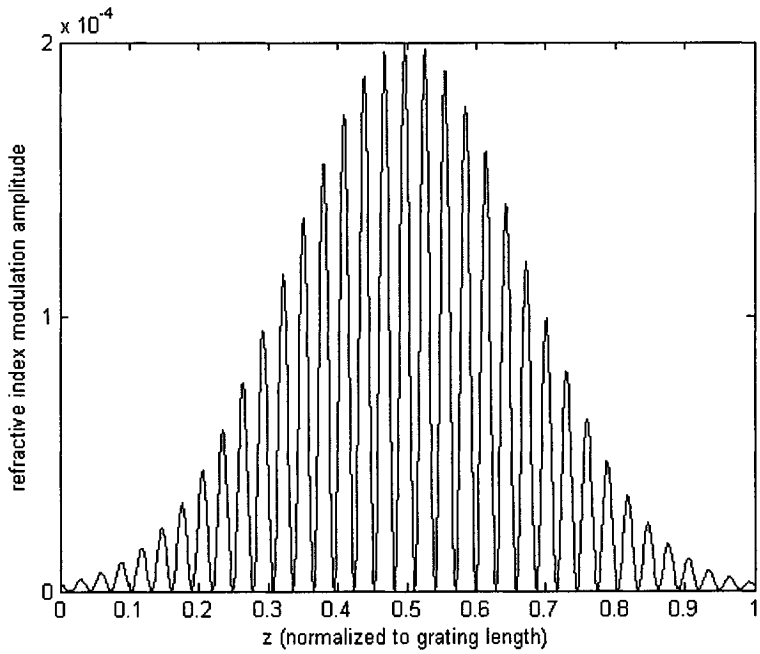
x 10^-4
2
1
0
refractive index modulation amplitude
0 0.1 0.2 0.3 0.4 0.5 0.6 0.7 0.8 0.9 1
z (normalized to grating length)

(b)

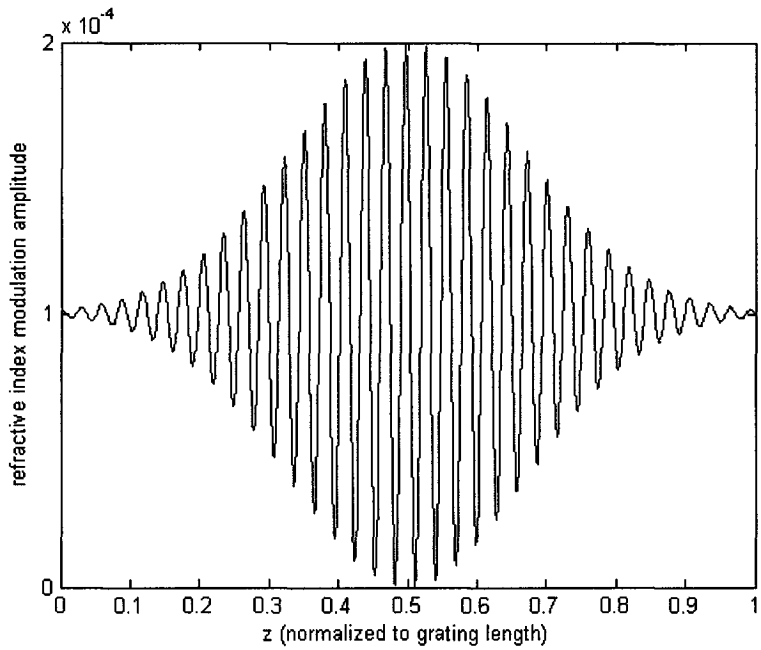

(c)

Fig. 2.13 Refractive index modulation amplitude of (a) a uniform Bragg grating, (b) a Gaussian-apodized Bragg grating with simple refractive index modulation amplitude change and (c) a Gaussian-apodized Bragg grating with a constant average refractive index with a modulation depth of 0.0002.

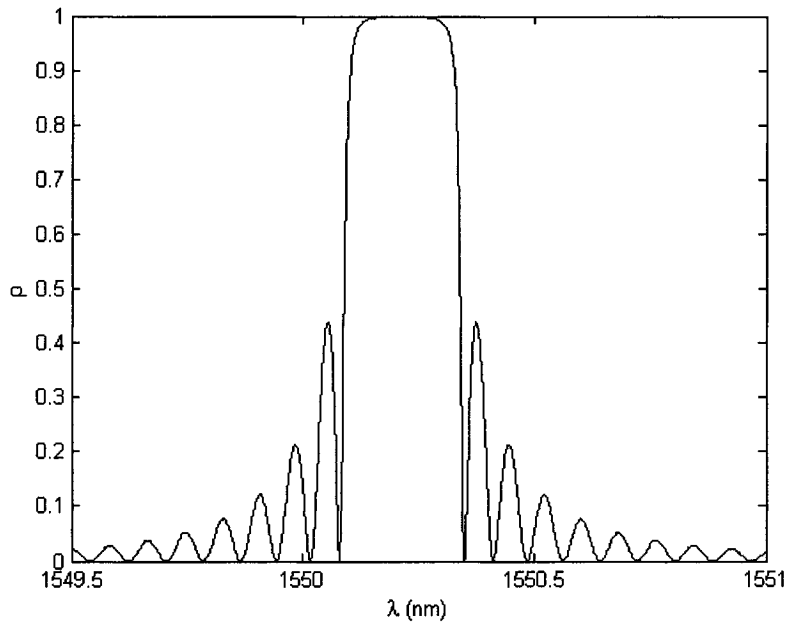
1
0.9
0.8
0.7
0.6
0.5
0.4
0.3
0.2
0.1
0
ρ
1549.5
1550
1550.5
1551
λ (nm)

(a)

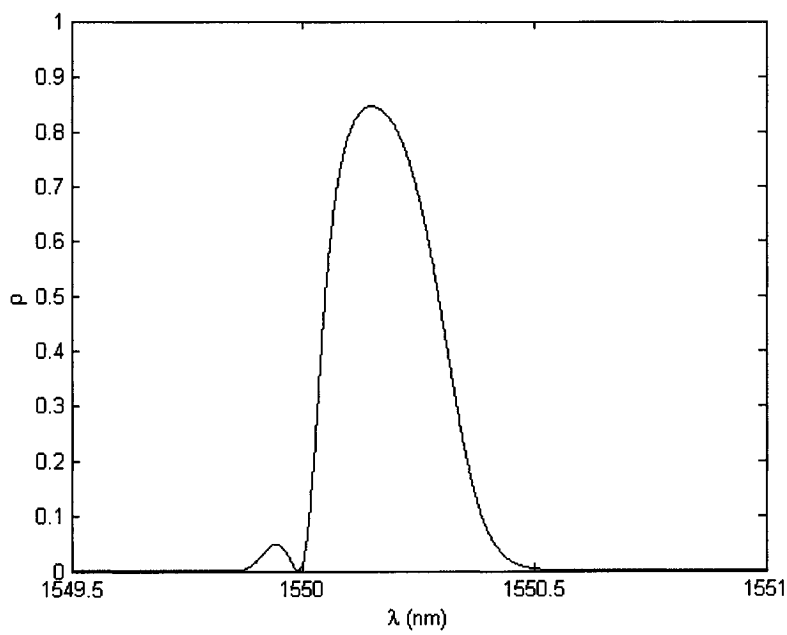
1
0.9
0.8
0.7
0.6
0.5
0.4
0.3
0.2
0.1
0
ρ
1549.5
1550
1550.5
1551
λ (nm)

(b)

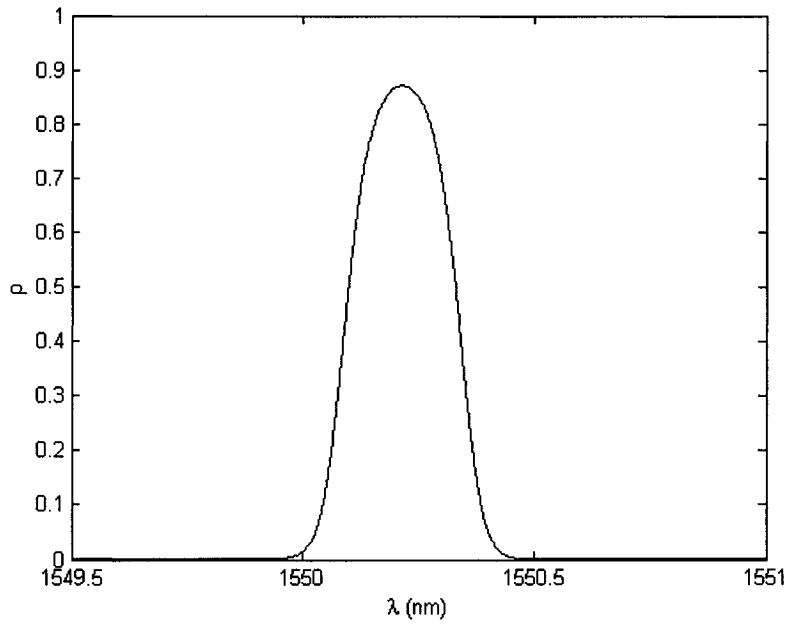

(c)

Fig. 2.14 Reflection spectrum of (a) a uniform Bragg grating, (b) a Gaussian-apodized Bragg grating with simple refractive index modulation amplitude change and (c) a Gaussian-apodized Bragg grating with a constant average refractive index.

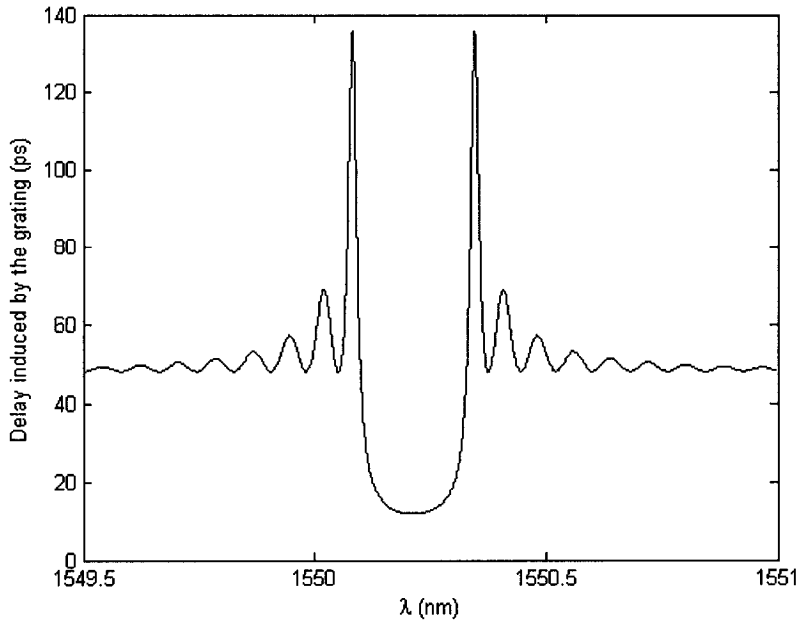
Delay induced by the grating (ps)
λ (nm)
140
120
100
80
60
40
20
0
1549.5
1550
1550.5
1551

(a)

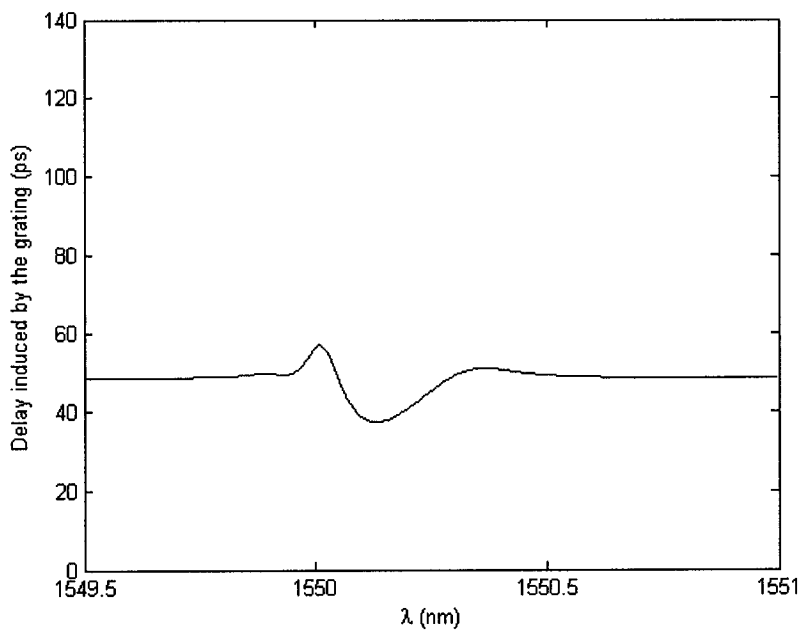
Delay induced by the grating (ps)
λ (nm)
140
120
100
80
60
40
20
0
1549.5
1550
1550.5
1551

(b)

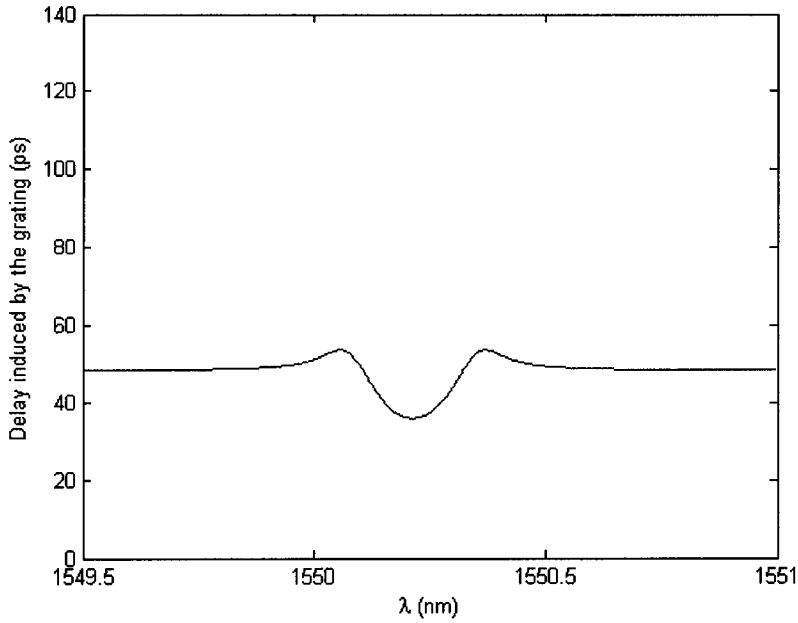

(c)

Fig. 2.15 Group delay of (a) a uniform Bragg grating, (b) a Gaussian-apodized Bragg grating with simple refractive index modulation amplitude change and (c) a Gaussian-apodized Bragg grating with a constant average refractive index.

When dealing with gratings having arbitrary coupling constant and chirp, no simple analytical solution exists. Also, these two variables cannot be separated as they collectively affect the transfer function of a given grating. For simulation purposes of the chirped gratings in this research project, the Transfer Matrix Method (TMM) is used [56] [71-73]. This method was first used by Yamada [73] in 1987 to analyze optical waveguides.

In this method, the coupled mode equations of a Bragg grating are used to calculate the output field of a short section of length δL of the grating. In this short section of grating, the period of the grating, $\Lambda(z)$, and the coupling constant, $\kappa(z)$, are assumed to be constant.

Thus, this short section of a grating can be considered as a uniform grating. This uniform grating can be viewed as a four-port device with two input- and two output-fields as depicted in Fig. 2.16.

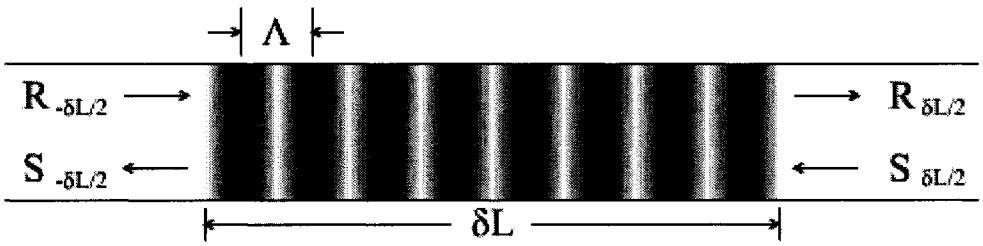

Fig. 2.16 Diagram representing the transfer matrix method principle for a uniform grating.

The section of grating can be expressed as a transfer matrix linking the two input and two output fields as

$$\begin{bmatrix} R_{\delta L/2} \\ S_{-\delta L/2} \end{bmatrix} = T \cdot \begin{bmatrix} R_{-\delta L/2} \\ S_{\delta L/2} \end{bmatrix} \tag{26}$$

The expression for the transfer matrix T, considering a uniform non-apodized grating of length δL is given by Eq. 27.

$$T = \begin{bmatrix} \cosh(\Omega \delta L) - i\frac{\hat{\sigma}}{\Omega}\sinh(\Omega \delta L) & -i\frac{\kappa}{\Omega}\sinh(\Omega \delta L) \\ i\frac{\kappa}{\Omega}\sinh(\Omega \delta L) & \cosh(\Omega \delta L) + i\frac{\hat{\sigma}}{\Omega}\sinh(\Omega \delta L) \end{bmatrix} \tag{27}$$

where $\Omega = \sqrt{\kappa^2 - \hat{\sigma}^2}$

The transfer matrix method can be used to solve non-uniform gratings. This method is effective in the analysis of the almost-periodic grating. A non-uniform Bragg grating can be divided into many uniform sections. Each section is described by its transfer matrix T_i as given in Eq. 27. The entire grating of length L is then approximated as the combined effect of all uniform sections as shown in Fig. 2.17.

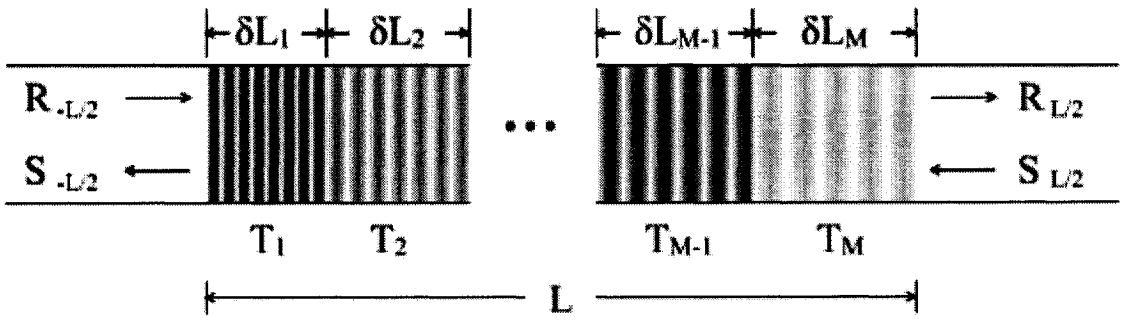

Fig. 2.17 Diagram showing the principle of the transfer matrix method for a non-uniform grating.

The entire grating can be approximated to be

$$\begin{bmatrix} R_{L/2} \\ S_{-L/2} \end{bmatrix} = T_M \cdot T_{M-1} \cdot \ldots \cdot T_2 \cdot T_1 \cdot \begin{bmatrix} R_{-L/2} \\ S_{L/2} \end{bmatrix} \tag{28}$$

When using the transfer matrix method, it is important to note that the number of sections, M, cannot be arbitrarily large. A section's length has to satisfy the slowly varying approximation, which requires that the amplitude of the mode change slowly over a distance of the wavelength of the light. Also, special care must be taken to ensure that each section contains an integer number of grating periods in order to have a smooth transition between sections. Not maintaining this condition can lead to a deleterious effect outside the bandwidth of the grating. Finally, when simulating long chirped gratings, care must be taken to allow adequate spectral resolution in order to calculate the group delay accurately.

The following figures give the simulation results of linearly chirped gratings without apodization and with a Gaussian apodization. Both gratings have a total chirp of 9 nm, which means that the periods of the grating at $z = 0$ and $z = L$, where L is the length of the grating, differ by 9 nm. Thus, the Bragg wavelength of this grating will differ by an amount equal to the multiplication of the total chirp by $2\, n_{eff}$.

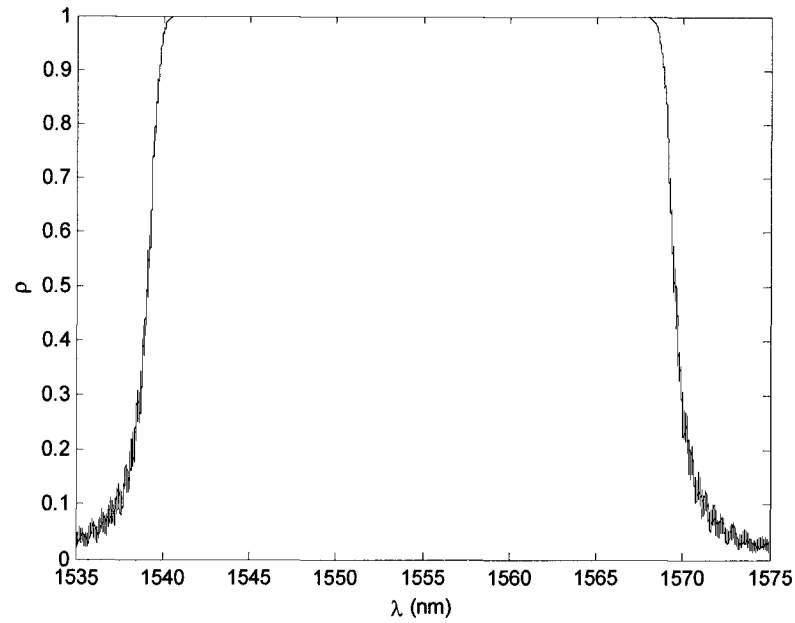

(a)

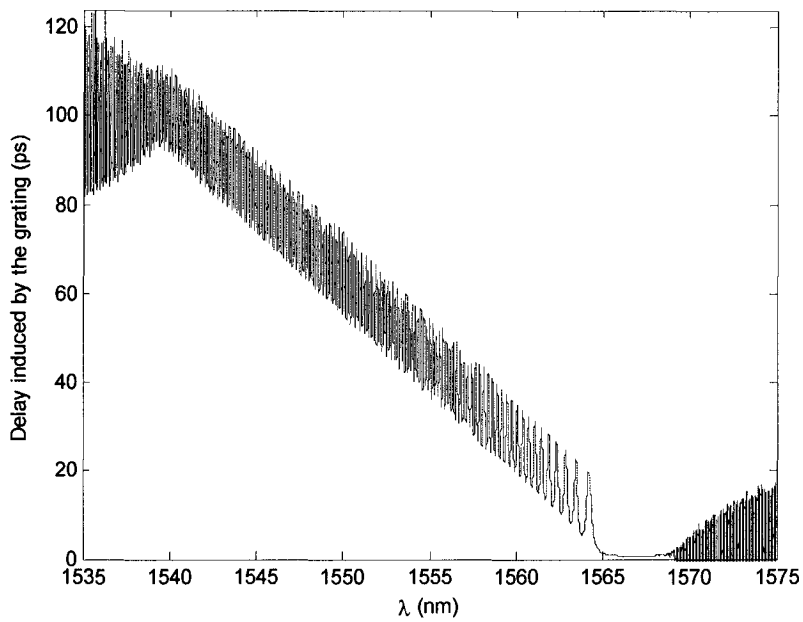

(b)

Fig. 2.18 Simulation results of the (a) reflection response and (b) delay induced by a 10-mm long chirped Bragg grating with total chirp of 9 nm.

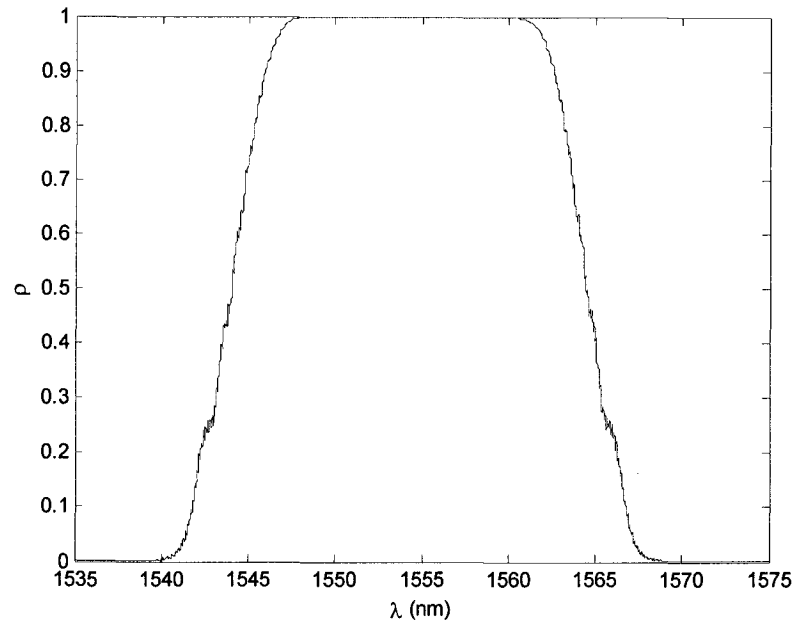

(a)

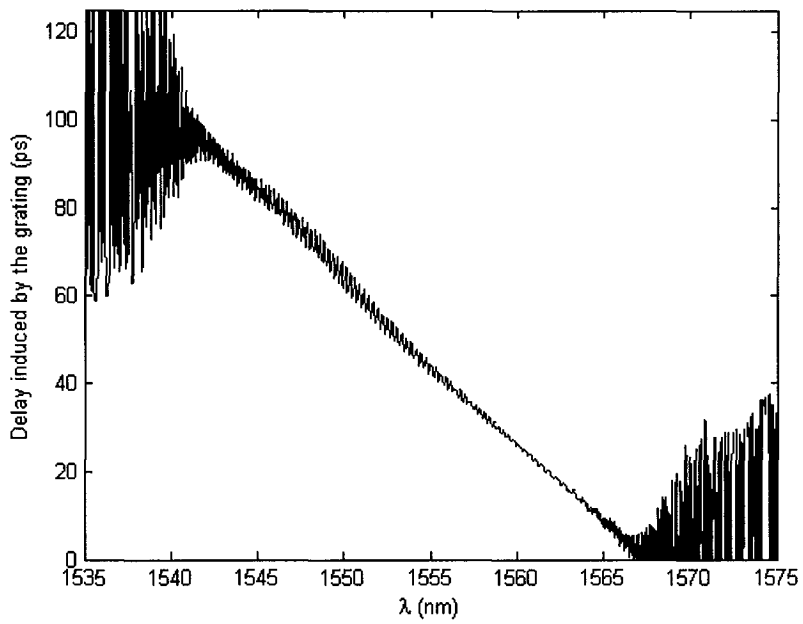

(b)

Fig. 2.19 Simulation results of the (a) reflection response and (b) delay induced by a 10-mm long Gaussian-apodized Bragg grating with total chirp of 9 nm.

2.2.2 Photosensitivity

Photosensitivity refers to a permanent change in the index of refraction of a photo-conductive and electro-optic material induced by exposure to light radiation [56]. Photosensitivity is commonly used to modulate the refractive index of materials spatially and fabricate devices such as Bragg gratings. The fabrication process of Bragg gratings will be described in Section 2.2.3.

Since the discovery of photosensitivity by Hill and al. [54] and the first demonstration of grating formation in Ge-doped fibers, there have been considerable efforts in modeling and increasing the photosensitivity in optical fibers. Many techniques and methods have been developed to achieve just this in both optical fibers and planar glass structures. Such methods include thermal-induced refractive index change, hydrogen loading, photosensitivity increase by strain, and co-doping [56] [74].

2.2.3 Fabrication of Bragg gratings

In 1989, an important breakthrough in the Bragg grating fabrication was made by Gerry Meltz and his coworkers [55]. The method they developed uses the superposition of ultraviolet beams in order to produce an interference pattern which creates the grating. Another technique for fabricating Bragg gratings consists of the two ultraviolet beams being generated by exposing a periodic phase mask with a single UV beam. This section will describe these two techniques for fabricating Bragg gratings in more details.

The holographic method of fabricating Bragg gratings uses a beam splitter to divide a single ultraviolet beam. The two beams resulting from this splitter are brought together by reflections from two mirrors. The fiber is then placed in the interference pattern created at the intersection of the two UV beams. Fig. 2.20 shows the holographic method to write Bragg gratings.

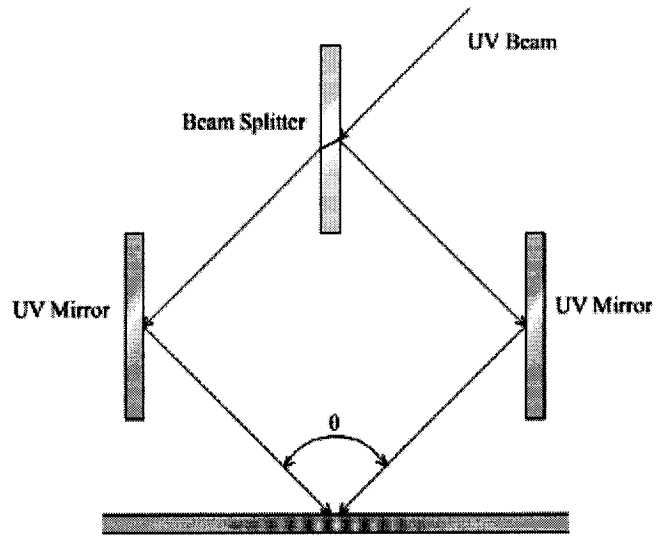

Fig. 2.20 Holographic method to write Bragg gratings.

With this method, the Bragg wavelength is given by

$$\lambda_B = \frac{n_{eff}\,\lambda_{UV}}{n_{UV}\sin\left(\frac{\theta}{2}\right)} \tag{29}$$

where λ_{UV} is the wavelength of the UV beam, n_{UV} is the refractive index of silica in the UV region and θ is the mutual angle of the UV beams.

From this equation, it can be seen that the Bragg wavelength of a grating can be chosen independently of the UV wavelength by controlling the mutual angle of the UV beams. This method is better suited for short exposure times as mechanical vibrations and long path lengths in the air affect the quality of the grating written if longer exposure time would be used.

The second method to write Bragg gratings uses a phase mask as a component of the interferometer. A phase mask is a relief grating which is often fabricated by holographic exposure, but can also be fabricated by e-beam lithography in a fused silica plate. For grating writing, the phase mask used is also called a zero-order-nulled phase mask as it is designed so that minimum radiation is transmitted in the zeroth order and maximum radiation is transmitted into the two first-order beams [75-76]. Figure 2.21 illustrates the concept of the zero-order-nulled phase mask.

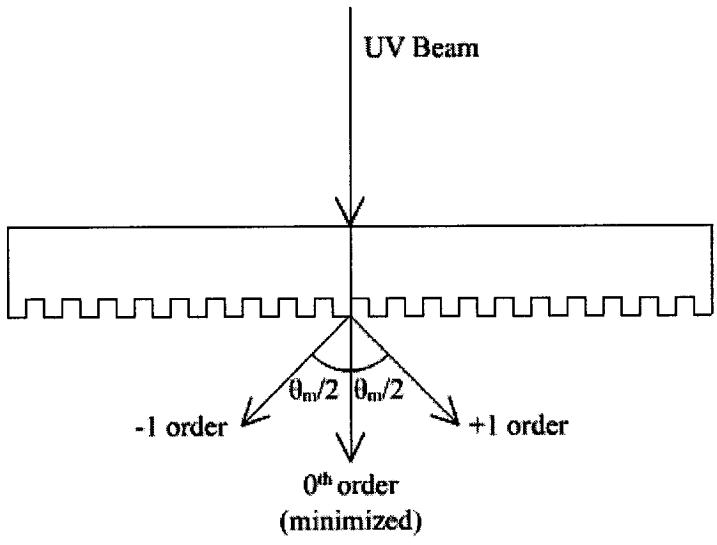

Fig. 2.21 Diffraction of a UV beam from a phase mask.

The period of the Bragg grating is related to the Bragg wavelength by the following relation

$$\lambda_B = n_{eff}\,\Lambda_{PM} \tag{30}$$

where Λ_{PM} is the period of the relief grating etched in the phase mask.

Photosensitivity, a property of a material indicating that it will react when exposed to light energy, allows the writing of Bragg gratings in optical fibers and waveguides. This material property is still being investigated as to which mechanisms are contributing to its effects. In order to increase the photosensitivity of an optical waveguide, germanium can be used as a defect former. UV radiation can cause large changes in the local refractive index of Ge-doped silica. The presence of hydrogen also greatly contributes to the photosensitivity of silica. Even if the understanding of photosensitivity is limited, its effects have been exploited in numerous applications as far as grating fabrication is concerned.

2.3 Summary

In this chapter, the concept of phased array antennas has been introduced. The difference between a phase shift beamforming module and a true time-delay beamformer were discussed and the clear advantages of the true time-delay approach at high microwave frequencies were explained. Bragg gratings, which will be used in the true time-delay beamformer developed in this research project, were introduced in this chapter. The transfer

matrix method was presented as a way to simulate the behavior of Bragg gratings with arbitrary coupling constant and chirp. Two methods for fabricating Bragg gratings were presented: the holographic method and the phase mask method.

Chapter 3

TRUE TIME DELAY BEAMFORMING MODULE DESIGN

The key components in a true time-delay beamforming network are the delay lines. These delay lines are required to produce accurate time delays and offer a large tunability. In this research project, the tunable time delays are achieved by using a waveguide Bragg prism [14] [18] [42] [45]. The results of the characterization of the Bragg prism are given in Chapter 4. In this chapter, we discuss the construction of the true time-delay beam forming network using the Bragg prism. The true time-delay beamforming network under consideration in this project is depicted in Fig. 3.1. Electrical components are presented in bold.

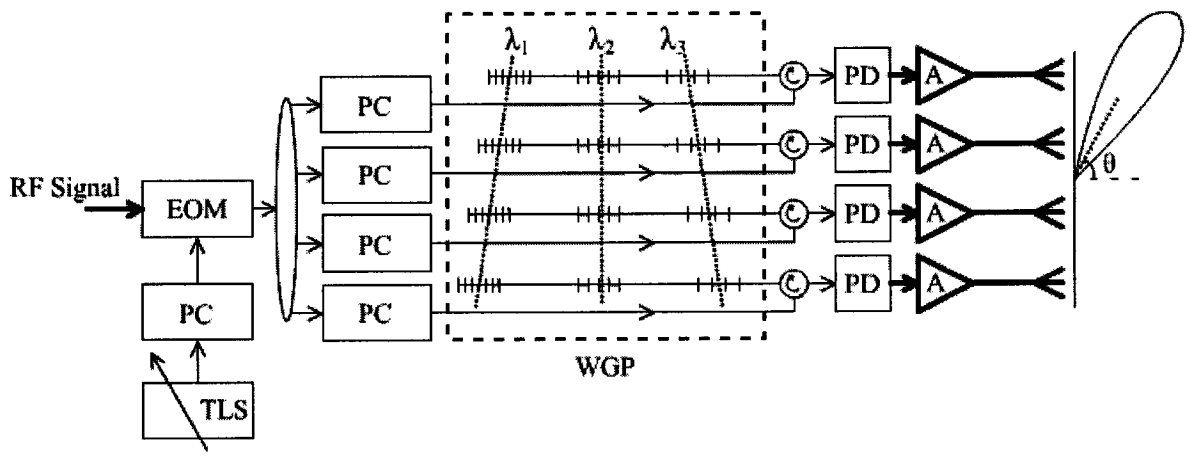

Fig. 3.1 True time-delay beamforming network using a waveguide Bragg grating prism.

The output of a tunable laser source (TLS) is sent to an external electro-optic modulator (EOM) through a polarization controller. At the EOM stage, the optical carrier is intensity modulated by the electrical signal. The modulated light signal is then divided equally into four branches by a 1:4 splitter. Each output branch is connected to a three-port optical circulator after going through a polarization controller (PC). At this stage, the polarization controller is required to control the polarization state of the light as the waveguides used are slightly birefringent and the standard SMF is used to interconnect the various optical components. The optical signals are then sent to the waveguide Bragg grating prism. Depending on the wavelength of the optical carrier, the Bragg grating prism will reflect the light at different spatial locations, where the corresponding gratings are located. This spatial location can be translated into a time delay progression of the modulated optical signal at the output of the waveguide Bragg grating prism. The reflected light goes through the circulator again and on to a photodetector. The time delays caused by the location of the gratings along the delay lines are then translated into different beamsteering angles.

3.1 Optical source

Many laser configurations have been developed in the past and many are currently being researched for different photonics applications. Such configurations include distributed-feedback (DFB) lasers, distributed Bragg reflector (DBR) lasers, including external cavity DBR lasers and external fiber-cavity DBR lasers, Vertical Cavity Surface Emitting Lasers (VCSELs), in-fiber lasers and fiber ring lasers. In this research project, a tunable laser source is required to generate an optical carrier signal at different wavelengths. As

previously stated, tuning the wavelength of the optical carrier will result in the tuning of the angle of the main beam in the radiation pattern of the phased array antenna.

Several types of wavelength-tunable lasers are currently available. The first two technologies are based on DFB and DBR structures and include a waveguide-type grating filter in the lasing cavity. The wavelength tuning is achieved either by varying the temperature of the cavity or by changing the injection current in the gain (active) section or the passive section of the laser [77-82]. Typically, DFB lasers tuned by varying the temperature of the laser and DBR lasers are tuned by varying the injection current to the grating. Temperature tuning can yield a limited wavelength tuning (typically 5 to 15 nm). Varying the injection current provides a maximum tuning range that depends on the output power. High output power levels results in a narrower wavelength tuning range. Fig. 3.2 illustrates a tunable 2-Section DBR laser.

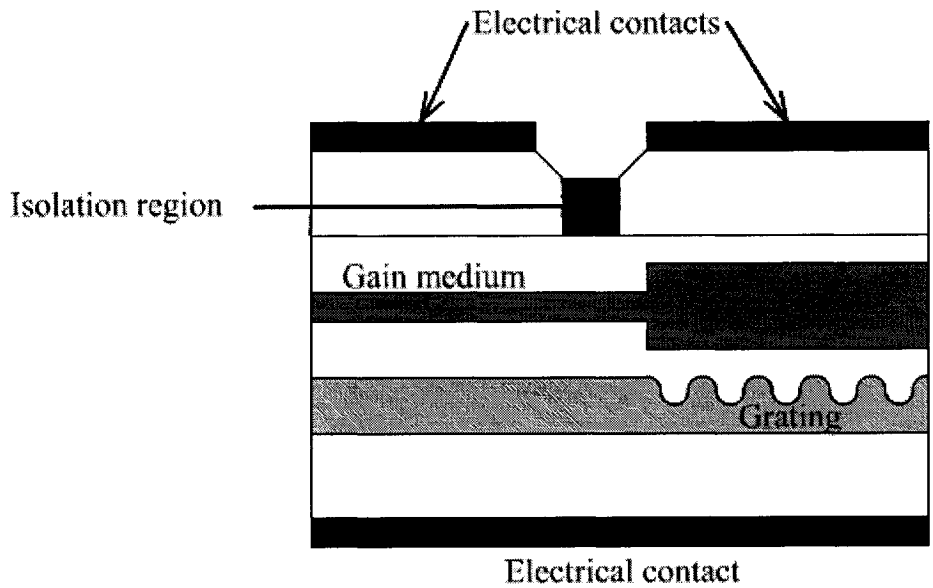

Fig. 3.2 Tunable 2-section DBR laser.

Another type of tunable lasers is the external-cavity diode lasers. Such lasers consist of a Fabry-Perot laser diode and an external diffraction grating which exhibits high reflectivity. External-cavity lasers are tuned by mechanically tilting the diffraction grating [83-84]. Fig. 3.3 shows an external cavity laser.

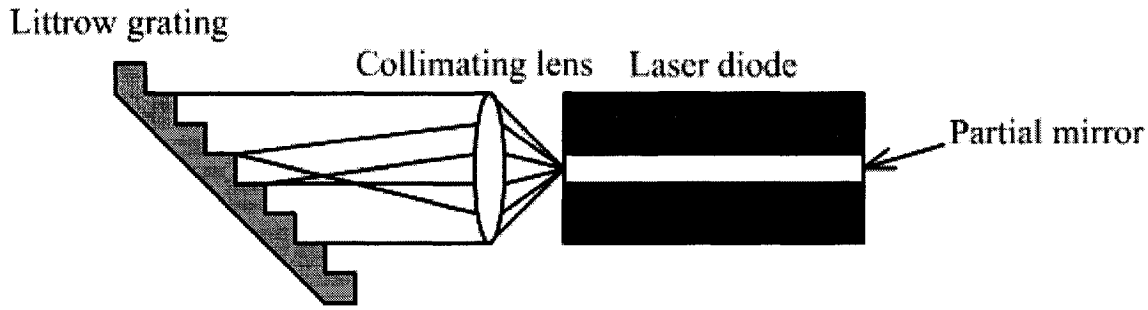

Fig. 3.3 External-cavity diode laser.

Vertical-cavity surface-emitting lasers are semiconductor microlaser diodes. VCSELs emit light perpendicular to the surface of the wafer on which they are fabricated. In this configuration, tuning is achieved by moving the top reflection mirror of the lasing cavity. This can be done by using micro-electro-mechanical systems (MEMS) [85-87]. Fig. 3.4 illustrates a possible configuration of a VCSEL.

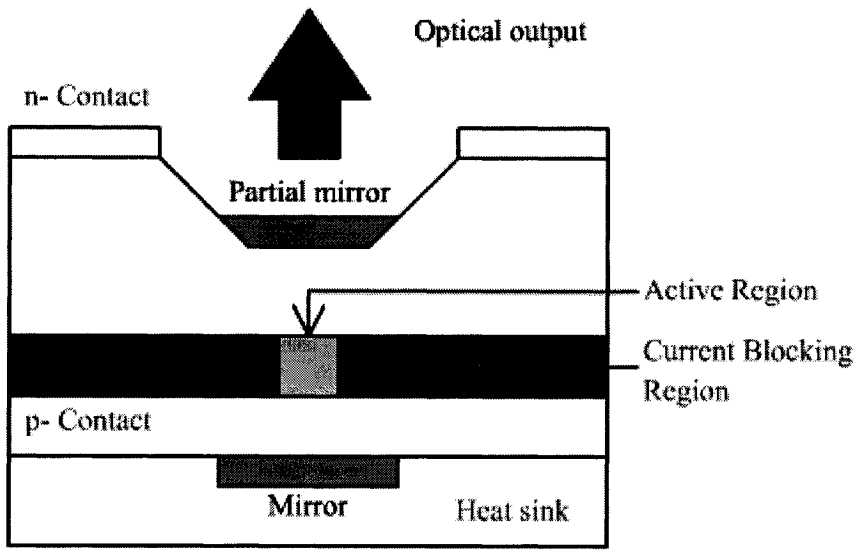

Fig. 3.4 Vertical-cavity surface-emitting laser.

In-fiber lasers use a length of Erbium-doped fiber as the gain medium. Various configurations of mirrors can be used and FBGs are well-suited for this application due to their wavelength-selective properties. The laser is pumped with an optical signal at a wavelength appropriate to the gain medium (e.g. 980 nm or 1480 nm for Erbium-doped fiber). Such lasers are able to output high power signals (up to 4 W in continuous operation). In the case where Bragg gratings are used as the mirrors, the tuning of such lasers can be done by stretching or compressing the gratings. This can yield a tuning range up to 40 nm. Fig. 3.5 illustrates an example of an in-fiber laser.

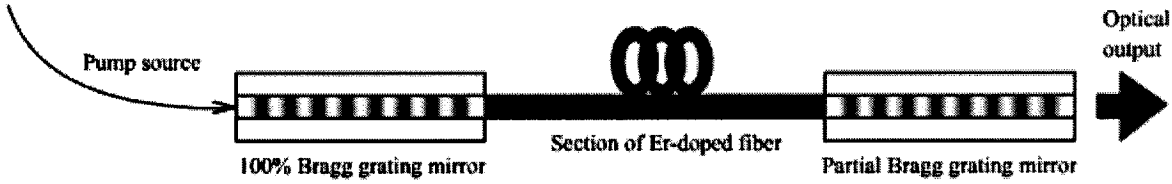

Fig. 3.5 In-fiber laser.

Instead of using mirrors at both ends of an in-fiber laser, a fiber ring configuration can be used [88-90]. The resulting laser gives a very narrow linewidth laser. A filter present in the ring allows the selection of the lasing wavelength and not the length of the ring. A Bragg grating can be used as the filter and tuning can be done by stretching or compressing the grating. Fig. 3.6 illustrates the concept of a fiber ring laser.

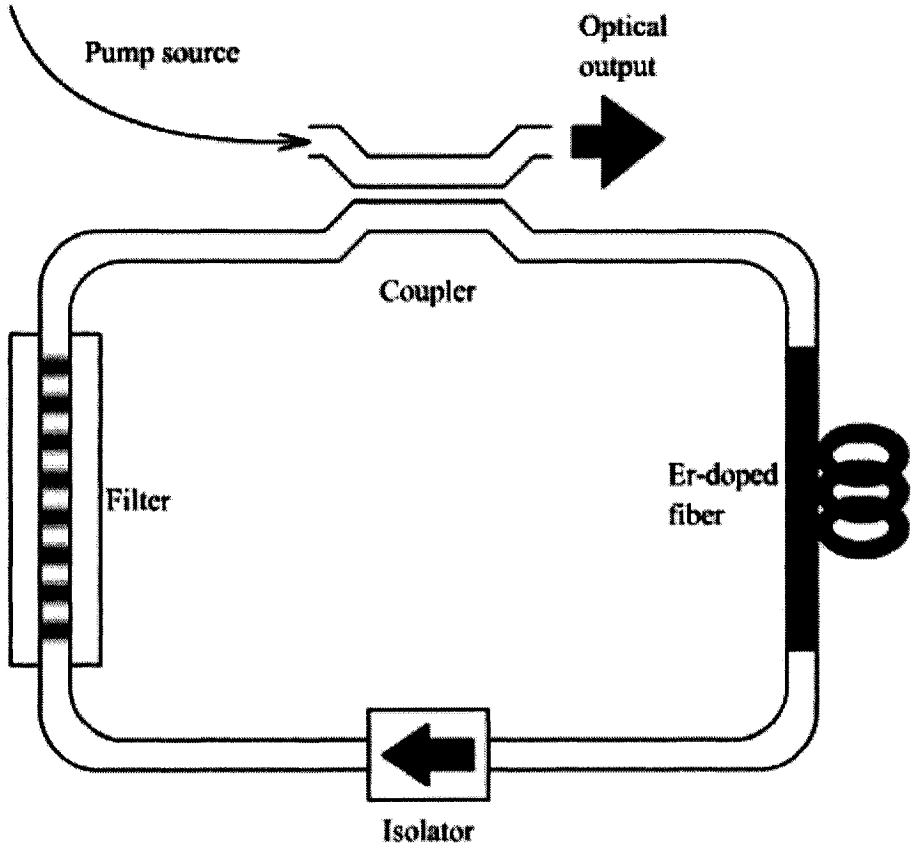

Fig. 3.6 Fiber ring laser.

3.2 Electro-optic modulator

Electro-optic modulators, as their name states, are based on the electro-optic effect, i.e., the modification of the refractive index of a nonlinear crystal by an electric field. The modification of the refractive index is proportional to the electric field strength [91-93]. Non-centrosymmetric crystal materials exhibit a linear relation between the electric field strength and the refractive index change. This electro-optic effect is also called Pockels effect. Other transparent media exhibit the Kerr electro-optic effect, where the refractive index change is proportional to the square of the electric field strength. This effect is

typically much weaker than the Pockels effect. Materials exhibiting the Pockels effect are called electro-optic materials.

The refractive index change of an electro-optic material is given by

$$\delta n(E) = \frac{-r n^3 E}{2} \tag{31}$$

where r is the electro-optic effect coefficient, n is the effective refractive index of the medium and E is the strength of the electrical field applied to the crystal.

By varying the strength of the electric field, the phase of the optical signal passing through the crystal will be changed. This phase variation will be directly proportional to the strength of the electric field and phase modulation of the optical carrier is obtained. The total phase change over an interaction length L is given by

$$\Delta\phi = \frac{2\pi\, \delta n\, L}{\lambda} \tag{32}$$

where λ is the free space wavelength of the optical signal.

In order to achieve an intensity modulation scheme, this phase modulator can be used in a Mach-Zehnder interferometer. Fig. 3.7 illustrates the configuration used.

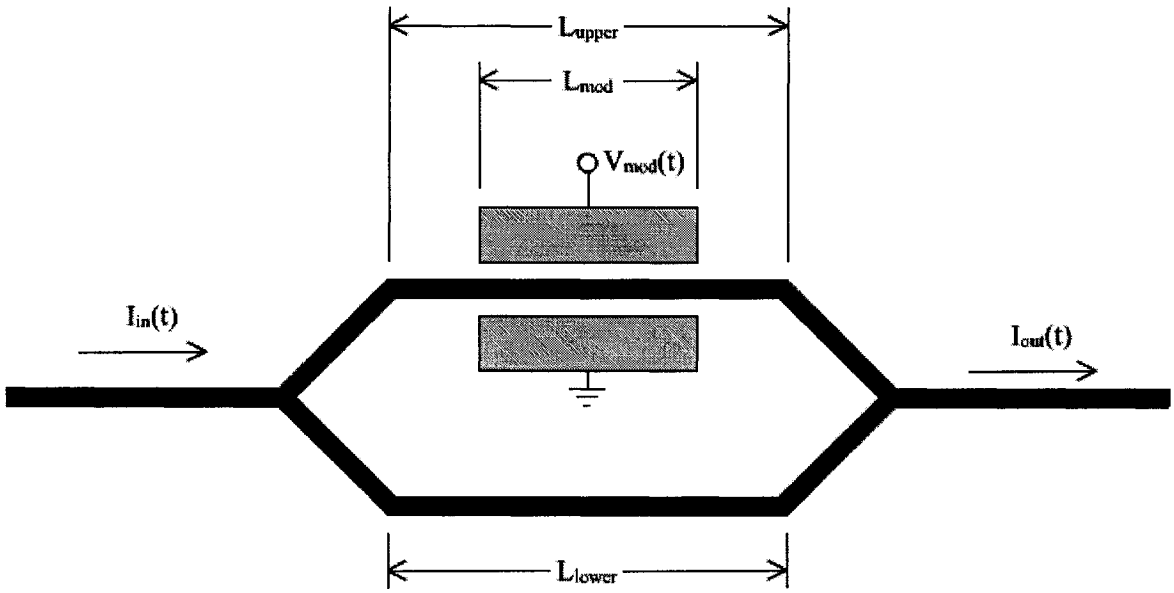

Fig. 3.7 Mach-Zehnder based electro-optic modulator.

By using Eq. 32, it is possible to find the phase shift in the upper branch as a function of the electric field strength

$$\phi_{upper}(E) = \frac{2\pi\, n L_{upper}}{\lambda} - \frac{2\pi\, \delta n(E) L_{\mathrm{mod}}}{\lambda} \tag{33}$$

where L_{upper} is the total length of the upper branch of the interferometer, L_{mod} is the length of the Pockel cell, $\delta n(E)$ is the refractive index change caused by the electric field as described in Eq. 31 and λ is the free space wavelength of the optical signal.

Similarly, the phase shift of the upper branch of the interferometer is given by

$$\phi_{lower} = \frac{2\pi n L_{lower}}{\lambda} \tag{34}$$

where L_{lower} is the length of the lower branch of the interferometer.

If the waveguide divides the input optical power equally, the output optical intensity is related to the input intensity by the well-known interferometer equation

$$I_{out}(t) = I_{in}(t)\cos^2\left(\frac{\Delta\phi}{2}\right) \tag{35}$$

where $\Delta\phi$ is the phase difference between the two branches of the interferometer defined as

$$\Delta\phi = \phi_{upper} - \phi_{lower} \tag{36}$$

When the phase difference is being controlled with a linear relation for a Pockel's effect, the transmittance of the electro-optic modulator becomes a function of the applied voltage as

$$T(V_{\text{mod}}) = \cos^2\left(\frac{\phi}{2} - \frac{\pi V_{\text{mod}}}{2V_{\pi}}\right) \tag{37}$$

where $\phi = \frac{2\pi n(L_{upper} - L_{lower})}{\lambda}$, V_{mod} is the applied voltage and V_{π} is the voltage to achieve a π phase shift between the beams of the two arms of the interferometer. In order to produce a

linear intensity modulator, the optical path difference has to be adjusted so that $\phi = \frac{\pi}{2}$. When this is the case, Eq. 35 can be approximated as

$$I_{out}(t) = \frac{I_{in}(t)}{2}[1 + m V_{\mathrm{mod}}(t)] \tag{38}$$

where $V_{mod}(t)$ is the electric signal applied to the Mach-Zehnder modulator.

3.3 Waveguide Bragg grating prism

In a true time-delay beamforming system, the delay lines play the key role in achieving squint-free and accurate radiation patterns. In the proposed system configuration, the tunable time delays are achieved by using a waveguide Bragg grating prism. Two different configurations are presented in this section, the first one being composed of discrete uniform Bragg gratings and the second, of chirped gratings.

A Bragg grating prism composed of discrete Bragg gratings does not require special phase masks as the prism is composed of discrete uniform gratings. General purpose uniform phase masks can be used to create such a prism. Fig. 3.8 illustrates an $N \times M$ Bragg grating prism composed of discrete gratings. N represents the number of delay lines and M represents the number of gratings per delay line which is equal to the number of possible angles of the main beam of the radiation pattern of the phased array antenna.

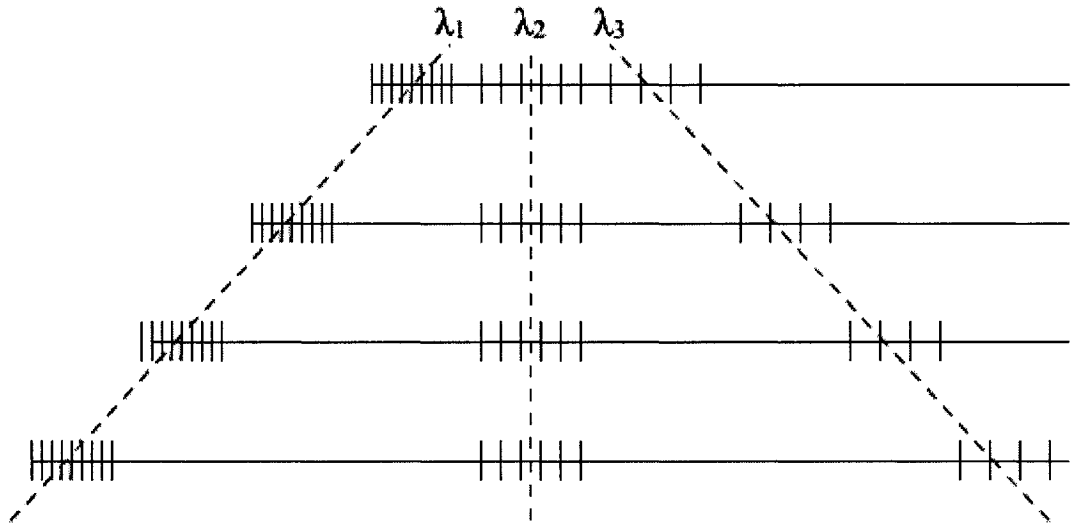

Fig. 3.8 4 × 3 Discrete Bragg grating prism.

The spacing between the gratings when using this configuration is critical as it is directly proportional to the time delays of the optical signals traveling through each line. The velocity of light in a waveguide is reduced by a factor equal to the refractive index of this waveguide. Thus, when an optical signal is reflected by a Bragg grating, the time delay incurred by the optical signal at the output of the Bragg grating prism is proportional to twice the distance between the grating and the input/output of the prism as

$$\Delta\tau = \frac{2\Delta d\, n_{eff}}{c} \tag{39}$$

where Δd is the distance between the grating and the input/output of the prism, n_{eff} is the effective refractive index of the optical waveguide and c is the velocity of light in vacuum.

When considering the radiation pattern of phased array antennas, the absolute time delays are not of interest but rather the relative time delay between each feed signal. Since the time delay of the recovered electrical signal is equal to that of the optical signal (if we assume that the response time of the photodetector is negligible), the time delay progression induced by the delay lines are in direct relation with the radiation pattern of the phased array antenna. Therefore, a constant spacing between two gratings in all delay lines will not affect the shape of the radiation pattern as it will induce an equal time delay for all optical signals but a linear spacing progression will affect the shape of the radiation pattern. Fig. 3.9 illustrates this spacing. In the figure, the constant spacing L_1 and L_2 are not affecting the shape radiation pattern while the spacing progressions of l_1 and l_2 are contributing to the beamforming.

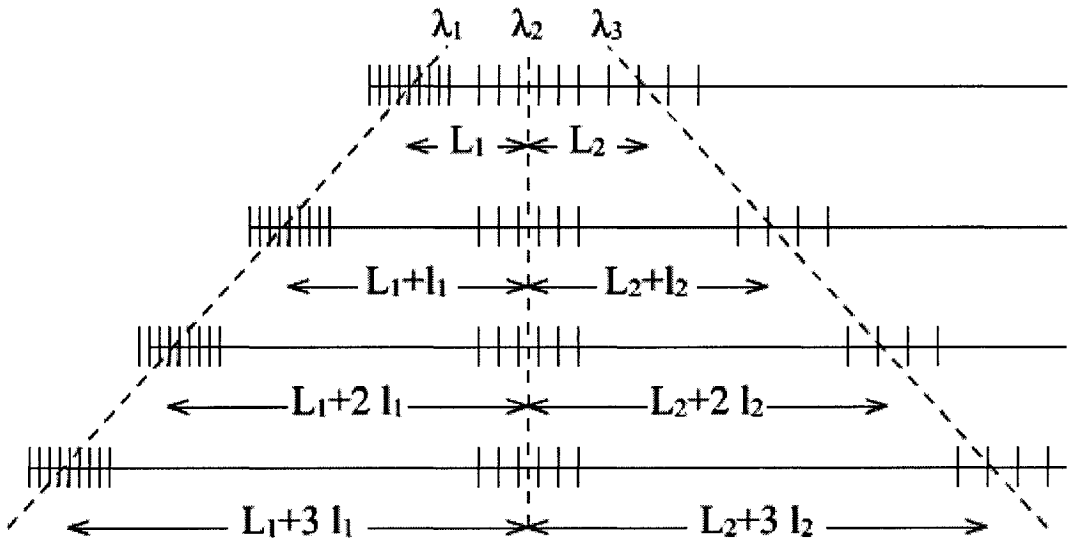

Fig. 3.9 Spacing of the Bragg gratings in a discrete Bragg prism.

A drawback of using discrete uniform gratings is that the orientation of the mainlobe of the phased array antenna is limited by the number of gratings. In order to overcome this

limitation, a chirped Bragg grating prism can be built. The fabrication of such a prism requires chirped phased masks of different lengths and different chirp rates. Fig. 3.10 illustrates a chirped Bragg grating prism.

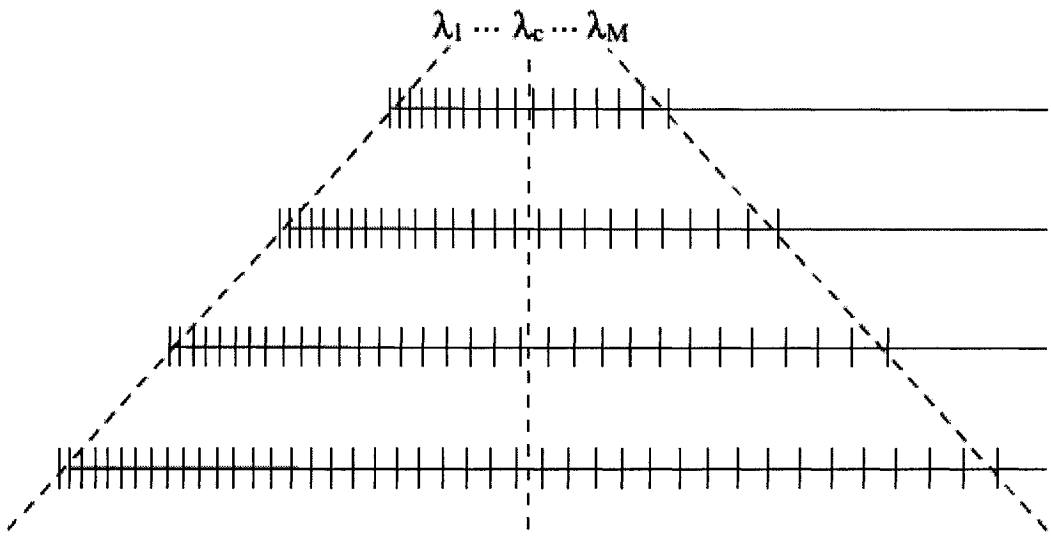

Fig. 3.10 Chirped Bragg grating prism.

In a chirped Bragg grating prism, the total chirp of the Bragg gratings should be equal, but the lengths of the gratings vary with a linear increment. Optical signals reflected by each delay line will be delayed by a linear time delay progression which comes from the group delay response of the gratings. The center wavelength λ_c corresponds to the point where the optical signals are reflected at the same distance from the input of the prism. The time delay progression at this point is null.

In this research project, a discrete uniform Bragg grating prism is constructed. In the future, a chirped Bragg grating prism can be constructed to exploit the advantages of such a configuration.

3.4 Photodetector

There exist many types of optical receivers. The most widely used ones are semiconductor photodetectors, which include the PIN photodetector and the Avalanche photodetector (APD). PIN photodetectors consists of a positively doped (*p*-doped) layer and a negatively doped (*n*-doped) layer and these two layers are separated by an intrinsic semiconductor layer, hence its name *p-i-n* photodetector [91] [93-94]. APD is a photodiode with an internal current gain which differentiates it from the PIN photodetector [91] [93-94]. Both types of photodetectors are reverse biased. This increases the size of the depletion region which results in a large internal electric field. In the case of the APD, a large reverse bias is responsible for the internal current gain.

The process of light detection in a PIN photodetector starts with incident light on the photodetector. When the photon energy is greater than the band gap of the semiconductor material, an electron-hole pair is generated by absorption of the photon. Because of the reverse bias, the electron and the hole are separated by the high electric field present in the depletion layer. This movement of electrons and holes creates a current in the outer circuitry. Fig. 3.11 shows the basic structure of a PIN photodetector.

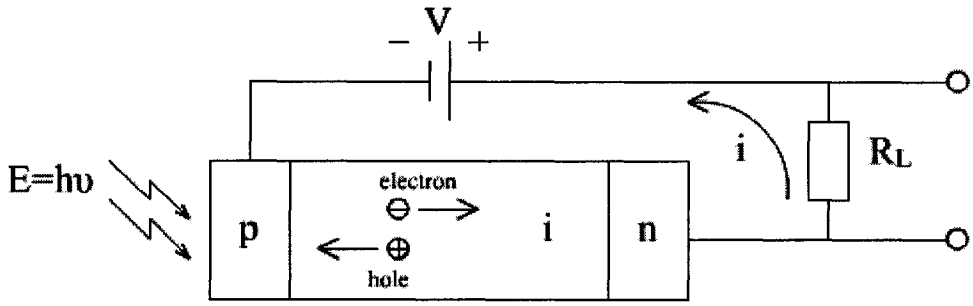

Fig. 3.11 Structure of a PIN photodetector.

In an APD, the absorption of a photon creates an electron-hole pair like the PIN photodetector. Since a large electric field in present in the depletion region, the free charges accelerate rapidly. Charges propagating at high velocities can give a part of their energy to other electrons and create other electron-hole pairs. This process leads to an avalanche (hence the name of the photodetector) multiplication of the charges. Fig. 3.12 illustrates the structure of an APD.

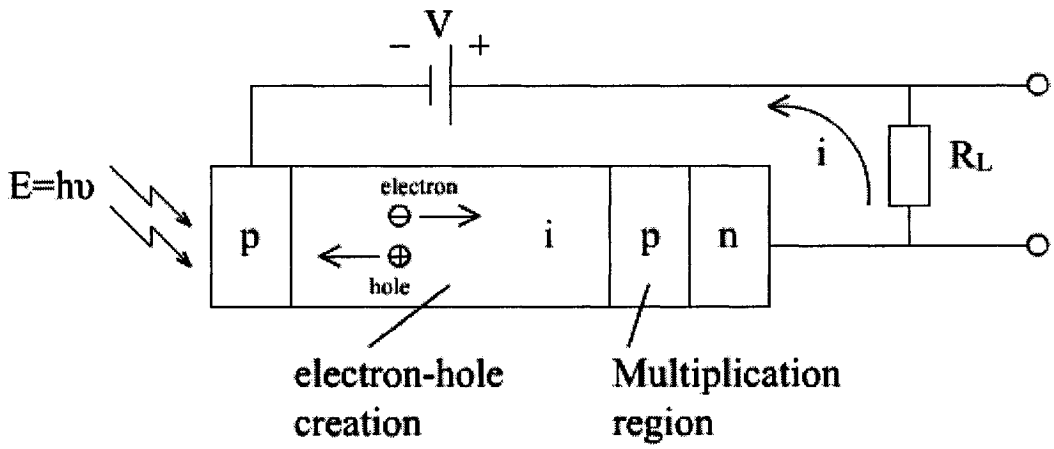

Fig. 3.12 Structure of an avalanche photodetector.

The relation between the incident optical power P_o and the photocurrent I_p for both PIN photodetectors and APDs is given by

$$I_p = \frac{M \eta q}{h\nu} P_o \tag{40}$$

where M is the Multiplication of the APD and is equal to 1 for a PIN photodiode, η is the quantum efficiency, q is the electron charge and $h\,v$ is the photon energy.

Important parameters of photodetectors include the quantum efficiency which can be calculated as

$$\eta = \frac{h\nu}{q} \frac{I_p}{P_o} \tag{41}$$

Another important parameter is the responsitivity of the photodetector given by

$$\Re = \frac{I_p}{P_o} = \frac{\eta q}{h\nu} \tag{42}$$

This last parameter is quite useful in practice as it gives the photocurrent generated per unit optical power.

When an optical signal *E(t)* is incident on the photodetector, the modulated electrical signal can be recovered exactly if shot noise and thermal noise are neglected. Propagation through an optical fiber will lead to signal degradation which are presented as amplitude and phase distortion. This degradation is mainly caused by chromatic dispersion and chirp effects. The impact of chromatic dispersion on a remote true time-delay beamforming system will be discussed in Chapter 5.

3.5 Summary

The configuration of the true time-delay beamforming module has been introduced in this chapter. The basic functions of each component are first described. Each component was then presented in more details. Firstly, different tunable optical source configurations were introduced. The description of the Mach-Zehnder interferometer based electro-optic modulator and the waveguide Bragg grating prism used to delay the modulated optical signals were presented. Finally, photodetectors were introduced with more emphasis on the PIN photodetector. These components will be used to measure the parameters of the waveguide Bragg grating prism constructed in this research project.

Chapter 4

WAVEGUIDE BRAGG PRISM IMPLEMENTATION

This chapter will present the experimental results of a waveguide Bragg grating prism fabricated on planar integrated optical waveguides. The waveguide Bragg grating prism implemented contains four delay lines with three Bragg gratings in each line. The physical distance separating the three gratings follows a linear progression which is required to achieve beamsteering capability for the phased array antenna. The Bragg gratings were fabricated using UV photo-imprinting technique with a phase mask. This method of fabricating Bragg gratings has been described in Section 2.2.2. The optical performance of the waveguide Bragg grating prism developed is evaluated and compared with simulation results. A true time-delay beamformer using the waveguide Bragg grating prism is constructed and its performance is characterized and analyzed.

4.1 Waveguide design and fabrication

The waveguides used to implement the waveguide Bragg prism were developed at the Communications Research Center. The waveguide Bragg prism is fabricated on germanium-doped silica-on-silicon planar optical waveguides. The waveguides were fabricated using plasma-enhanced chemical vapor deposition and reactive ion etching.

To create Ge-doped silica-on-silicon waveguides, plasma enhanced chemical vapor deposition allows the deposition of thin films of silica on silicon wafers. The silicon wafers are placed in a mixture of gases which chemically react at the surface of the wafers. The main advantage plasma enhanced chemical vapor deposition over traditional chemical vapor deposition techniques is that it avoids the need for a high temperature by exciting the reactant gases into a plasma.

Reactive ion etching uses highly energetic chemically reactive ions to bombard the material to be etched with. The goal of RIE is to dislodge atoms from the material, therefore removing material by bombardment.

The theoretical design of the parameters of the optical waveguides was done using the finite difference beam propagation method (BPM) simulations. Finite difference BPM is one of the most powerful techniques to study lightwave propagation in waveguides. Finite difference BPM solves Maxwell's equations by using finite differences in place of partial derivatives. The derivation of the differential equations has been detailed in several research papers [95-99].

The theoretical design takes into consideration that the input field into the optical waveguide will be one exiting a standard SMF. The parameters of the optical fiber for simulation purposes are the following:

- Core index : 1.45204
- Cladding index : 1.44681
- Diameter : 8.14 μm

The parameters of the SMF are typical values for a Corning SMF-28 and are used by Optiwave Corporation in many of their example simulations.

The following figures show the refractive index profile and the mode field of this step-index SMF which has been simulated using the software package OptiBPM from Optiwave Corporation.

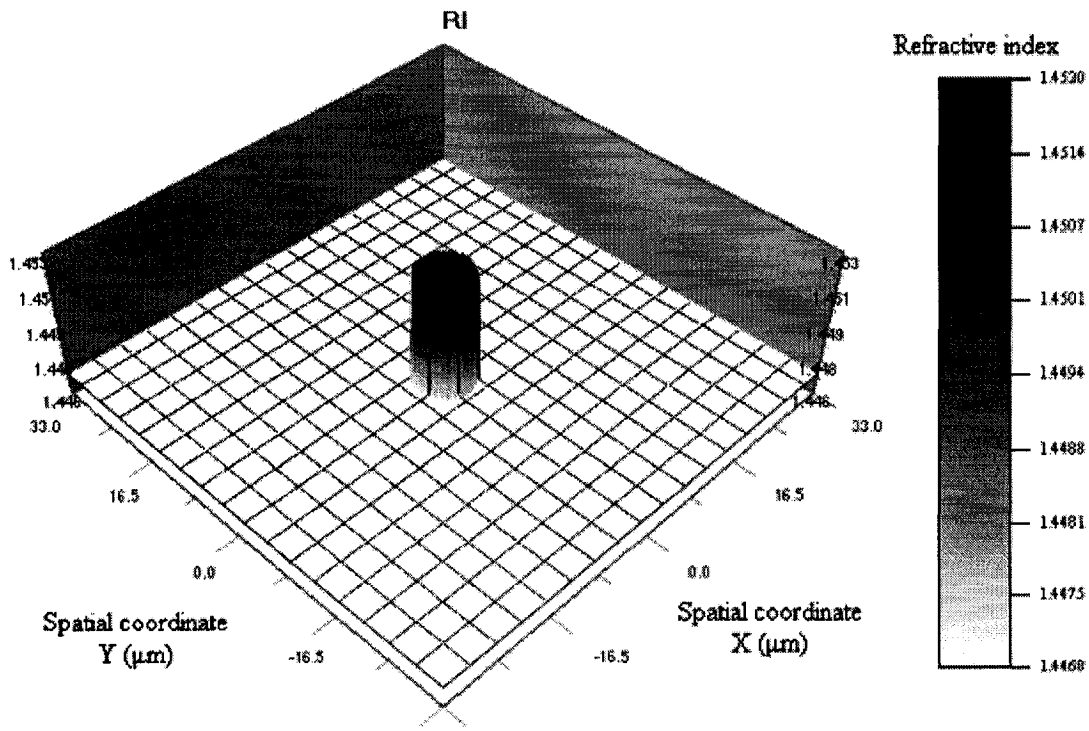

Fig. 4.1 Refractive index profile of a step-index single mode optical fiber.

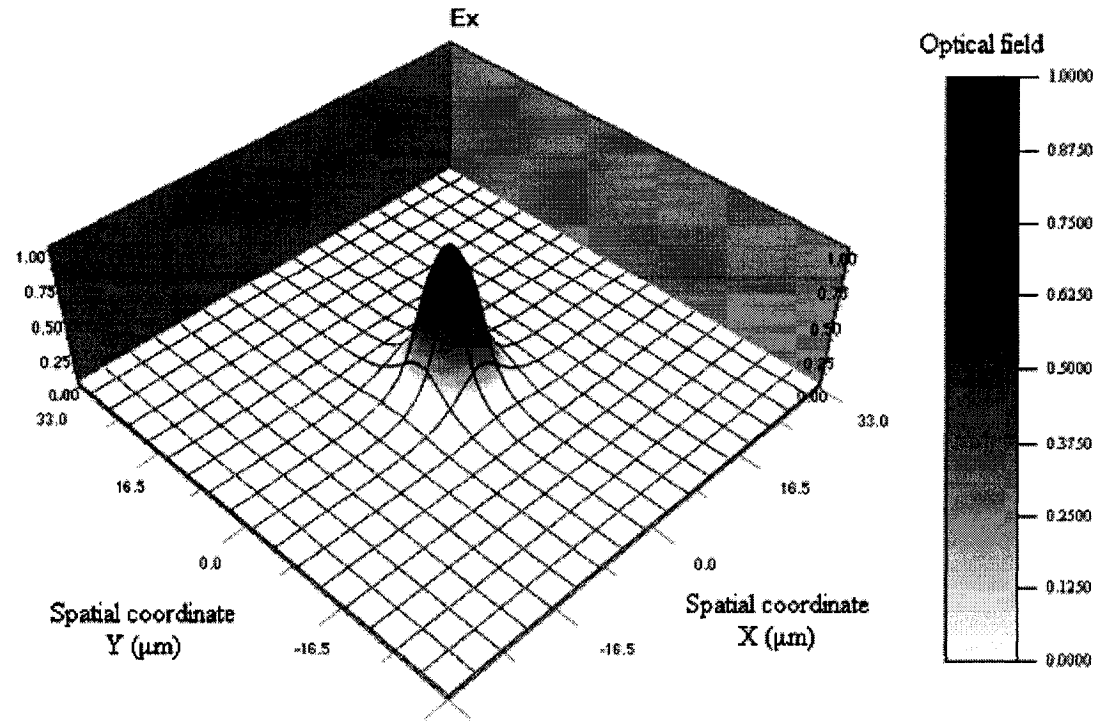

Fig. 4.2 Mode field of a step-index single mode optical fiber.

The following figure shows the simulation setup for the design of the planar optical waveguide used in this research project.

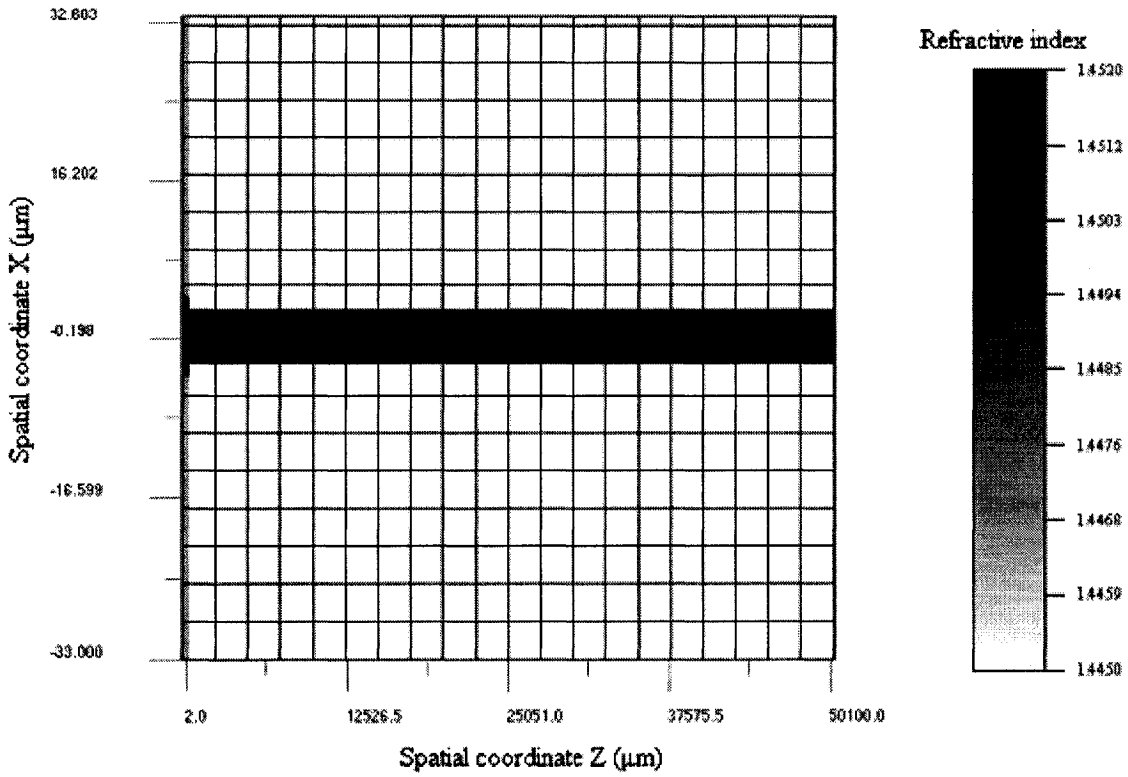

Fig. 4.3 Simulation layout for light coupling between SMF and planar optical waveguide.

Several simulation parameters were tested before achieving an optimal solution given the fabrication constraints. Fig. 4.4 illustrates the BMP simulation result of the planar optical waveguide designed.

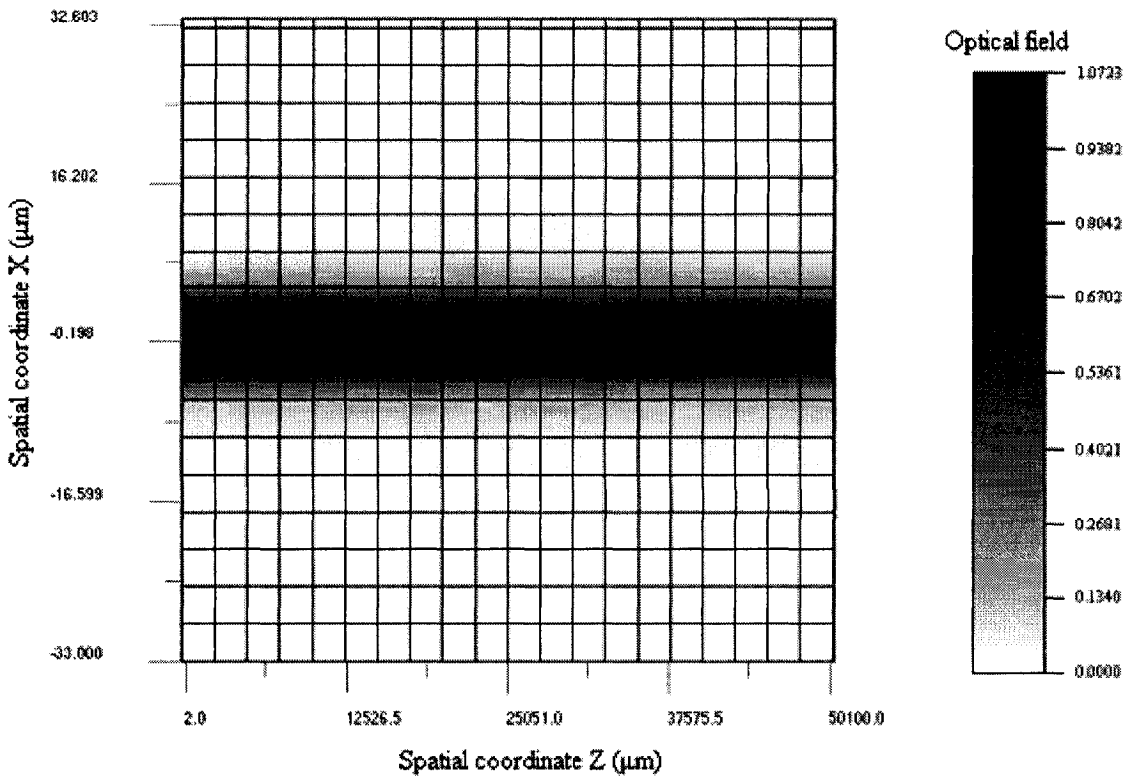

Fig. 4.4 BPM simulation of light coupling between a SMF and the designed planar optical waveguide.

The optical waveguides fabricated have the following parameters:

- Core index : 1.455
- Cladding index (top and bottom) : 1.445
- Width : 6 µm
- Height : 6 µm
- Length : approx. 50 mm

Fig. 4.5 shows a picture taken at the Communication Research Center of the cross-sections of the fabricated waveguides. The picture clearly shows the square core and the reflowed borophosphosilicate glass top cladding layer.

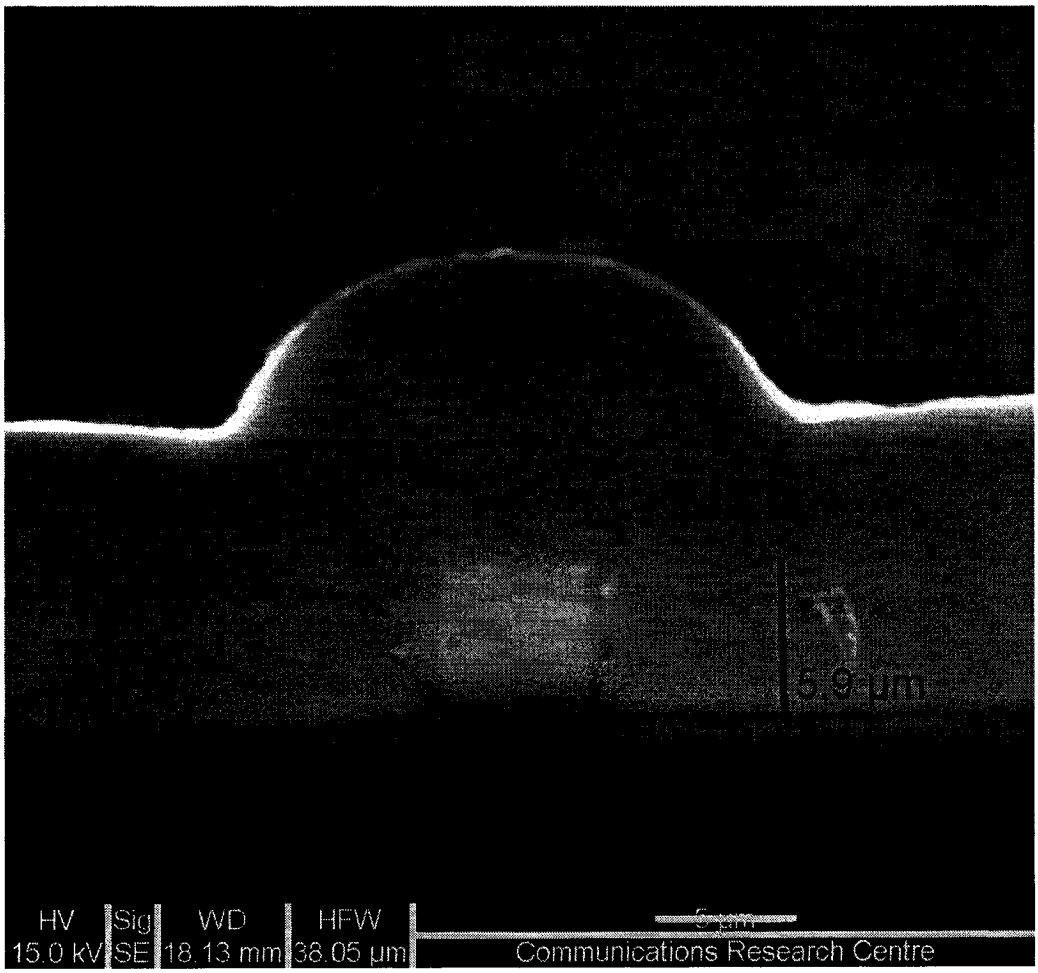

Fig. 4.5 Cross-section of the Ge-doped Si/SiO_2 waveguides.

The next figure shows a top view of the wafer. The reflowed borophosphosilicate glass top cladding layer is quite apparent.

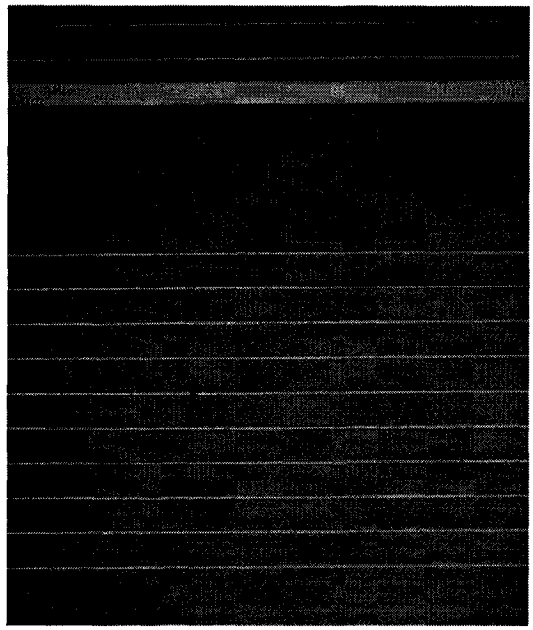

Fig. 4.6 Top view of the planar integrated optical waveguides.

The fabricated waveguides are slightly birefringent. This birefringence has been estimated to be approximately equal to 6×10^{-4}. This birefringence is estimated by characterizing polarization sensitive devices fabricated in the waveguides such as Bragg gratings. The cause of this polarization is mainly due to a stress field in the top cladding layer. The losses of the waveguides at a wavelength of 1550 nm have been measured to be less than 0.5 dB/cm.

4.2 Design parameters of the waveguide Bragg prism

As previously mentioned, the waveguide Bragg prism realized in this project is composed of four delay lines with three Bragg gratings in each line. The gratings are strategically

positioned in order to achieve a beamsteering capability. Fig. 4.7 illustrated the Bragg grating prism realized.

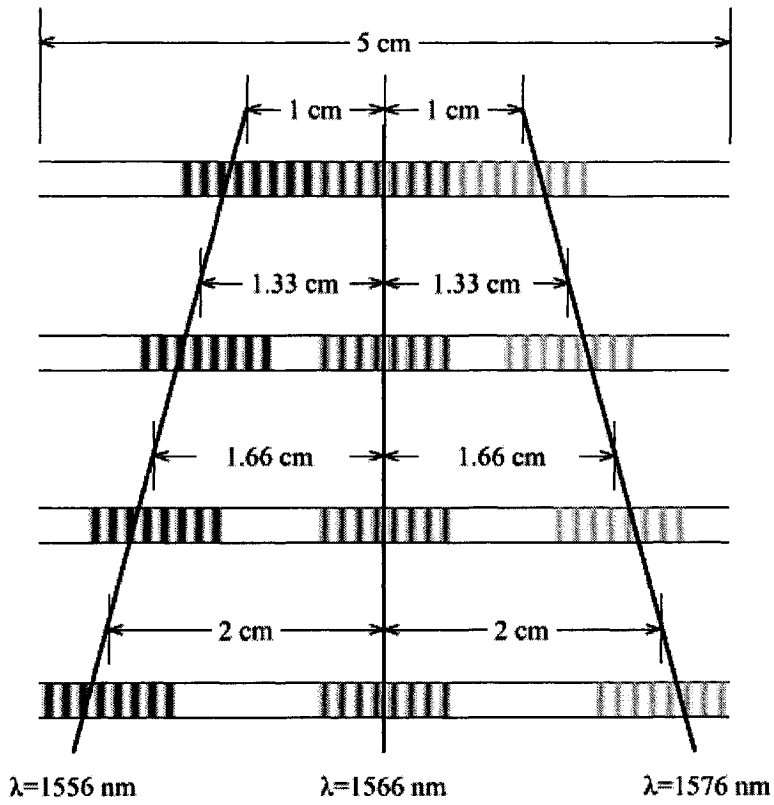

Fig. 4.7 Bragg grating prism realized in this research project.

The Bragg wavelengths of the gratings were chosen based on available phase masks and the range of the tunable laser source. The physical layout was chosen in order to maximize the scan area of the PAA. In typical applications, a scan area of ±60° would be required. It was not possible to realize such a large scan area in this research project mainly because of the length the Bragg gratings that was required to achieve good reflection gratings (which was experimentally determined to be around 10 mm) and the total length of the waveguides available, which is approximately 50 mm. Using these two values, a maximum physical

progression of 3.3 mm was possible on each side of the center Bragg grating, as shown in Fig. 4.7. Using this physical layout, it is possible to calculate the theoretical time delay induced by each grating by using Eq. 39, by indicating that the center grating is located in the middle of the 5-cm long waveguide and by using the effective refractive index of the waveguides, n_{eff} = 1.45. The optical signal is considered to be entering and exiting the waveguides from the right and the time delays are calculated from the time the optical enters the waveguide to the time where it exits the waveguide. Table 4.1 resumes these values. For the purpose of clarity, the gratings are identified by the number 1 to 12, assigned from left to right, top to bottom.

Grating number	Position relative to center grating (mm)	Time delay (ps)	Relative time delay with respect to center grating (ps)
1	-10.00	338.33	96.67
2	0.00	241.67	0.00
3	10.00	145.00	-96.67
4	-13.33	370.56	128.89
5	0.00	241.67	0.00
6	13.33	112.78	-128.89
7	-16.67	402.78	161.11
8	0.00	241.67	0.00
9	16.67	80.56	-161.11
10	-20.00	435.00	193.33
11	0.00	241.67	0.00
12	20.00	48.33	-193.33

Table 4.1 Theoretical time delays of the waveguide Bragg grating.

From Table 4.1, it is possible to notice the time delay progression for each wavelength. The time delay progression for a given wavelength can be calculated as the difference of the relative time delays with respect to center grating from two adjacent branches. This is equal to -32.22 ps for the gratings to the left, 0 ps for the center grating and 32.22 ps for the right gratings.

4.3 Bragg gratings characterization

When writing Bragg gratings in the optical waveguides using the UV photoimprinting system with phase masks, the photosensitivity of the waveguides caused by Ge-doping was found to be too weak. Thus, hydrogen loading was suggested to increase the photosensitivity of the waveguides. This was found to give acceptable gratings with a notch in the transmission spectrum of around -10 dB (10% transmission).

The following figures show the transmission and the reflection spectrum for all four delay lines of the waveguide Bragg grating prism.

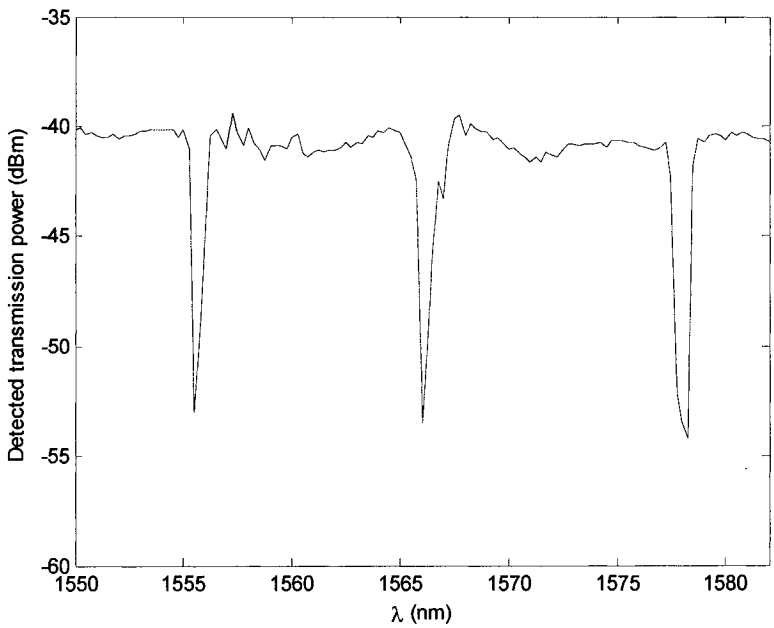

(a)

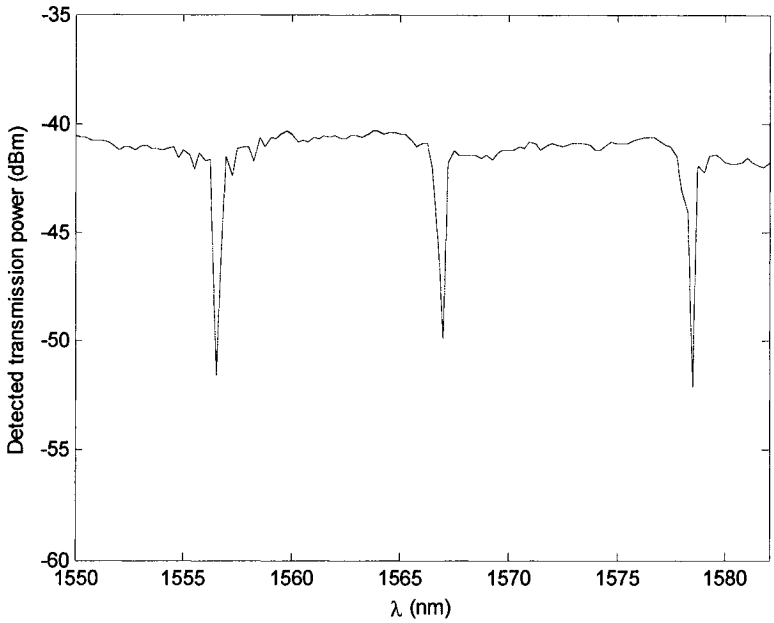
-35
-40
-45
-50
-55
-60
Detected transmission power (dBm)
1550
1555
1560
1565
1570
1575
1580
λ (nm)

(b)

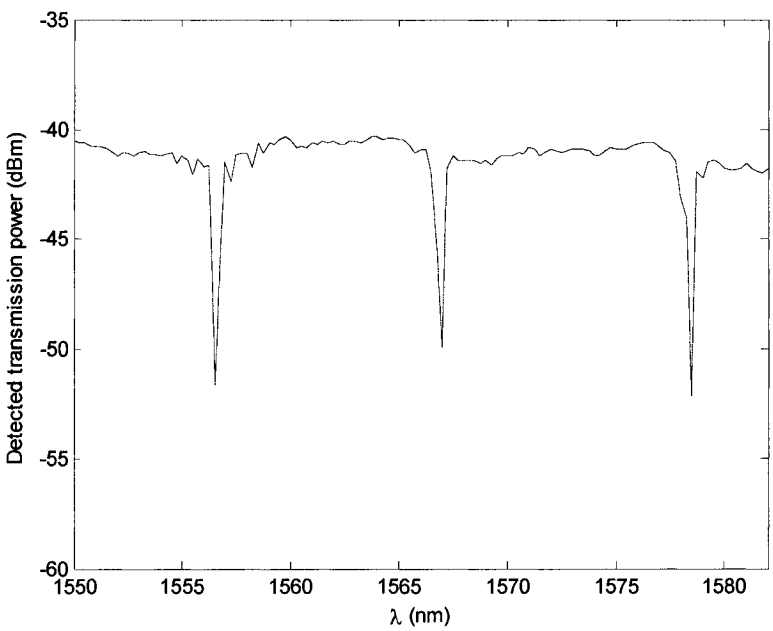
-35
-40
-45
-50
-55
-60
Detected transmission power (dBm)
1550
1555
1560
1565
1570
1575
1580
λ (nm)

(c)

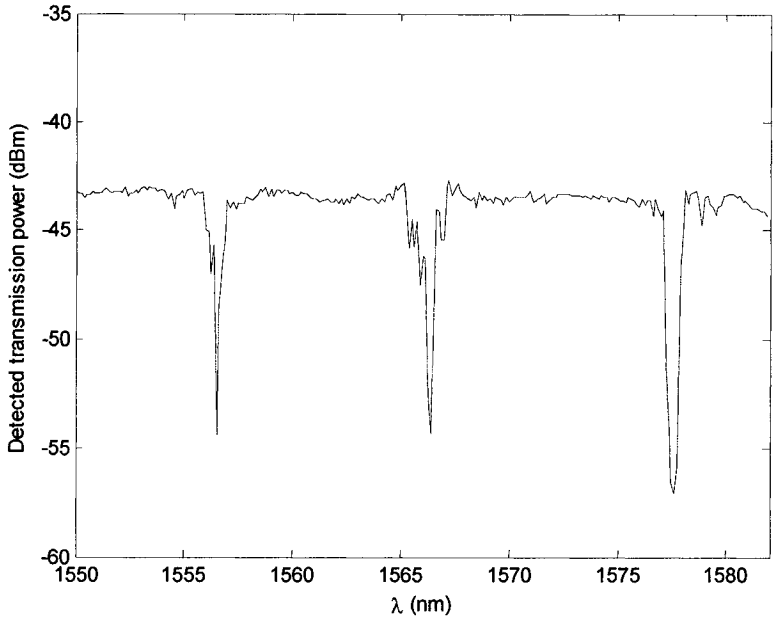

(d)

Fig. 4.8 (a)-(d) Transmission spectrum of the four waveguide delay lines.

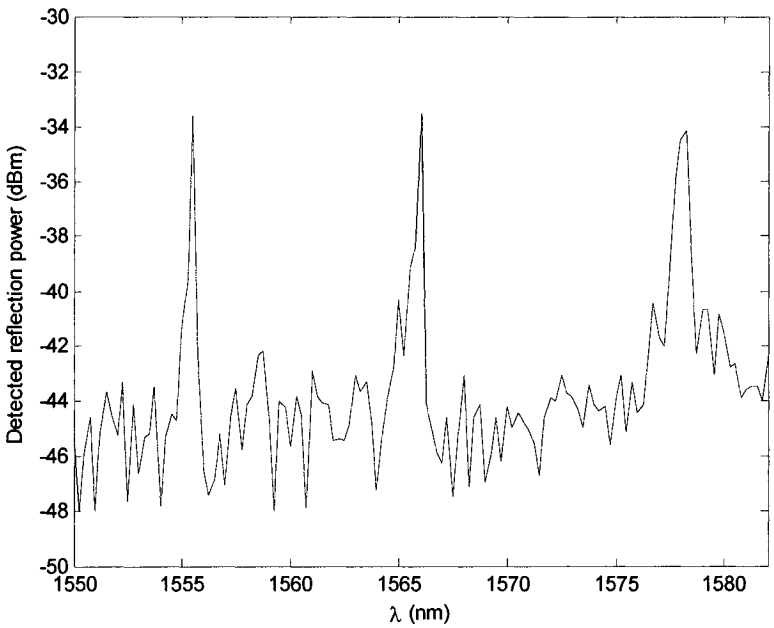

(a)

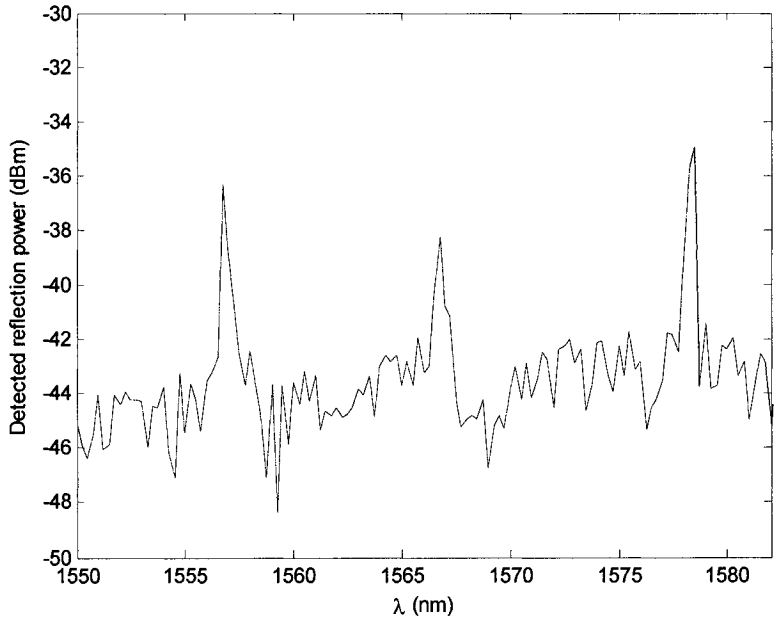
-30
-32
-34
-36
-38
-40
-42
-44
-46
-48
-50
Detected reflection power (dBm)
1550
1555
1560
1565
1570
1575
1580
λ (nm)

(b)

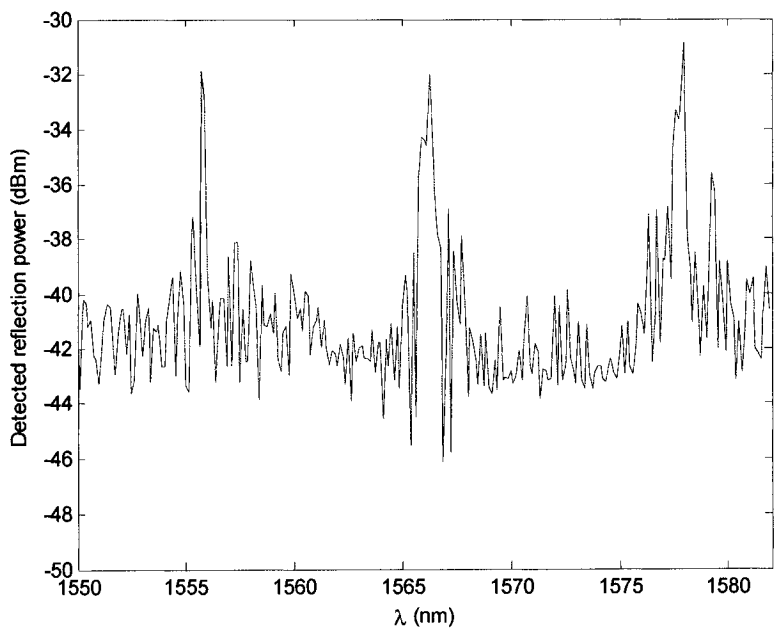
-30
-32
-34
-36
-38
-40
-42
-44
-46
-48
-50
Detected reflection power (dBm)
1550
1555
1560
1565
1570
1575
1580
λ (nm)

(c)

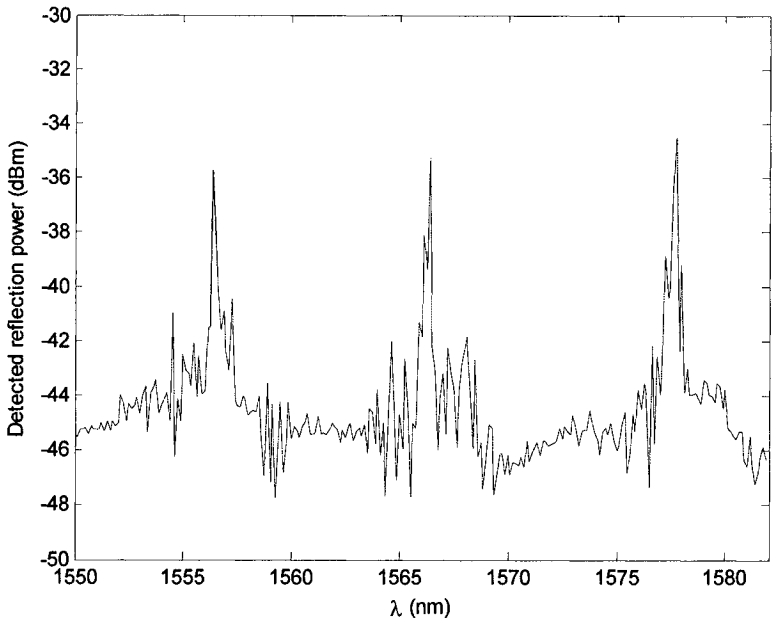

(d)

Fig. 4.9 (a)-(d) Reflection spectrum of the four waveguide delay lines.

Fig. 4.8 and 4.9 present different spectral responses for the Bragg grating delay lines. Ideally, the spectral response of all waveguide delay lines would be identical in both transmission and reflection. In practice, as the Bragg gratings are fabricated individually, alignment error during the fabrication process of the Bragg gratings can result in different transmission and reflection spectra from one delay line to another. A second factor contributing to differences in the transmission and reflection spectra comes from the fact that the waveguides fabricated at CRC can present slightly different optical properties. Hydrogen loading is another source of error as different concentration of hydrogen in the waveguides will affect significantly the photosensitivity of the waveguides to the UV light used in the fabrication of the Bragg gratings. Finally, optical characterization can also play a role in this subject as high insertion losses were found experimentally while these losses were minimal

in theory. A bad coupling between a SMF and the waveguides would be the most probable source of error.

It is important to mention that the fabricated device is not a waveguide grating prism but rather a set of waveguide Bragg gratings. This is true as the peak reflectivities of the gratings do not align exactly when comparing different delay lines. The exercise of simulating the beamformer obtained with this particular device assumes that another device can be made with adjusted the grating center wavelengths.

The following table summaries the main characteristics of the realized Bragg gratings.

Grating number	Center wavelength (nm)	3 dB bandwidth (nm)	Peak reflectivity (dB)	Grating length (mm)
1	1555.50	0.308	13.64	10
2	1566.00	0.287	14.02	10
3	1578.25	0.582	14.78	10
4	1556.50	0.210	11.33	10
5	1567.00	0.259	9.70	10
6	1578.50	0.284	11.89	10
7	1556.37	0.188	12.50	10
8	1566.25	0.118	14.26	10
9	1577.75	0.257	14.56	10
10	1556.50	0.159	11.80	10
11	1566.38	0.258	11.73	10
12	1577.63	0.401	14.46	10

Table 4.2 Characteristics of waveguide Bragg gratings.

Since hydrogen loading was used to increase the photosensitivity of the waveguides, thermal decay would occur over time at room temperature [100]. For commercial application, it would be better to increase the fluence of the Bragg writing system in order to achieve results without hydrogen loading to eliminate the thermal decay effects.

4.4 True time delay measurements

In order to measure the time delays caused by the gratings, the setup depicted in Fig. 4.10 was realized. A tunable laser source is used to select the wavelength of the optical carrier. The optical signal is fed to a polarization controller to control the polarization state of the light incident on the electro-optic modulator. The polarization-optimized optical signal is intensity modulated by the microwave signal generated by a network analyzer. A second polarization controller is used to control the polarization state of the light before it enters the planar optical waveguide as regular SMF is used to interconnect the electro-optic modulator and the circulator and the circulator and the waveguides. This polarization controller is required as the waveguides are slightly birefringent and their spectral characteristics are therefore sensitive to the polarization of the light. The modulated optical signal is then fed to a delay line of the Bragg grating prism through an optical circulator. The reflected signal is then sent to a photodetector and the recovered microwave signal is analyzed by the network analyzer.

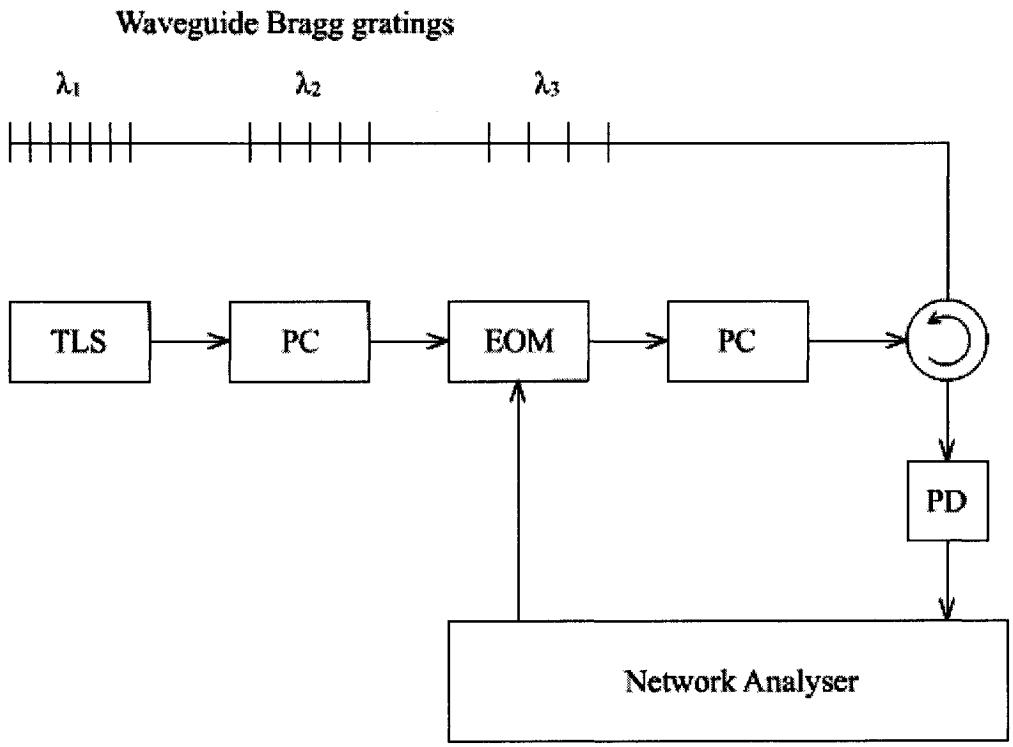

Fig. 4.10 Experimental setup of the waveguide-based photonic true time-delay beamforming module.

Table 4.3 gives the measured time delays for different microwave frequencies.

		Measured relative time delay with respect to center grating (ps)				
Grating number	Theoretical time delays (ps)	1 GHz	2 GHz	3 GHz	4 GHz	5 GHz
1	96.67	98	99	101	96	92
2	0.00	0.00	0.00	0.00	0.00	0.00
3	-96.67	-100	-97	-100	-94	-96
4	128.89	120	129	125	130	128
5	0.00	0.00	0.00	0.00	0.00	0.00
6	-128.89	-122	-136	-125	-127	-130
7	161.11	163	169	168	165	166
8	0.00	0.00	0.00	0.00	0.00	0.00
9	-161.11	-162	-162	-167	-161	-163
10	193.33	194	195	199	193	197
11	0.00	0.00	0.00	0.00	0.00	0.00
12	-193.33	-199	-201	-196	-195	-193

Table 4.3 Experimental measurement of the time delays relative to the center gratings in each delay line.

The time delays in Table 4.3 were calculated from the experimental measurements of the phase of the recovered microwave signal with respect to the microwave signal generated by the network analyzer. The network analyzer calculated the phase difference between the

generated and the recovered electrical signals. Using this value, the time delays can be calculated using Eq. 43.

$$\Delta\tau = \frac{\Delta\phi}{2\,\pi\,f_{RF}} \tag{43}$$

where $\Delta\phi$ is the phase difference and f_{RF} is the microwave frequency of the electrical signal.

Fig. 4.11 shows a graphical representation of the experimental and theoretical time delays.

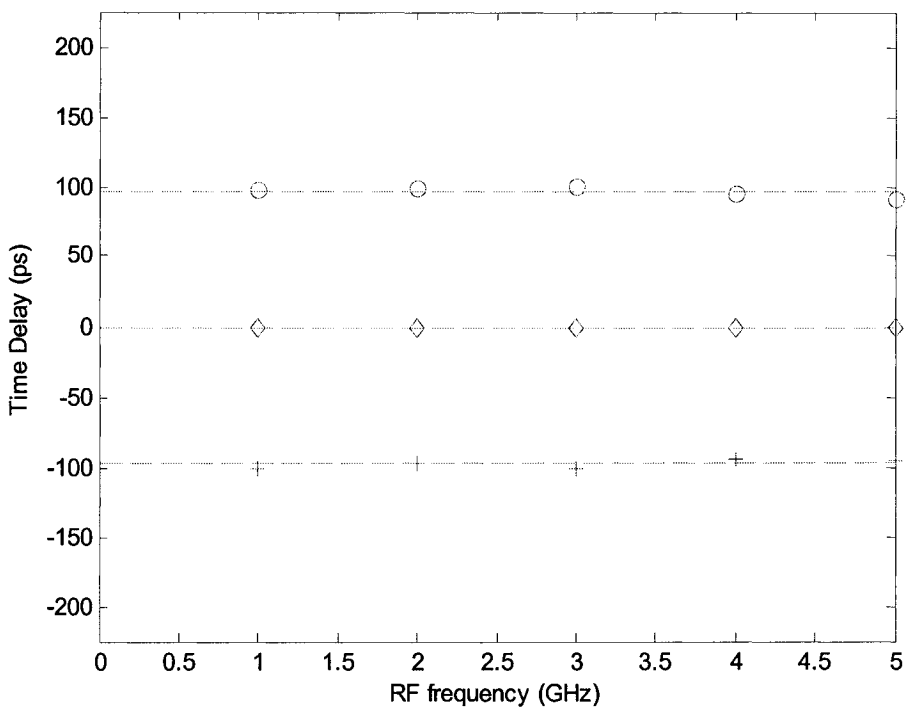

(a)

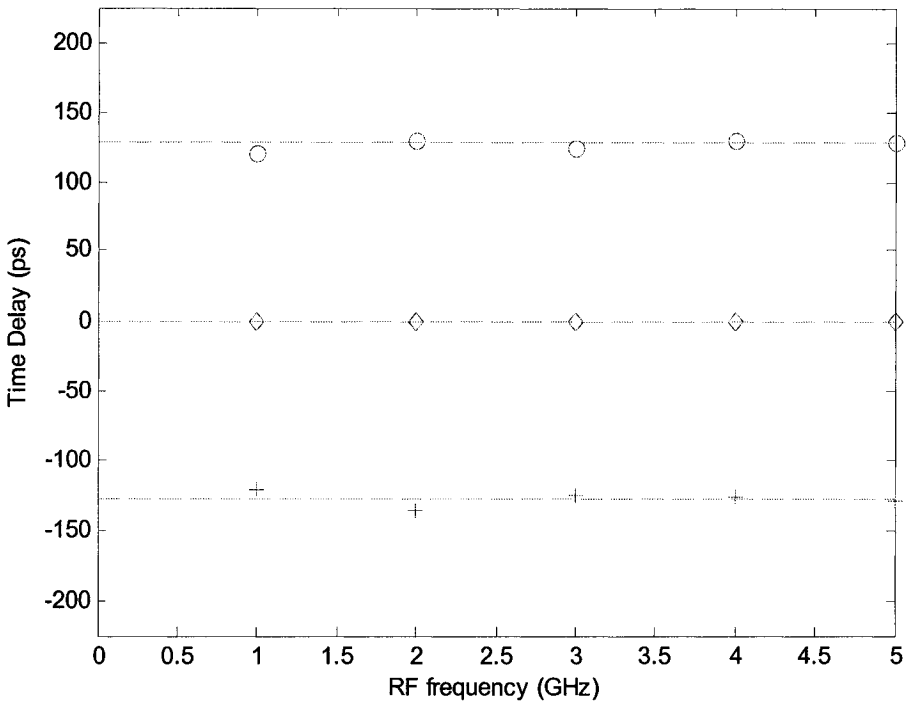
Time Delay (ps)
RF frequency (GHz)
200
150
100
50
0
-50
-100
-150
-200
0
0.5
1
1.5
2
2.5
3
3.5
4
4.5
5

(b)

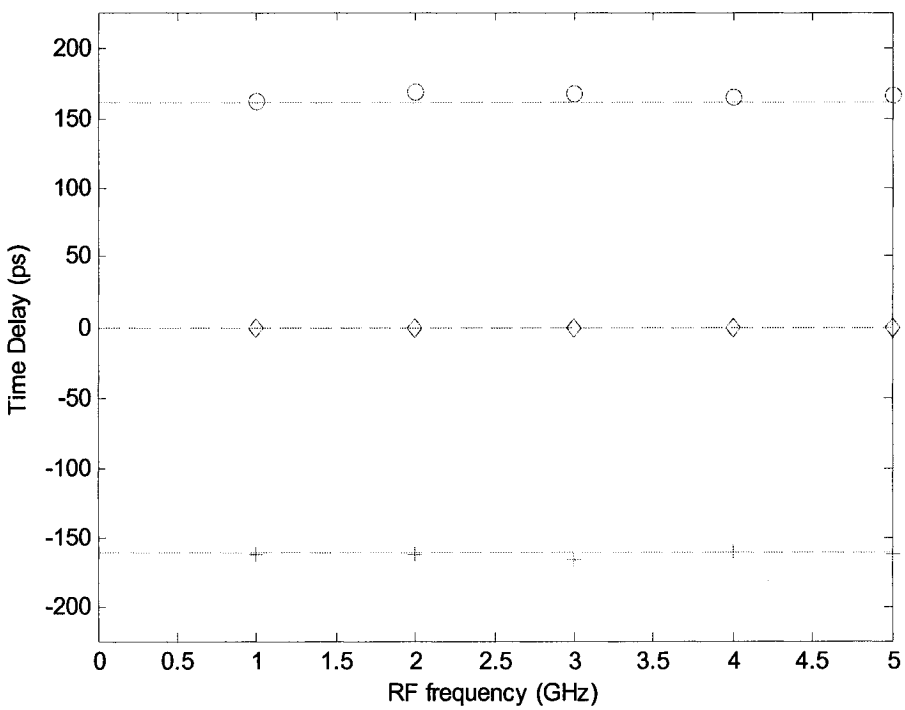
Time Delay (ps)
RF frequency (GHz)
200
150
100
50
0
-50
-100
-150
-200
0
0.5
1
1.5
2
2.5
3
3.5
4
4.5
5

(c)

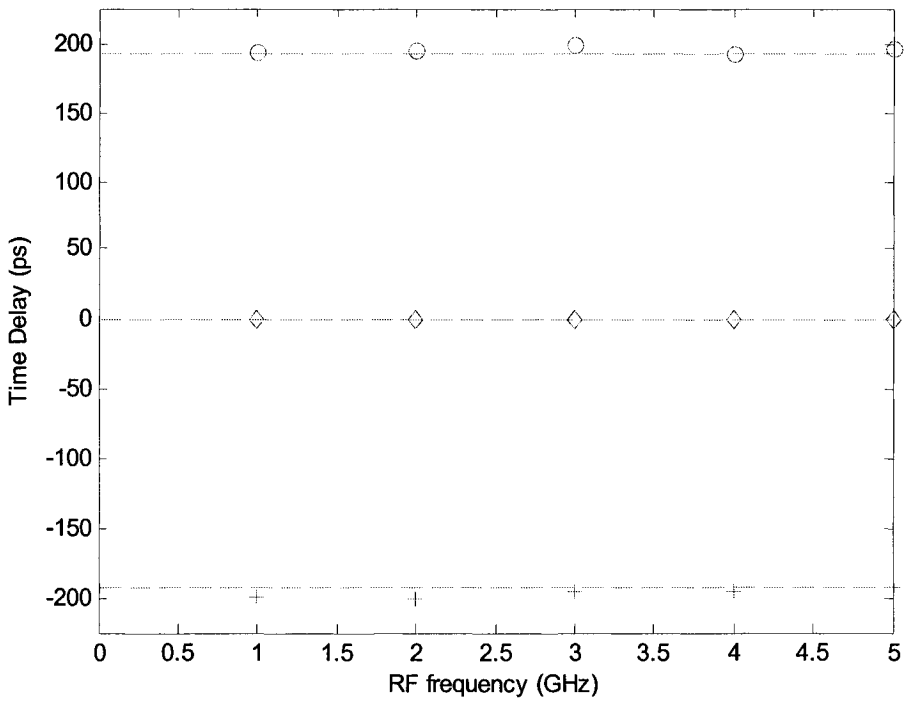

(d)

Fig. 4.11 (a)-(d) Experimental and theoretical time delays of the recovered microwave signal for the four waveguide delay lines. The markers indicate the experimental values, while the dashed line represents the theoretical value.

4.5 Radiation patterns

The measured time delays shown in Table 4.3 show that the delay line can provide accurate results for different microwave frequencies. The deviation between the experimental results and the theory can be caused by uncertainties in the parameters of the waveguides, errors in the time delay measurements and uncertainties in the positioning of the gratings during the fabrication of the Bragg grating prism. The following figures show the radiation pattern of a

4-element phased array antenna whose elements are fed electrical signals delayed by the photonic beamformer based on the experimental time delays when the microwave frequency is equal to 5 GHz. The spacing between the antenna elements is chosen to be equal to 30 mm in order to avoid grating lobes with a microwave carrier frequency of 5 GHz.

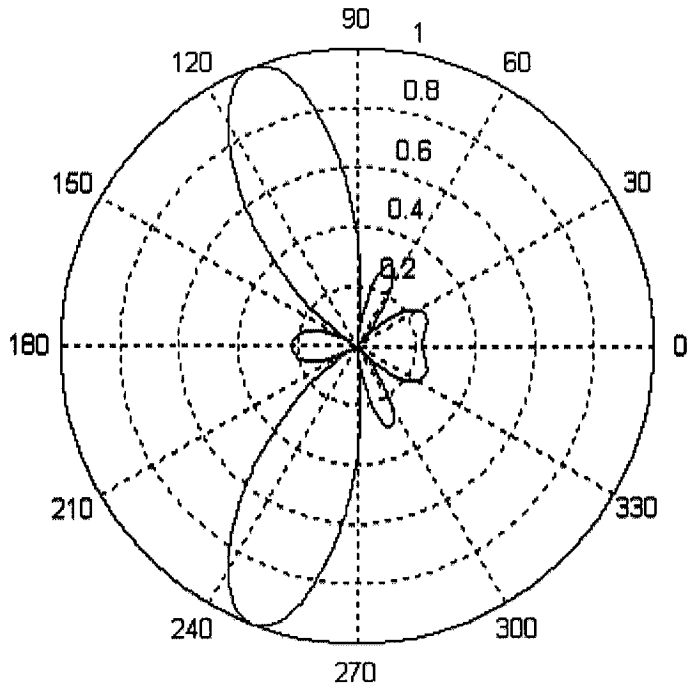

Fig. 4.12 Radiation pattern of a 4-element phased array antenna steered by the TTD beamformer when the optical carrier wavelength is equal to 1556 nm.

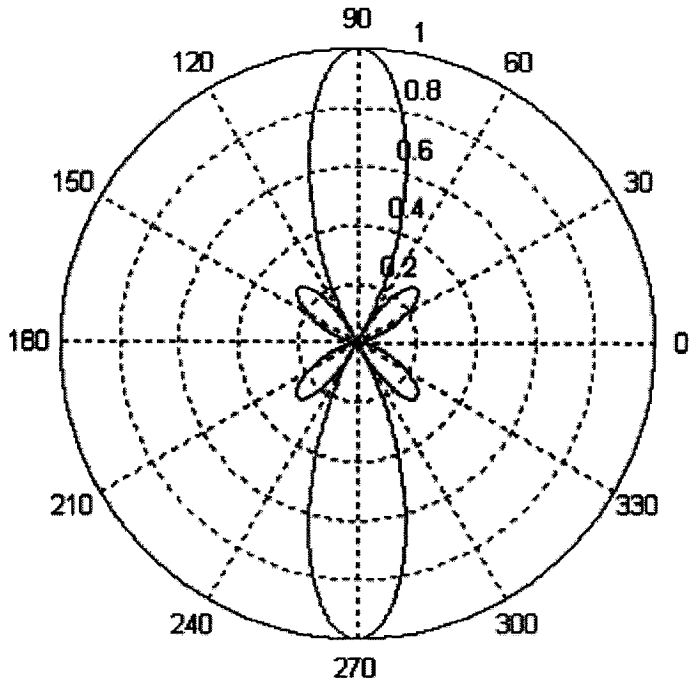

Fig. 4.13 Radiation pattern of a 4-element phased array antenna steered by the TTD beamformer when the optical carrier wavelength is equal to 1566 nm.

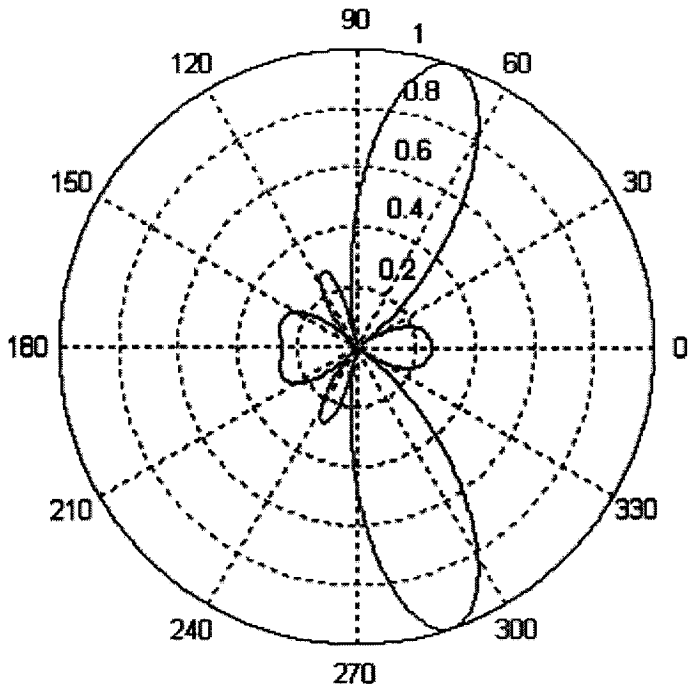

Fig. 4.14 Radiation pattern of a 4-element phased array antenna steered by the TTD beamformer when the optical carrier wavelength is equal to 1577 nm.

The radiation angles for the 5 GHz microwave frequency are equal to -110.5°, 90° and 70.9°. The broadside radiation direction (90° orientation from the array axis) occurs at an optical carrier wavelength of 1566 nm which is consistent with the theoretical analysis.

The span of the phased array antenna is limited to approximately ±20° from the broadside direction in this implementation. This limitation is caused by the length of the planar optical waveguide. Longer delay lines can produce longer time delay progressions which yields a larger scanning area for the phased array antenna.

4.6 Problems encountered and solutions

In order to write on planar optical waveguides, modifications had to be brought to the Bragg grating system used. Among the modifications made, a phase mask holder, a fiber holder and a waveguide holder were designed and realized as part of this research project. Also, a vertical linear translation stage was added to the fiber and waveguide holder section of the system in order to add one more degree of freedom when performing the alignment of the optical waveguide and the phase mask. In order to compensate for the extra height added to one section, all other sections of the system had to be lifted by the same amount. The following figures show the components developed.

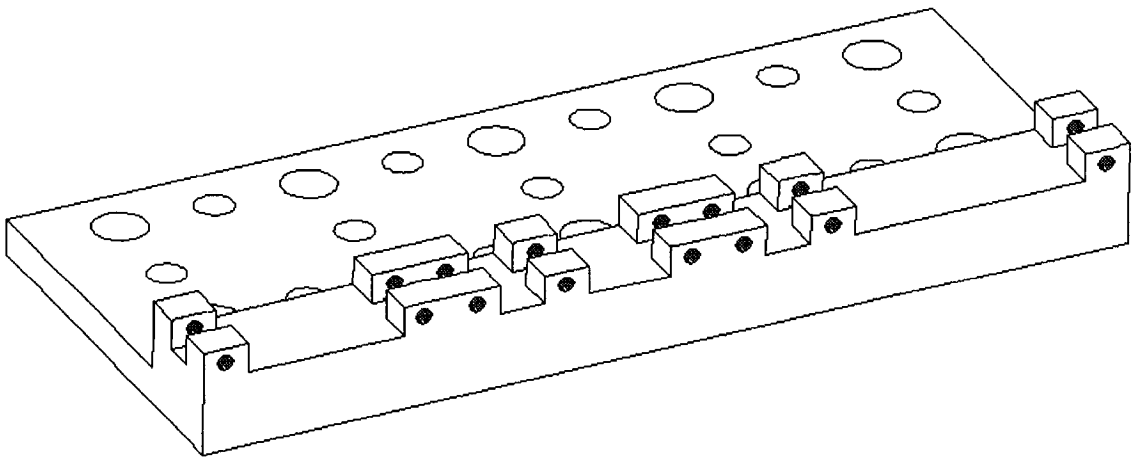

Fig. 4.15 Phase mask holder.

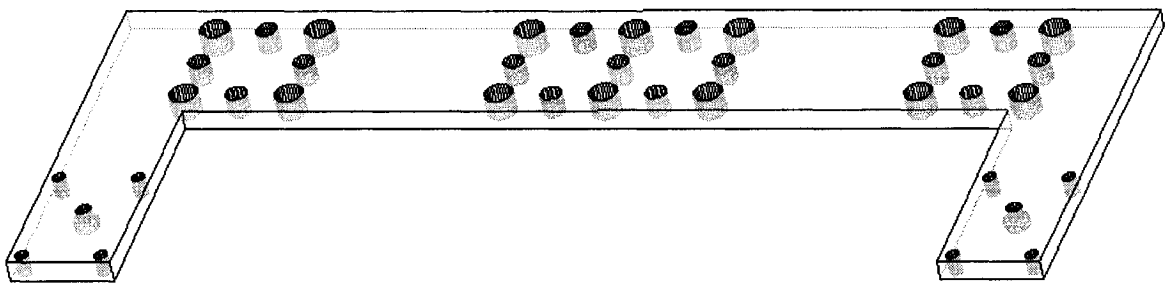

Fig. 4.16 Fiber chuck holder.

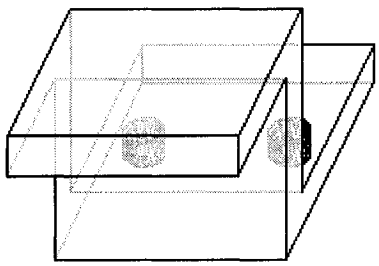

Fig. 4.17 Waveguide holder.

The photosensitivity of the planar optical waveguides was another issue that needed to be resolved in order to write Bragg gratings. It was found that the fluence of the Bragg writing system used in this research project was not high enough to write on the Ge-doped waveguides alone. In order to increase the photosensitivity, hydrogen loading was proposed. This was found to be sufficient to write Bragg gratings with a notch of 10-15 dB and more in their transmission spectrum. A hydrogen loading system was built as part of this project. Fig. 4.18 shows the schematic of the hydrogen loading system.

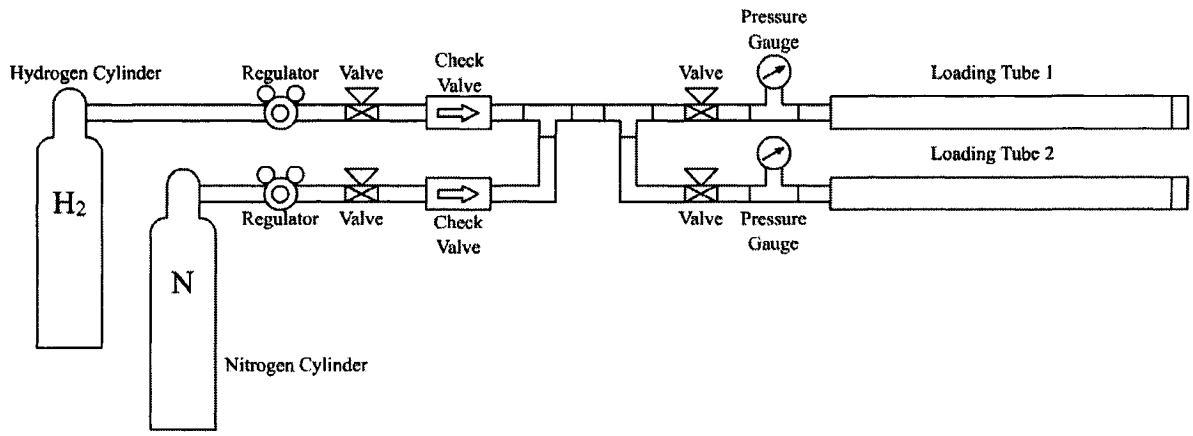

Fig. 4.18 Hydrogen loading system.

As can be seen from the figure, two loading tubes are present. These tubes can contain either optical fibers or planar optical waveguides. The width of the substrate of the planar optical waveguides is thus limited by the diameter of the loading tube. The nitrogen cylinder is used to remove any oxygen that enters the system upon inserting or removing optical fibers or waveguides.

The waveguides used in this project were fabricated at CRC using a general purpose photomask. This photomask gives a set of ten identical straight waveguides, separated by 75 μm. Since the waveguides are very close to one another, the alignment of the optical waveguides with respect to the phase mask and the UV beam was found to be another source of problem. Since the UV spot size is larger than the spacing between the optical waveguides, it was not possible to identify whether the UV beam was centered on one waveguide or between two waveguides just by looking at the diffraction in the reflection of the UV beam. This was not a problem for the two extremity waveguides (waveguides 1 and 10) but was an issue for the remaining waveguides (waveguides 2 to 9). For this research project, only the external waveguides were used in the fabrication of the waveguide Bragg grating prism in order to overcome the difficulty of the alignment of the waveguides with the phase mask and the UV beam.

The substrate on which the waveguides are deposited is relatively thin (< 0.5 mm), leading to a curvature along both x- and y-axis, as depicted in Fig. 4.19. A stress field present in the top cladding layer which is also responsible for the birefringence of the waveguides results in a bowing of the overall structure as the substrate is thin and thus not very resistant to this stress. Having a thicker substrate would bring more resistance to this stress field.

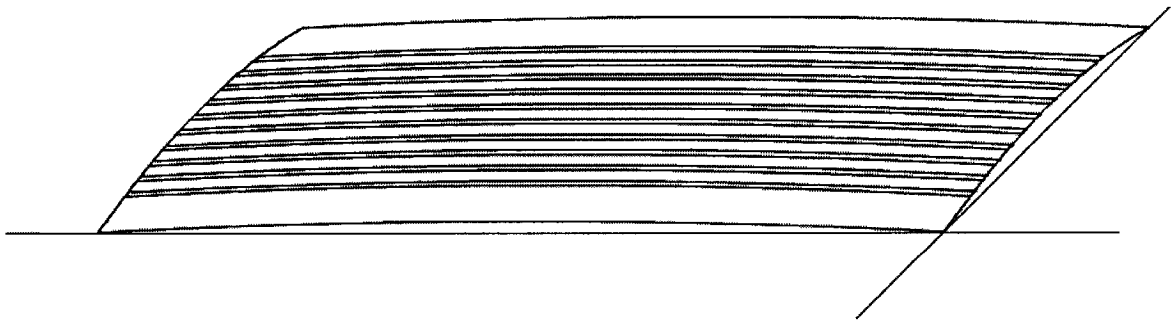

Fig. 4.19 Curvature of the substrate.

Writing Bragg gratings with this curvature would yield gratings that would be slightly apodized and chirped. In order to avoid this, the waveguides were glued to a uniformly flat piece of glass before the UV photoimprinting process. Pressure was applied in the center of the substrate in order to compensate for the bend. Since the glass would be in compression once the substrate is straight, the glass layer should not fracture. The only drawback of straightening the waveguides is an increased birefringence. Since the polarization state of light is controlled, the effect of this increased birefringence on the system performance would not be significant.

Another problem encountered concerned the coupling of light from an optical fiber to a planar waveguide and from the planar waveguide to the optical fiber. This problem was not found to be very insignificant when considering the transmission of light through the waveguide by butt-coupling two optical fibers at both extremities of the waveguide. The problem was more significant when trying to capture the light reflected by the Bragg gratings written on the waveguides. A high insertion loss from an optical fiber to the waveguide would be the principal cause of this problem. This resulted in a poor reflection spectrum

when characterizing the waveguide Bragg gratings. In order to overcome this problem, a lensed fiber was used. This lensed fiber has a far field divergence of 13.1° and 11.4° for the X and Y coordinates respectively. The results of the reflection spectrum of the waveguide Bragg grating array were improved, but were still "noisy". Further improvements can be obtained by using an index matching gel between the fiber and the waveguide.

4.7 Summary

In this chapter, the experimental results of a waveguide Bragg grating prism fabricated on planar integrated optical waveguides were presented. The waveguide Bragg grating prism implemented contained four delay lines with three Bragg gratings in each line. The optical performance of the waveguide Bragg grating prism developed has been evaluated and compared with theoretical results. The optical transmission and reflection spectrum of each delay line were presented and all gratings in the beamformer were characterized. The true time delays induced by each grating were measured and compared with the theoretical value based on the physical position of the gratings. A true time-delay beamformer using the waveguide Bragg grating prism was constructed and its performance were characterized and analyzed. Radiation pattern of a four-element phased array antenna were simulated considering the measured time delays. Finally, the problems and challenges encountered were detailed and solutions to these problems were presented.

Chapter 5

REMOTELY CONTROLLED PHASED ARRAY ANTENNA

This chapter details the mathematical model of a remotely controlled phased array antenna. The beamforming module considered is a true time-delay (TTD) beamforming network using a Bragg grating prism (BGP) on Ge-doped silica-on-silicon planar integrated optical waveguide. In such a scenario, the phased array antenna and the true time-delay beamforming module are located at a distance from the base station as shown in Fig. 5.1.

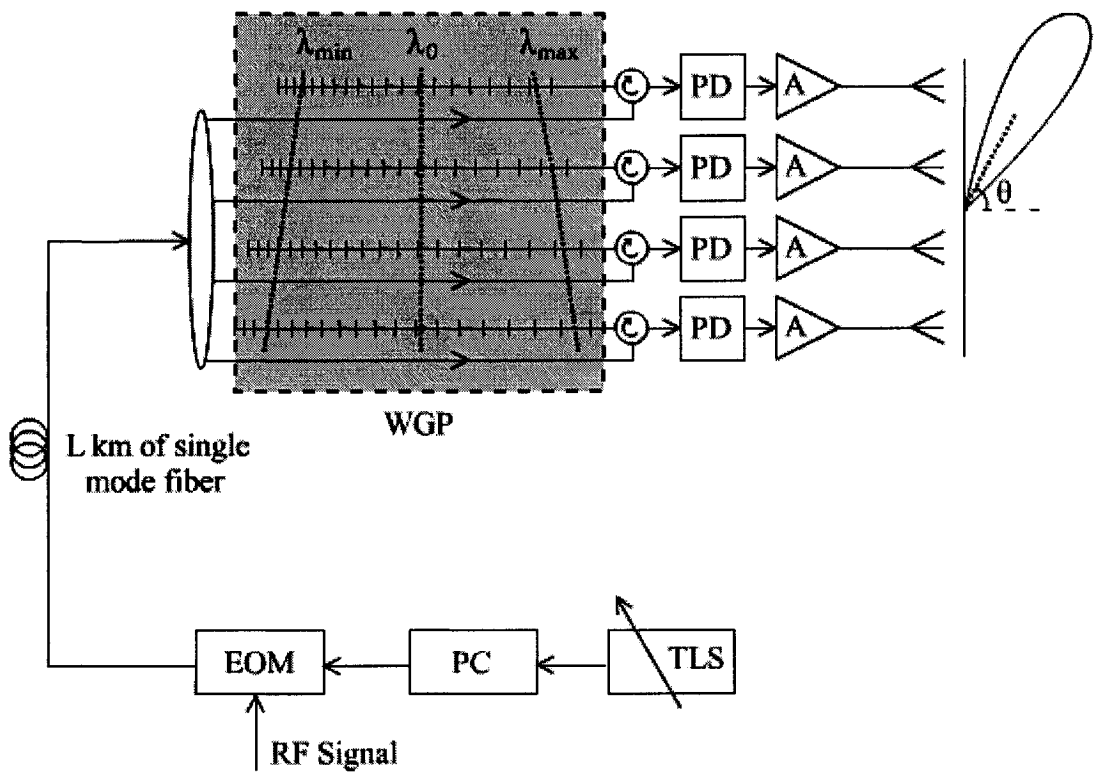

Fig. 5.1 Remotely controlled phased array antenna system.

The communication link used is a standard single mode fiber. When the length of the single mode fiber is significant, the effects of chromatic dispersion need to be taken under consideration [91] [93-94]. When using a conventional intensity modulation scheme, the relative phase differences between the carrier and the sidebands is not negligible and will lead to power degradation and an unexpected phase shift of the recovered microwave signal upon detection by a photodetector. It will be shown that this power penalty if a function of both the optical carrier wavelength and the microwave signal frequency.

This chapter will first introduce the mathematical equations used to model the photonic true time-delay beamforming module. It will be shown that the group delay response of the chirped gratings will lead to a power penalty at discrete wavelengths for a specified microwave frequency. The chromatic dispersion of the single mode fiber will be shown to cause another power penalty at discrete wavelengths for a specified frequency. The relationship between the power penalty caused by the group delay response of the chirped gratings, the optical carrier wavelength and the microwave frequency will be derived. Similarly, the relationship between the power penalty caused by chromatic dispersion for a given length of standard single mode fiber, the optical carrier wavelength and the microwave frequency will also be derived. Finally, the effects of chromatic dispersion on a true time-delay beamforming system will be derived when an optical single sideband modulation scheme [101-105] is used. It will be shown that the chromatic dispersion effects can be almost eliminated when such a modulation scheme is used.

5.1 Power spectrum of modulated optical signal

When an optical carrier is intensity modulated (IM) by an external electro-optic modulator, the normalized complex amplitude of the electric field can be expressed as

$$E_{\text{mod}} = \sqrt{1 + m\cos(\omega_m t)}\, E_{RF}\, e^{j(\omega_{RF} t + \phi_{RF})} \tag{44}$$

where E_{mod} denotes the output electric field of the EOM, m is the modulation index depth, ω_m is the modulation angular frequency, E_{RF}, ω_{RF}, and ϕ_{RF} are the amplitude of the electrical signal modulating the optical carrier, its frequency and its phase, respectively.

If we expand the mathematical expression of the amplitude of this intensity modulated signal into its Fourier series, we get

$$E_{RF}\sqrt{1 + m\cos(\omega_m t)} = E_{RF}\sum_{n=0}^{\infty} K_n \cos(n\omega_m t) \tag{45}$$

where $K_0 = \frac{1}{T}\int_0^T \sqrt{1 + m\cos\omega_m t}\; dt$ and

$$K_n = \frac{2}{T}\int_0^T \sqrt{1 + m\cos\omega_m t}\, \cos(n\omega_m t)\, dt, \qquad n = 1, 2, 3, \ldots$$

When m is small, the Fourier series can be approximated as

$$K_0 \approx 1$$
$$K_1 \approx \frac{m}{2}$$

and the higher order coefficients can be considered negligible. Under these conditions, when higher order harmonics can be neglected, the intensity modulated optical signal can be approximated by an amplitude modulated signal [106] as

$$E_{\text{mod}}(t) = 1 + m_a \cos(\omega_m t) E_{RF} e^{j(\omega_{RF} t + \phi_{RF})} \tag{46}$$

where m_a is the normalized amplitude modulation index.

It is well known that the Fourier transform of an amplitude modulated signal is given by

$$\begin{aligned} E_{\text{mod}}(\omega) &= E_{RF}\, \delta(\omega - \omega_m) e^{j\phi_{RF}} + \frac{m_a}{2} E_{RF}\, \delta(\omega - \omega_m - \omega_{RF}) e^{j\phi_{RF}} \\ &+ \frac{m_a}{2} E_{RF}\, \delta(\omega - \omega_m + \omega_{RF}) e^{j\phi_{RF}} \end{aligned} \tag{47}$$

From this equation, three frequency components are present at ω_0, $\omega_0 + \omega_m$ and $\omega_0 - \omega_m$. The first component is located at the carrier frequency and the two remaining components are the upper and lower sidebands respectively. This modulation type is also referred to as double sideband (DSB) modulation.

In the case where one of the sidebands is suppressed, the modulation is then referred to as single sideband modulation. Single sideband modulation in the optical domain can be achieved by using a dual electrode Mach-Zehnder modulator [102] [104]. The microwave electrical signal is applied to both electrodes with a $\pi/2$ phase shift difference. A DC bias voltage is applied to one electrode while the other one is grounded. Fig. 5.2 illustrates this optical single sideband modulator.

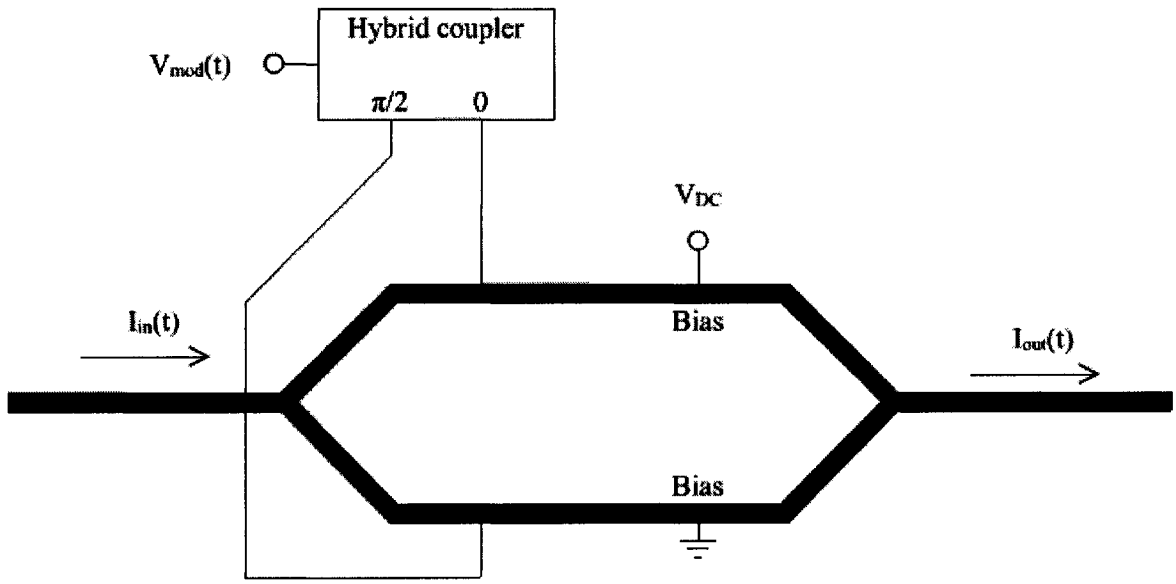

Fig. 5.2 SSB modulation scheme using a dual-electrode Mach-Zehnder modulator.

Following the same analysis procedure as described in Section 3.2 and considering the Mach-Zehnder modulator as two optical phase modulators with a DC voltage applied to one of the arms, the optical output signal, $I_{out}(t)$, is expressed as

$$I_{out}(t)=\frac{I_{in}}{2}\left\{\cos\left[\omega_m t+\frac{V_{DC}}{V_\pi}\pi+\frac{E_{RF}}{V_\pi}\pi\cos(\omega_{RF}t)\right]+\cos\left[\omega_m t+\frac{E_{RF}}{V_\pi}\pi\sin(\omega_{RF}t)\right]\right\} \quad (48)$$

where I_{in} is the amplitude of the optical signal at the input of the Mach-Zehnder modulator and V_{DC} is the bias voltage.

When the MZM is biased at quadrature, i.e. $\frac{V_{DC}}{V_\pi}=\frac{1}{2}$, and the amplitude of the microwave electrical signal is upper bounded as $E_{RF}<\frac{V_\pi}{\pi}$, Eq. 44 can be expressed as

$$I_{out}(t)=\frac{I_{in}}{2}\left\{J_0\left(\frac{E_{RF}}{V_\pi}\pi\right)\cos(\omega_m t)-J_0\left(\frac{E_{RF}}{V_\pi}\pi\right)\sin(\omega_m t)-2J_1\left(\frac{E_{RF}}{V_\pi}\pi\right)\cos[(\omega_m-\omega_{RF})t]\right\} \quad (49)$$

The power spectral density of Eq. 49 is given by

$$S_{I_{out}}(\omega)=\frac{I_{in}^{\ 2}}{4}J_0^{\ 2}\left(\frac{E_{RF}}{V_\pi}\pi\right)\pi\,\delta(\omega+\omega_m)+\frac{I_{in}^{\ 2}}{4}J_1^{\ 2}\left(\frac{E_{RF}}{V_\pi}\pi\right)\pi\,\delta(\omega+\omega_m-\omega_{RF}) \quad (50)$$

From this equation, two frequency components are present at ω_m and ω_m - ω_{RF}. The first component is located at the carrier frequency and the remaining component is the single sideband.

Another amplitude modulation scheme can be created by amplitude modulating the microwave signal. The double sideband modulated optical signal is then filtered in the optical domain such that only one of the sidebands is suppressed by the filter [102] [105]. Bragg gratings can be used for filtering the unwanted sideband.

5.2 Dispersion effects of a single mode fiber

A modulated optical signal propagating through an optical fiber of significant length will suffer from chromatic dispersion. When the frequency components of this modulated optical signal are recovered by a photodetector, the difference between the phases of each component may introduce a power penalty depending on the modulation scheme used [107-112]. The dispersion and group delay for a standard single mode fiber are given respectively by [94]

$$D(\lambda) = \frac{S_0}{4} \cdot \lambda \cdot \left[1 - \left(\frac{\lambda_0}{\lambda} \right)^4 \right] \tag{51}$$

$$\tau = \tau_0 + \frac{S_0}{8} \cdot \left(\lambda - \frac{{\lambda_0}^2}{\lambda} \right)^2 \tag{52}$$

where λ_0 is the zero-dispersion wavelength, S_0 is the maximum dispersion slope at λ_0 and τ_0 is a constant delay from the reference point.

The optical fiber considered in this analysis has a dispersion curve given in Fig. 5.3.

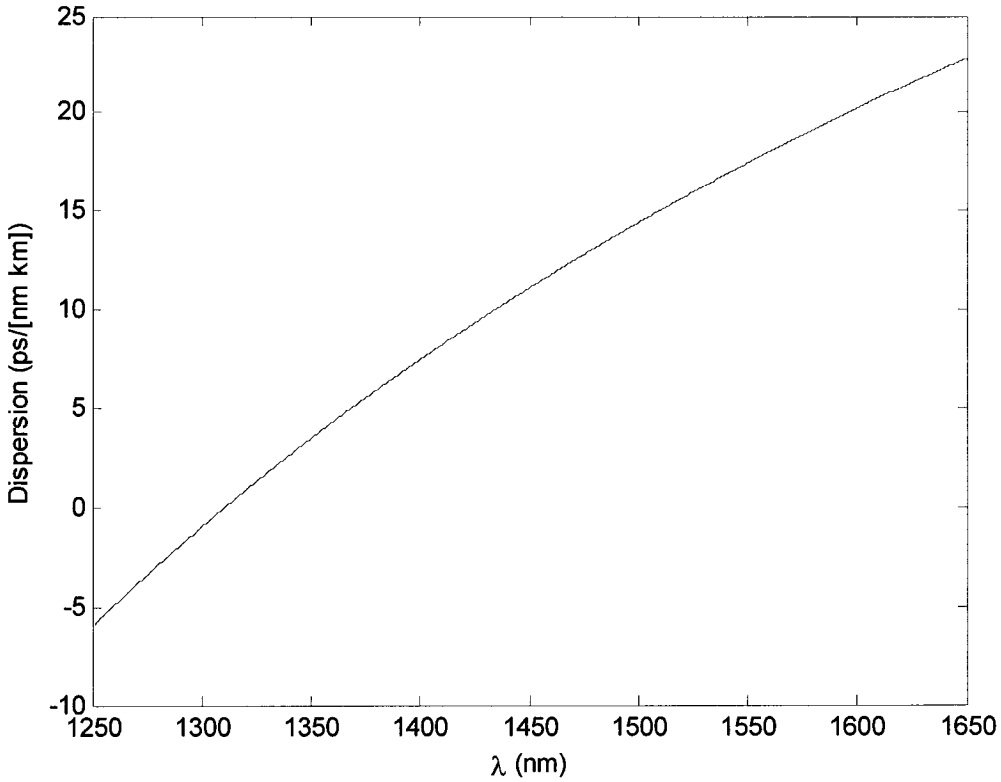

Fig. 5.3 Chromatic dispersion of a single mode fiber.

5.3 Dispersion caused by a chirped Bragg grating delay line

The Bragg grating prism under this theoretical investigation is composed of four chirped Bragg gratings designed to give a different true time-delay progression at different optical carrier frequencies. The parameters of the gratings are kept constant except for their length

and chirp rate to compensate for the difference in length as the total chirp of the gratings is kept constant. The time delay for light reflected off a uniform Bragg grating is

$$\tau_p = \frac{d\theta_p}{d\omega} = -\frac{\lambda}{2\pi c} \cdot \frac{d\theta_p}{d\lambda} \tag{53}$$

where θ_p is the phase of the amplitude reflection coefficient for different wavelengths.

When dealing with gratings with arbitrary coupling constant and chirp, no simple analytical solution exists. Also, these two variables cannot be separated as they collectively affect the transfer function of a given grating. For simulation purposes of the chirped gratings in this research project, the Transfer Matrix Method is used. This method was first used by Yamada in 1987 to analyze optical waveguides [73].

5.4 Recovered microwave signal by a photodetector

The photo current induced by a light wave reaching a photodetector is given by Eq. 40, as discussed in Section 3.4.

In the case of a remotely controlled phased array antenna, the intensity modulated optical signal reaching the photodetector is given by

$$E_{PD}(t) = E\rho_0 \cos(\omega_0 t + \theta_0) + \frac{m_a}{2} E\rho_1 \cos[(\omega - \omega_0 - \omega_m)t + \theta_1]$$
$$+ \frac{m_a}{2} E\rho_2 \cos[(\omega - \omega_0 + \omega_m)t + \theta_2] \quad (54)$$

where θ_0, θ_1, θ_2, ρ_0, ρ_1, ρ_2 represent the phase shifts caused by both the reflectivity of the Bragg grating and by the chromatic dispersion of the single mode fiber and the amplitude reflection introduced by the Bragg grating for all three frequency components.

When considering only frequencies centered around ω_m of the recovered microwave signal, we get

$$y(t) = \frac{1}{2} m_a E^2 \rho_1 \rho_2 \cos(\omega_m t + \theta_0 - \theta_1) + \frac{1}{2} m_a E^2 \rho_2 \rho_0 \cos(\omega_m t + \theta_2 - \theta_0) \quad (55)$$

Considering the following identity,

$$A\cos(\omega t + \phi_1) + B\cos(\omega t + \phi_2) =$$
$$\sqrt{A^2 + B^2 + 2AB\cos(\phi_2 - \phi_1)}\cos\left[\omega t + \arctan\left(\frac{A\sin(\phi_1) + B\sin(\phi_2)}{A\cos(\phi_1) + B\cos(\phi_2)}\right)\right] \quad (56)$$

We can express Eq. 55 as

$$y(t)=\frac{1}{2}m_a E^2 \rho_0 \sqrt{|\rho_1|^2+|\rho_2|^2+2|\rho_1\,\rho_2|\cos(\theta_2+\theta_1-2\theta_0)}\cdot$$
$$\cos\left[\omega_m\, t+\arctan\left(\frac{\rho_1\sin(\theta_0-\theta_1)+\rho_2\sin(\theta_2-\theta_0)}{\rho_1\cos(\theta_0-\theta_1)+\rho_2\cos(\theta_2-\theta_0)}\right)\right] \quad (57)$$

5.5 Evaluation of the dispersion effects

5.5.1 Evaluation of the dispersion effects induced by the waveguide Bragg grating prism

In this section, the effects of the dispersion induced by the waveguide Bragg grating prism are considered. The true time-delay beamforming system is considered in a relatively close proximity to the base station such that the effects of chromatic dispersion induced by a single mode fiber are negligible.

The following figures represent the reflection spectrum and the group delay of the four waveguide Bragg gratings composing the true time-delay beamforming module. The gratings simulated have a length from 10 to 25 mm, a total chirp of 9 nm and are uniformly apodized.

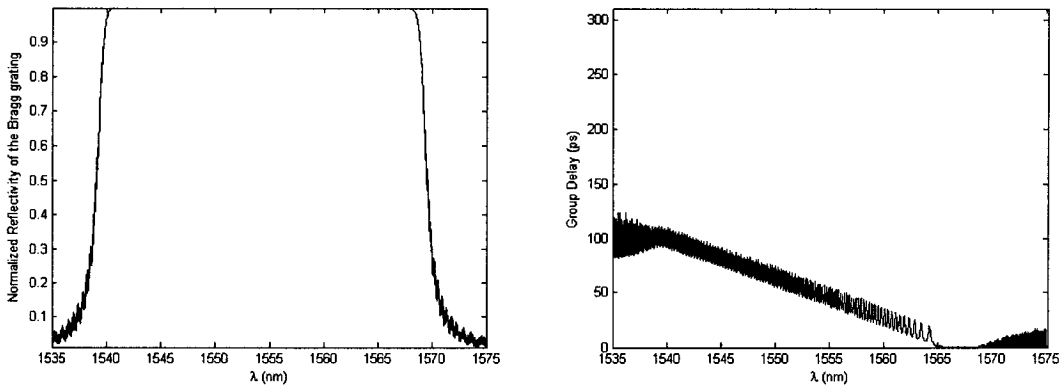

(a) (b)

Fig. 5.4 (a) Normalized reflectivity and (b) group delay of a 10-mm-long 9-nm chirp waveguide Bragg grating.

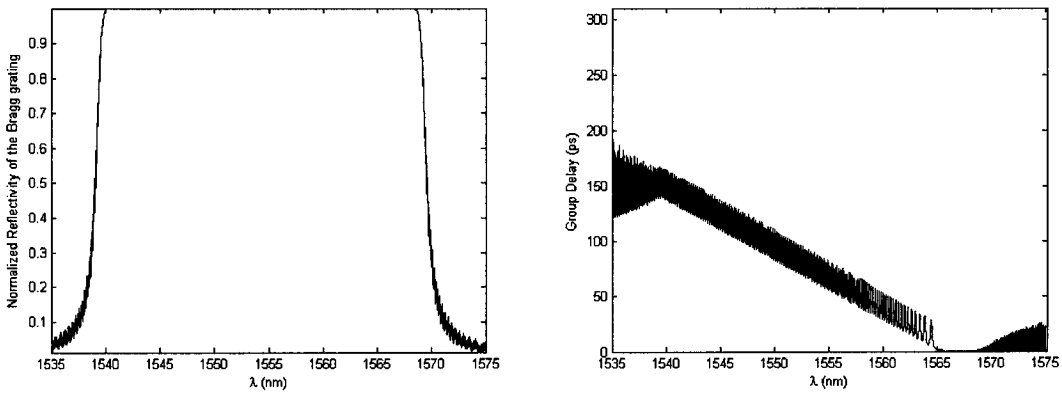

(a) (b)

Fig. 5.5 (a) Normalized reflectivity and (b) group delay of a 15-mm-long 9-nm chirp waveguide Bragg grating.

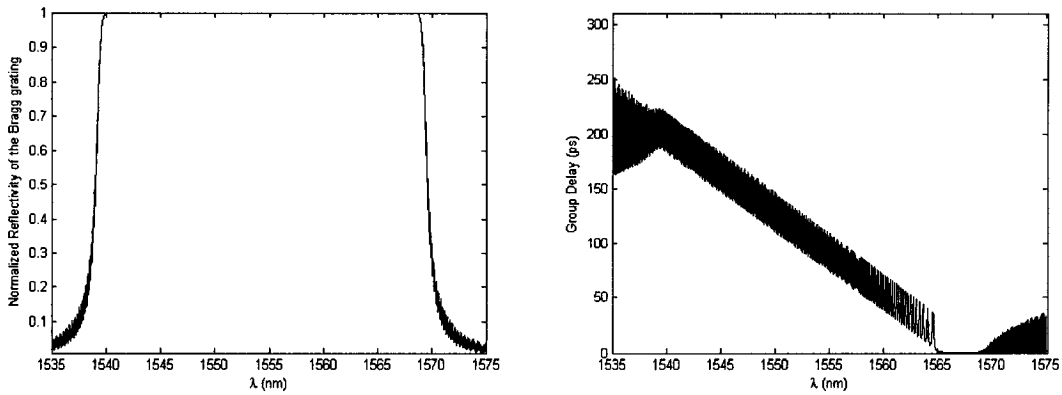

(a) (b)

Fig. 5.6 (a) Normalized reflectivity and (b) group delay of a 20-mm-long 9-nm chirp waveguide Bragg grating.

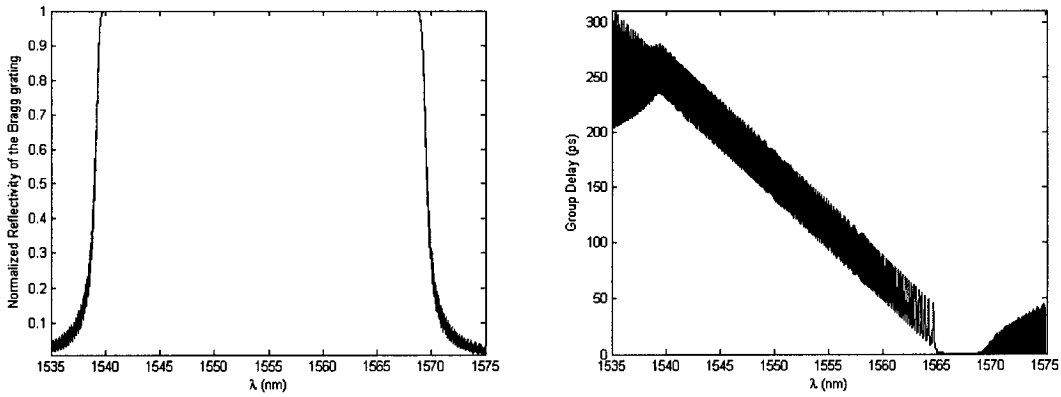

(a) (b)

Fig. 5.7 (a) Normalized reflectivity and (b) group delay of a 25-mm-long 9-nm chirp waveguide Bragg grating.

Using the simulation results for the four chirped Bragg gratings composing the true time-delay beamforming module, it is possible to find the electrical signal at the photodetector as a function of the optical wavelength. The following figures represent the electrical signal at

the output of the photodetector for a microwave carrier of 6 and 18 GHz using a DSB modulation scheme.

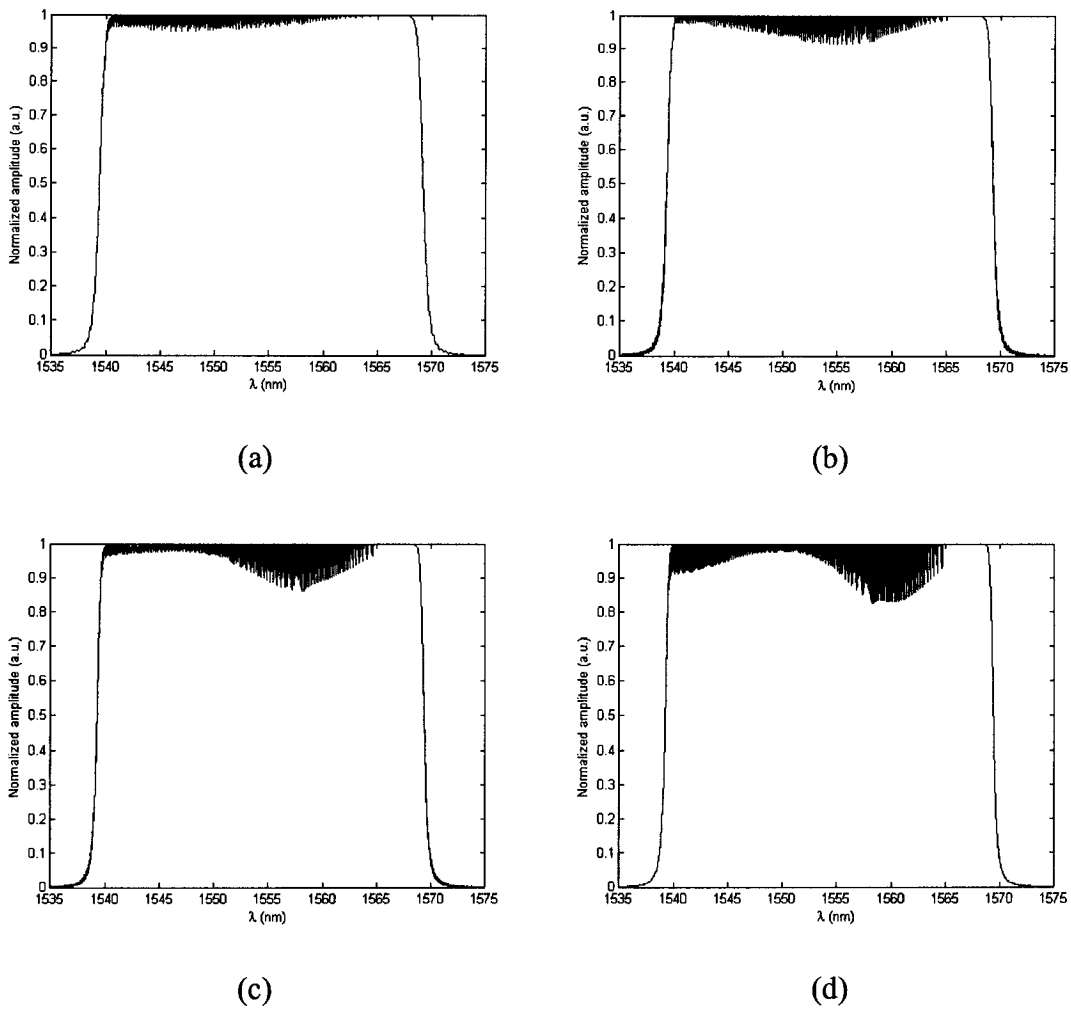

Fig. 5.8 Normalized amplitude of the recovered microwave signal delayed by a chirped grating of length of (a) 10 mm, (b) 15 mm, (c) 20 mm and (d) 25 mm when ω_m = 6 GHz and a DSB modulation scheme is used.

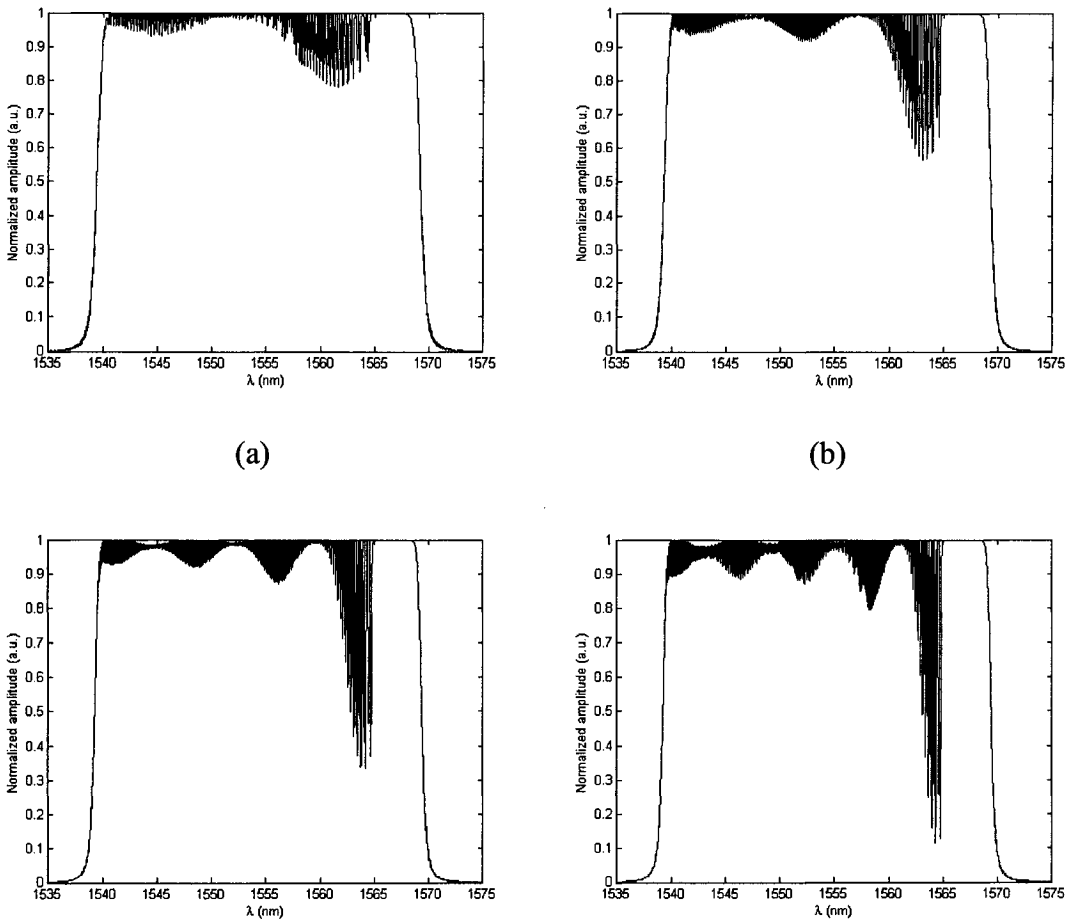

Fig. 5.9 Normalized amplitude of the recovered microwave signal delayed by a chirped grating of length of (a) 10 mm, (b) 15 mm, (c) 20 mm and (d) 25 mm when ω_m = 18 GHz and a DSB modulation scheme is used.

From Figs. 5.8 and 5.9, it is possible to notice that DSB modulation suffers important power penalties at discrete wavelengths for a given microwave frequency. This power penalty results from the beating of both sidebands with the carrier upon recovery of the electrical signal at the photodetector. When adding the signals resulting from this beating, important power losses are observed when the signals are almost completely out of phase.

When double sideband modulation is used, the angle of the main beam of the phased array antenna as a function of the optical carrier wavelength is displayed in Fig. 5.10.

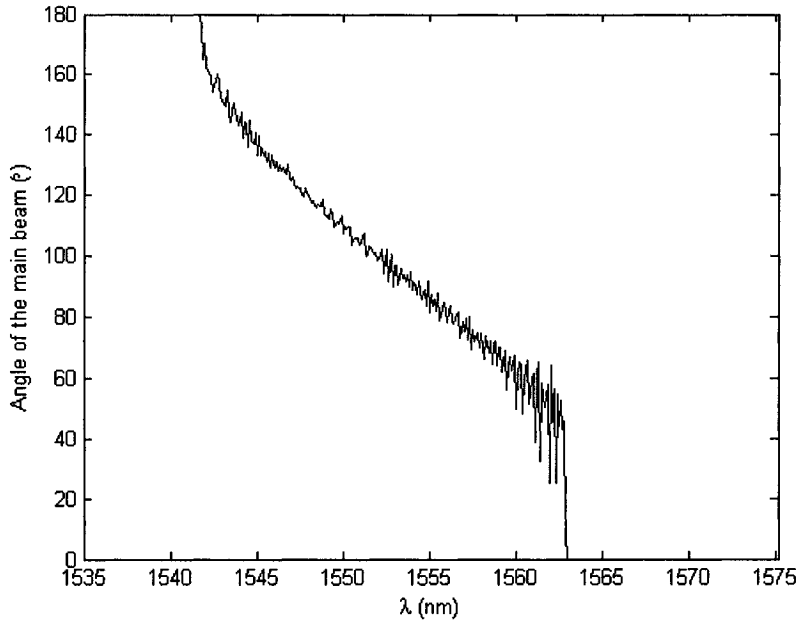

(a)

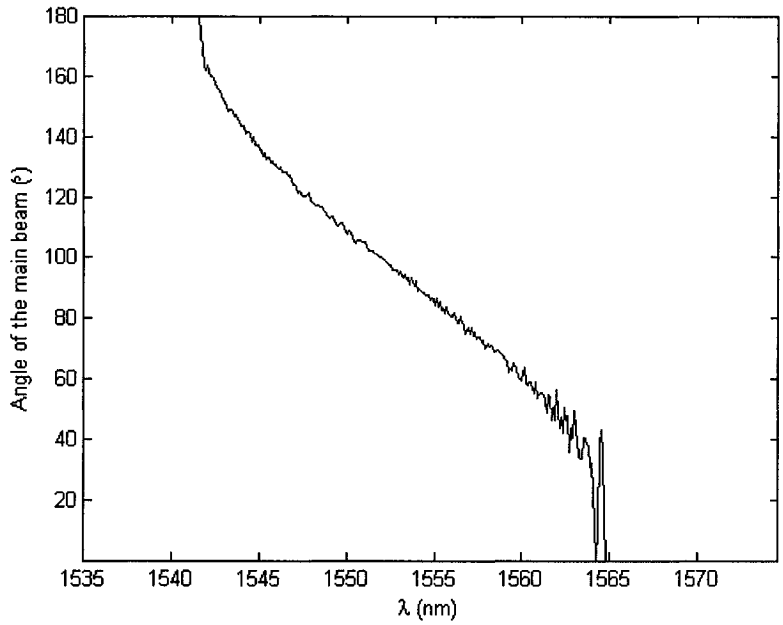

(b)

Fig 5.10 Angle of the mainlobe of the phased array antenna when double sideband modulation is used with (a) ω_m = 6 GHz and (b) ω_m = 18 GHz.

By observing Fig. 5.10 (a) and (b), it is worth noting that the ripple in the angle of the main lobe as a function of the optical carrier wavelength is less significant when a larger microwave frequency is used. In general, the phase response of the gratings is improved when DSB modulation is used. The group delay ripple of a chirped Bragg grating is significantly reduced as a consequence of the modulation by the electrical signal. At higher modulation frequencies, the effects are more significant. This is translated directly on the angle of the mainlobe of the PAA which depends directly to the group delay induced by the Bragg gratings. Thus, a higher frequency microwave signal produces a smoother operation curve of the angle of the main lobe as a function of the optical wavelength. This is confirmed in Fig. 5.10 (a) and (b).

The following figures represent the electrical signal at the output of the photodetector for a microwave carrier of 6 and 18 GHz using an SSB modulation scheme.

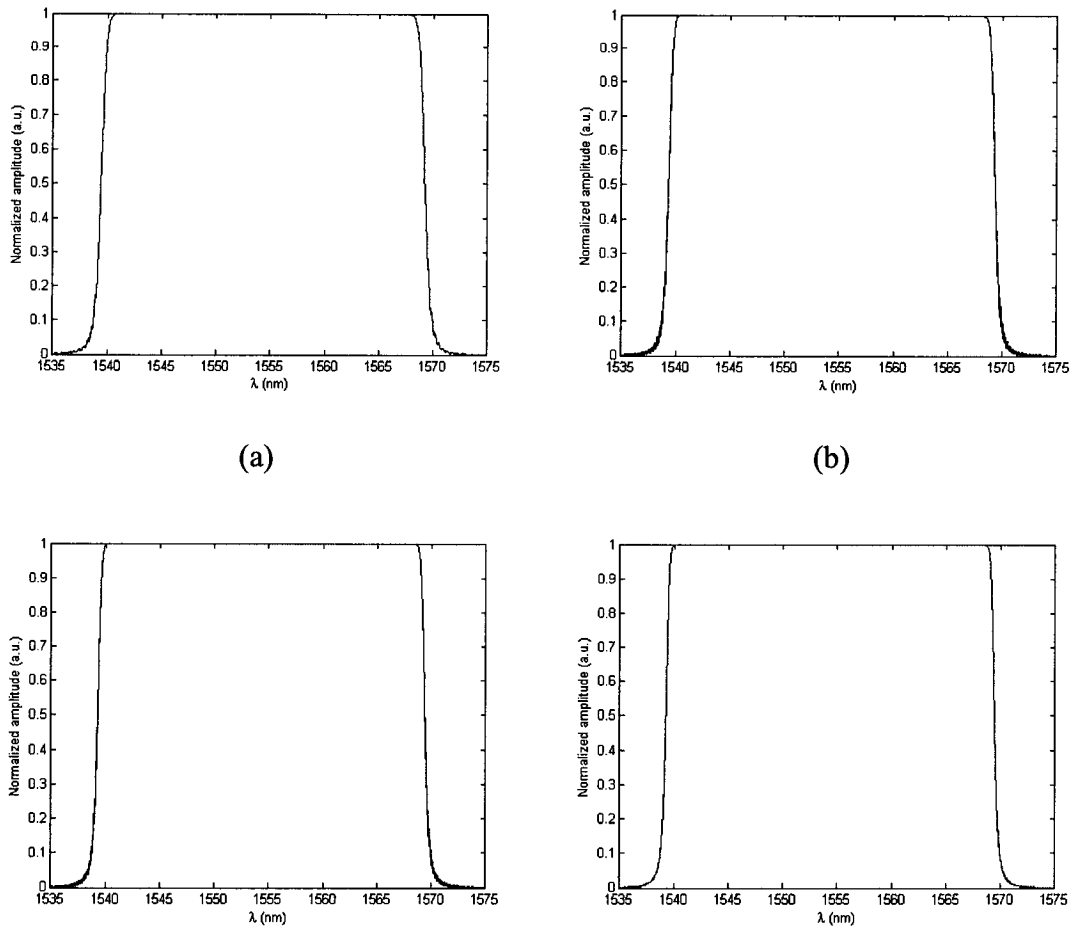

Fig. 5.11 Normalized amplitude of the recovered microwave signal delayed by a chirped grating of length of (a) 10 mm, (b) 15 mm, (c) 20 mm and (d) 25 mm when ω_m = 6 GHz and an SSB modulation scheme is used.

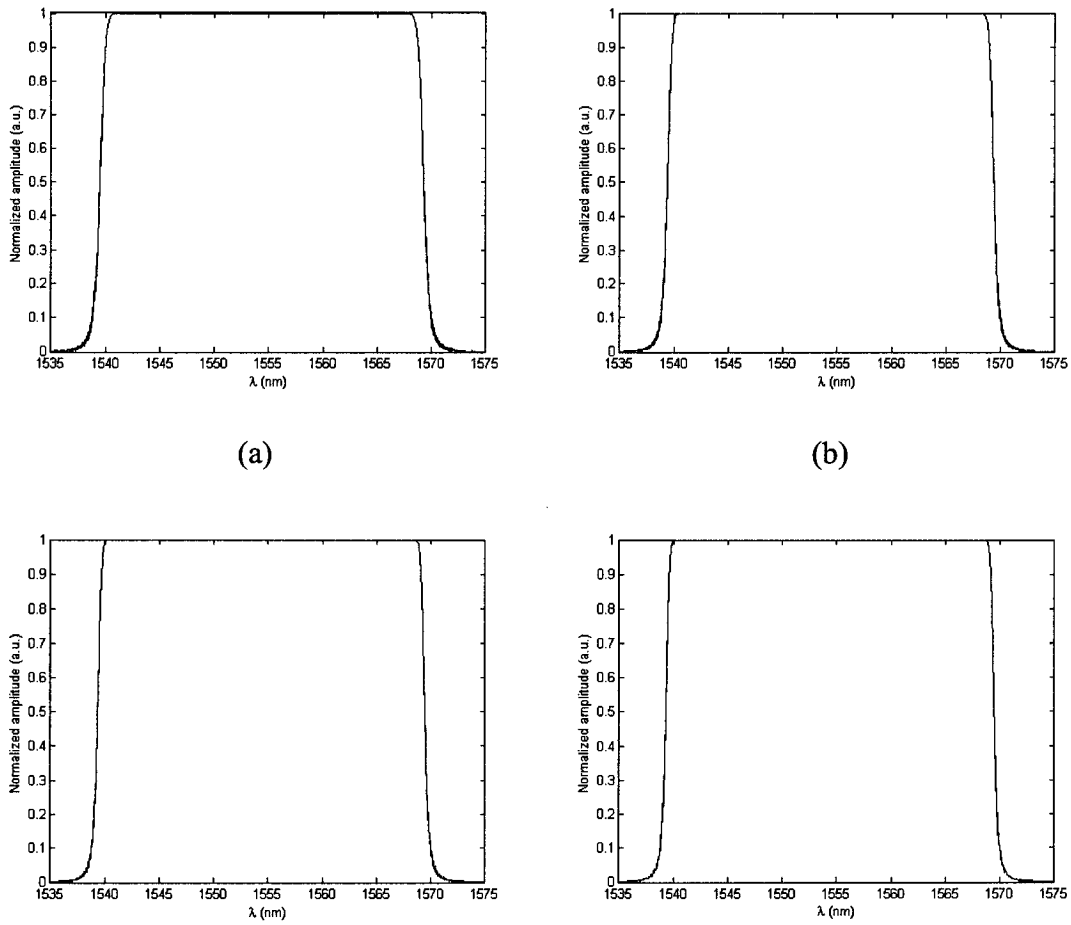

Fig. 5.12 Normalized amplitude of the recovered microwave signal delayed by a chirped grating of length of (a) 10 mm, (b) 15 mm, (c) 20 mm and (d) 25 mm when ω_m = 18 GHz and an SSB modulation scheme is used.

From Figs. 5.11 and 5.12, it is possible to notice that the power penalty present when a DSB modulation scheme is used is absent when an SSB modulation scheme is used for any microwave frequency and any optical carrier wavelength. No power penalty is possible as only one sideband can beat with the optical carrier upon recovery of the electrical signal at the photodetector. The two figures present a strong and flat reflection characteristic.

When single sideband modulation is used, the angle of the main beam of the phased array antenna as a function of the optical carrier wavelength is displayed in Fig. 5.13.

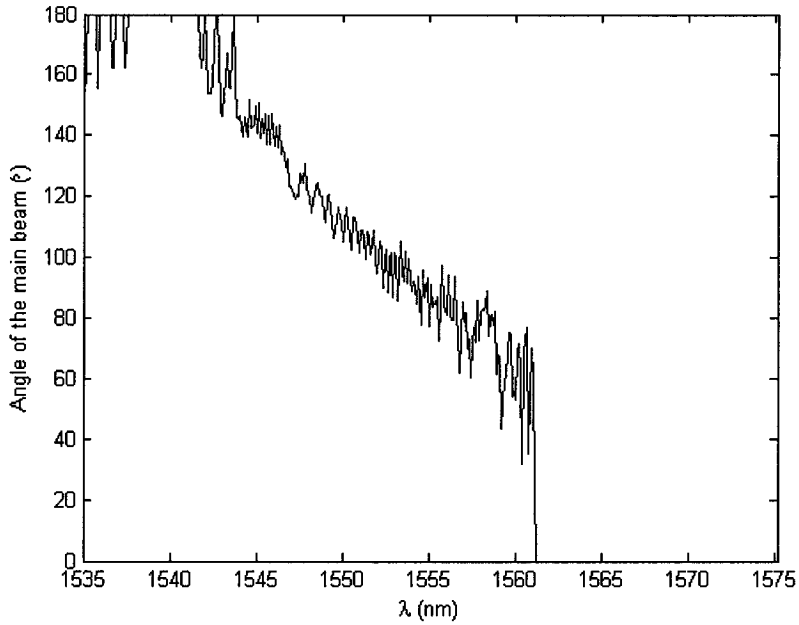

(a)

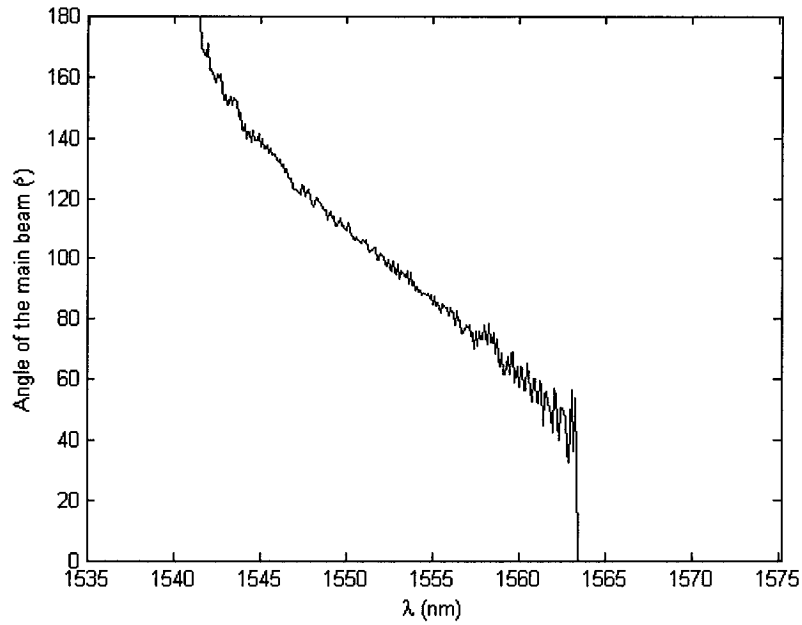

(b)

Fig 5.13 Angle of the main lobe of the phased array antenna when single sideband modulation is used with (a) ω_m = 6 GHz and (b) ω_m = 18 GHz.

From Fig. 5.13 (a) and (b), it is worth noting that the ripple in the angle of the main lobe as a function of the optical carrier wavelength is more significant for both microwave frequencies when an SSB modulation scheme is used when compared to the results in Fig. 5.10 where a DSB modulation scheme was used. On the other hand, a similar tendency is noted concerning the microwave frequency used: the higher the modulation frequency, the smoother the curve of the angle of the main lobe as a function of the main lobe.

5.5.2 Evaluation of the chromatic dispersion effects induced by the single mode fiber

In this section, the effects of the dispersion induced by the single mode fiber are considered. The true time-delay beamforming system considered is linked to the base station with a length of optical fiber such that the effects of chromatic dispersion induced by a single mode fiber are considerable.

The following figures represent the electrical signal at the output of the photodetector for a microwave carrier of 18 GHz using a DSB modulation scheme, a length L = 10km of single mode fiber.

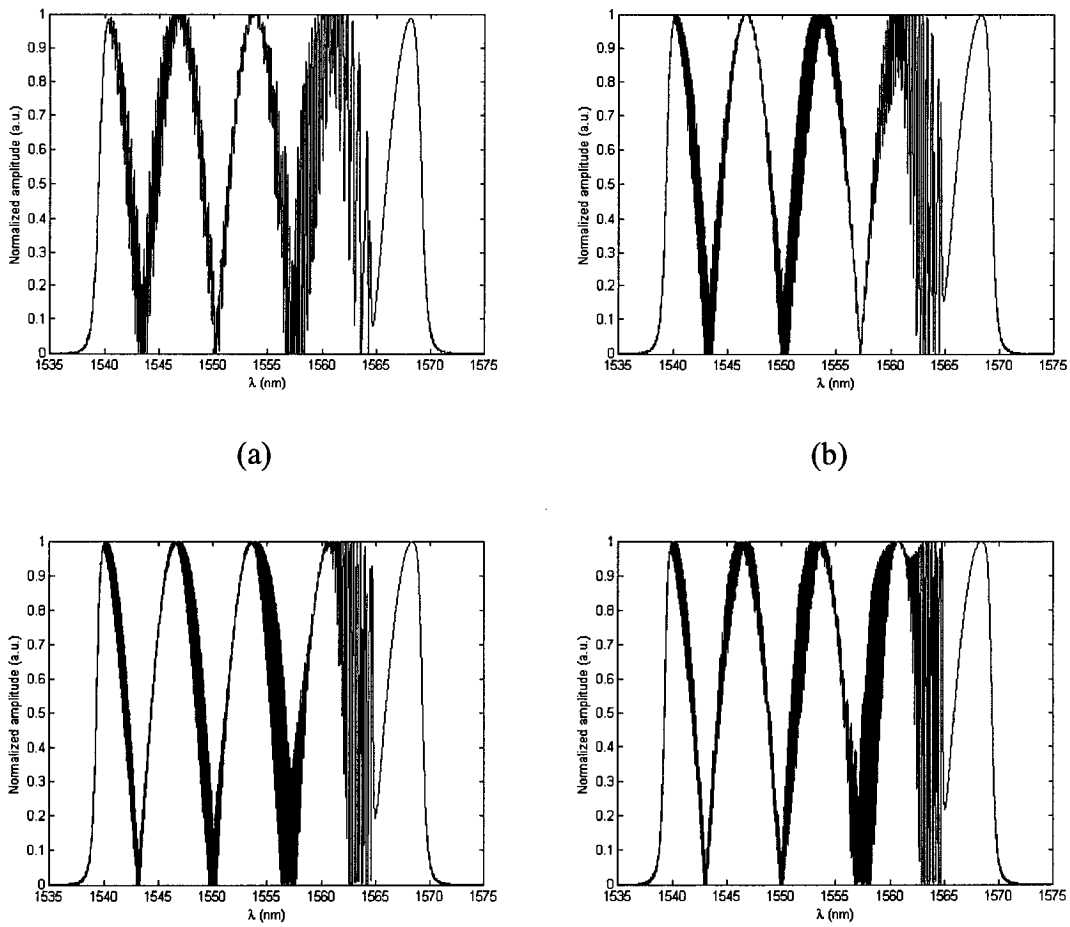

Fig. 5.14 Normalized amplitude of the microwave signal delayed by a chirped grating of length of (a) 10 mm, (b) 15 mm, (c) 20 mm and (d) 25 mm when ω_m = 18 GHz, a DSB scheme is used and the signal has propagated through 10 km of single mode fiber.

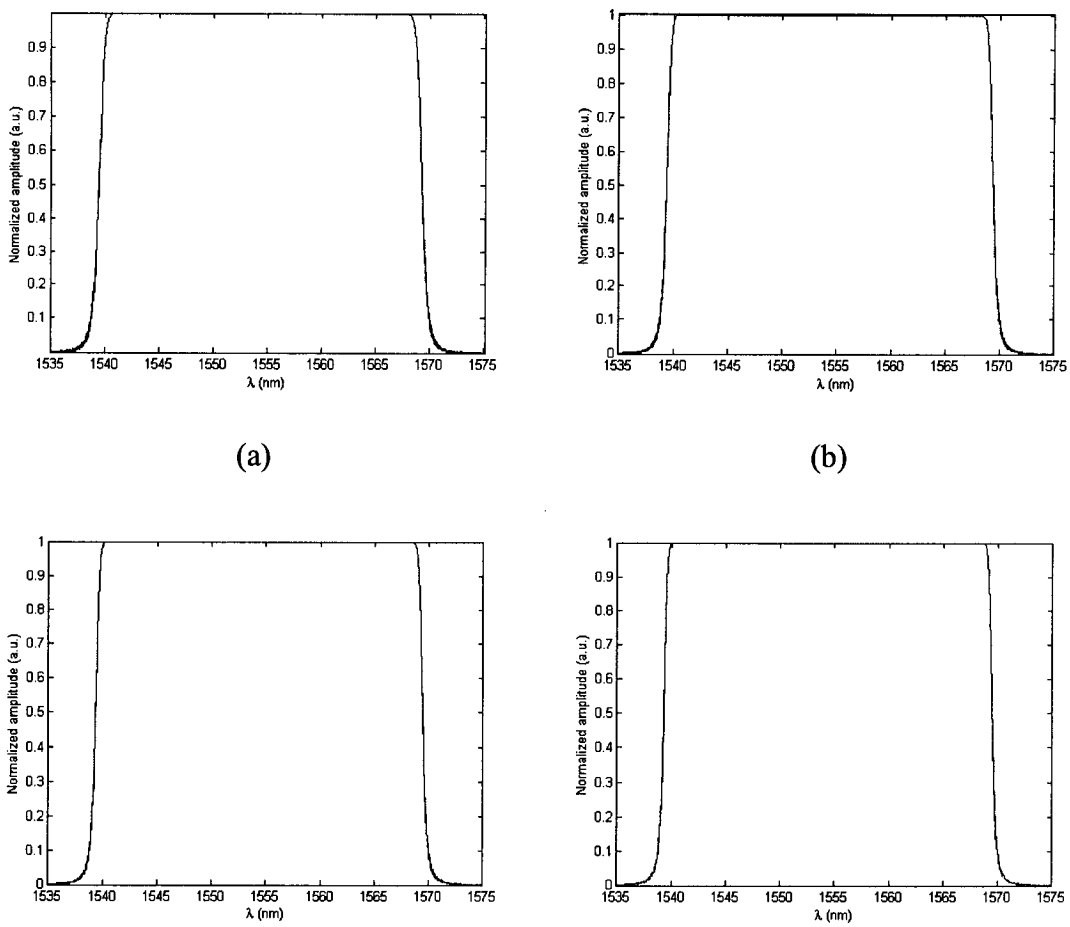

Fig. 5.15 Normalized amplitude of the microwave signal delayed by a chirped grating of length of (a) 10 mm, (b) 15 mm, (c) 20 mm and (d) 25 mm when ω_m = 18 GHz, an SSB scheme is used and the signal has propagated through 10 km of single mode fiber.

When analyzing the curves of the normalized amplitude of the recovered microwave signal when a DSB modulation scheme is used, as depicted in Fig. 5.14 (a)-(d), the same power penalty caused by the effects of the group delay ripple of the grating can be seen. On top of that, the effects of chromatic dispersion of the SMF can be seen. It is shown in the figures as a slowly varying power penalty as a function of the wavelength. In the case of 10 km of

SMF with an electrical carrier frequency of 18 GHz, four notches caused by the chromatic dispersion of the SMF can be seen in the pass band of the chirped Bragg gratings. This worsens the overall operation of the beamformer as it reduces significantly the number of operable wavelength, thus the number of possible angles for the phased array antenna. When an SSB modulation scheme is used, no power penalty is seen throughout the entire pass band of the chirped Bragg gratings. Thus, the effects of the group delay ripple of the gratings and the chromatic dispersion of the SMF do not affect the operation of the PAA beamformer when an SSB modulation scheme is used.

When the single mode fiber has a length of 10 km, the angle of the main beam of the phased array antenna as a function of the optical carrier wavelength is displayed in Fig. 5.16.

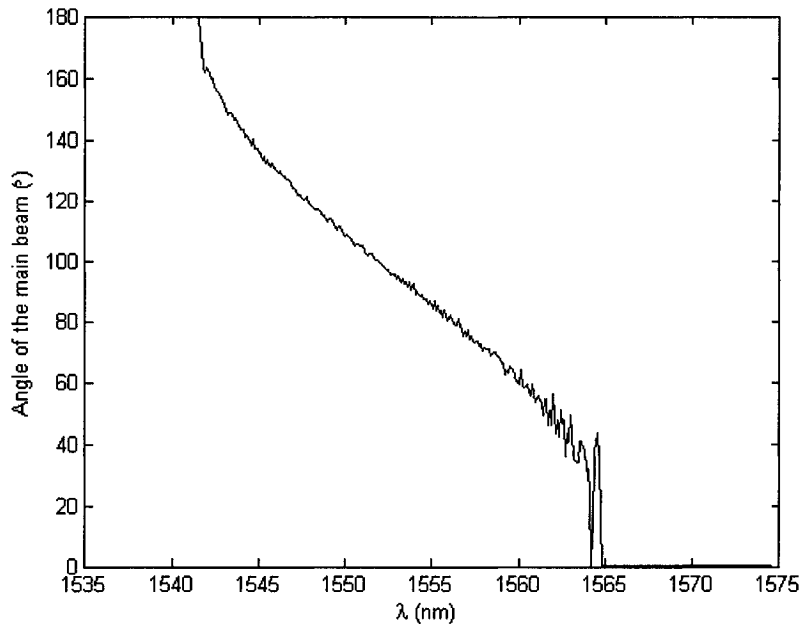

(a)

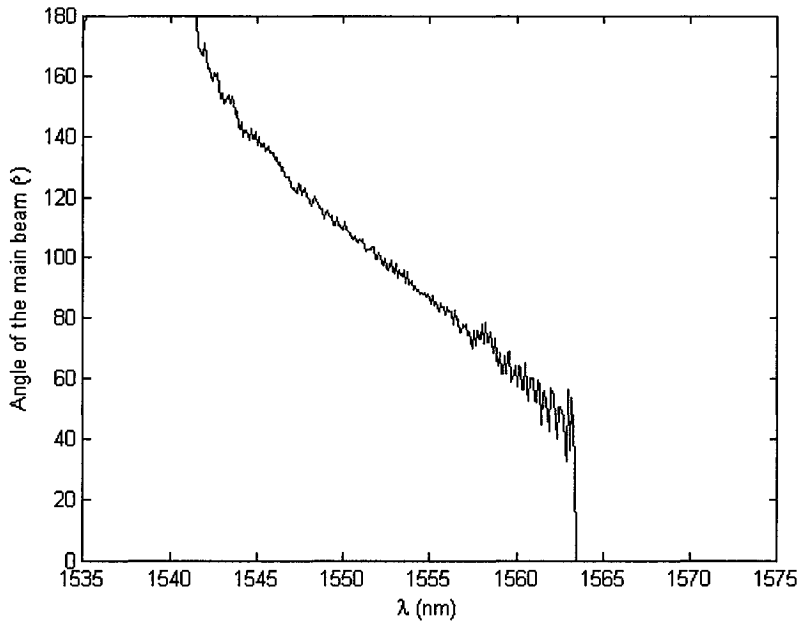

(b)

Fig 5.16 Angle of the main lobe of the phased array antenna when ω_m = 18 GHz, L = 10km and (a) double sideband- (b) single sideband- modulation is used.

The following figures represent the electrical signal at the output of the photodetector for a microwave carrier of 18 GHz using a DSB modulation scheme, a length L = 25 km of single mode fiber.

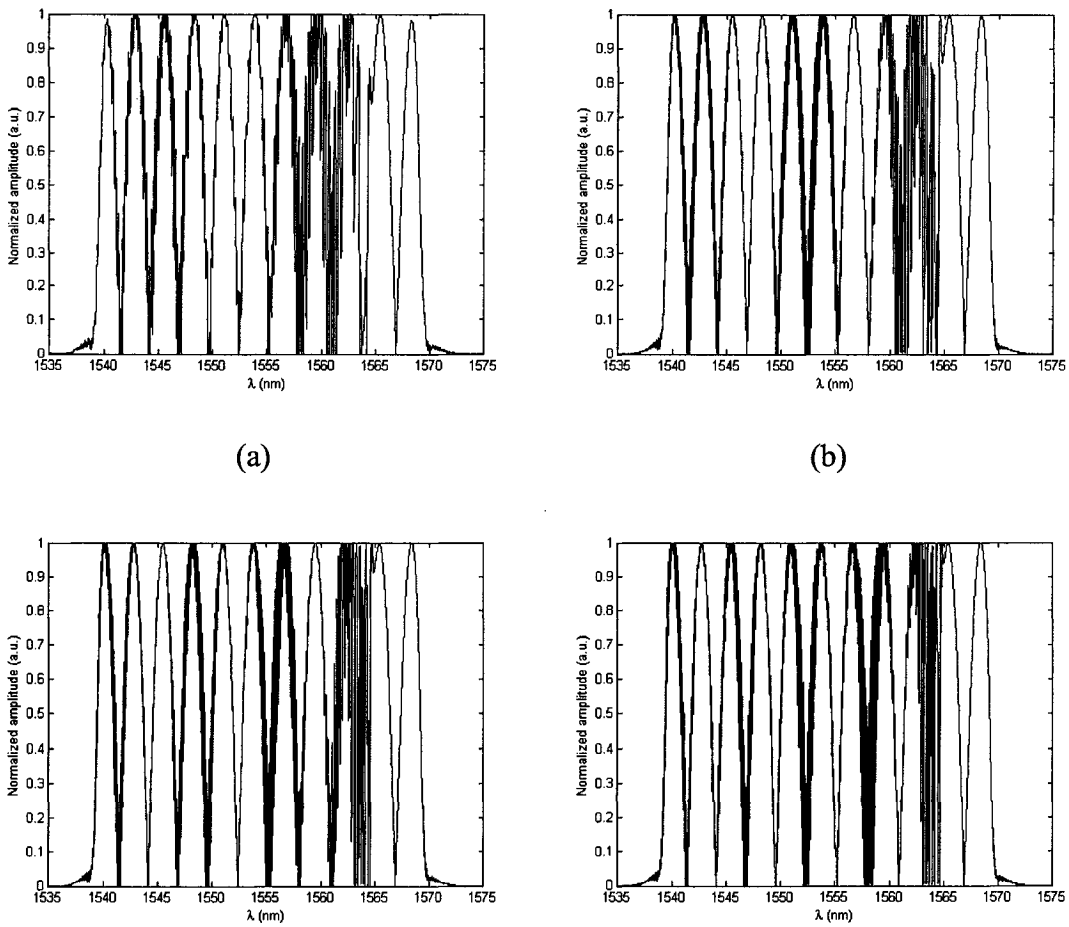

Fig. 5.17 Normalized amplitude of the microwave signal delayed by a chirped grating of length of (a) 10 mm, (b) 15 mm, (c) 20 mm and (d) 25 mm when ω_m = 18 GHz, a DSB modulation scheme is used and L = 25 km of single mode fiber.

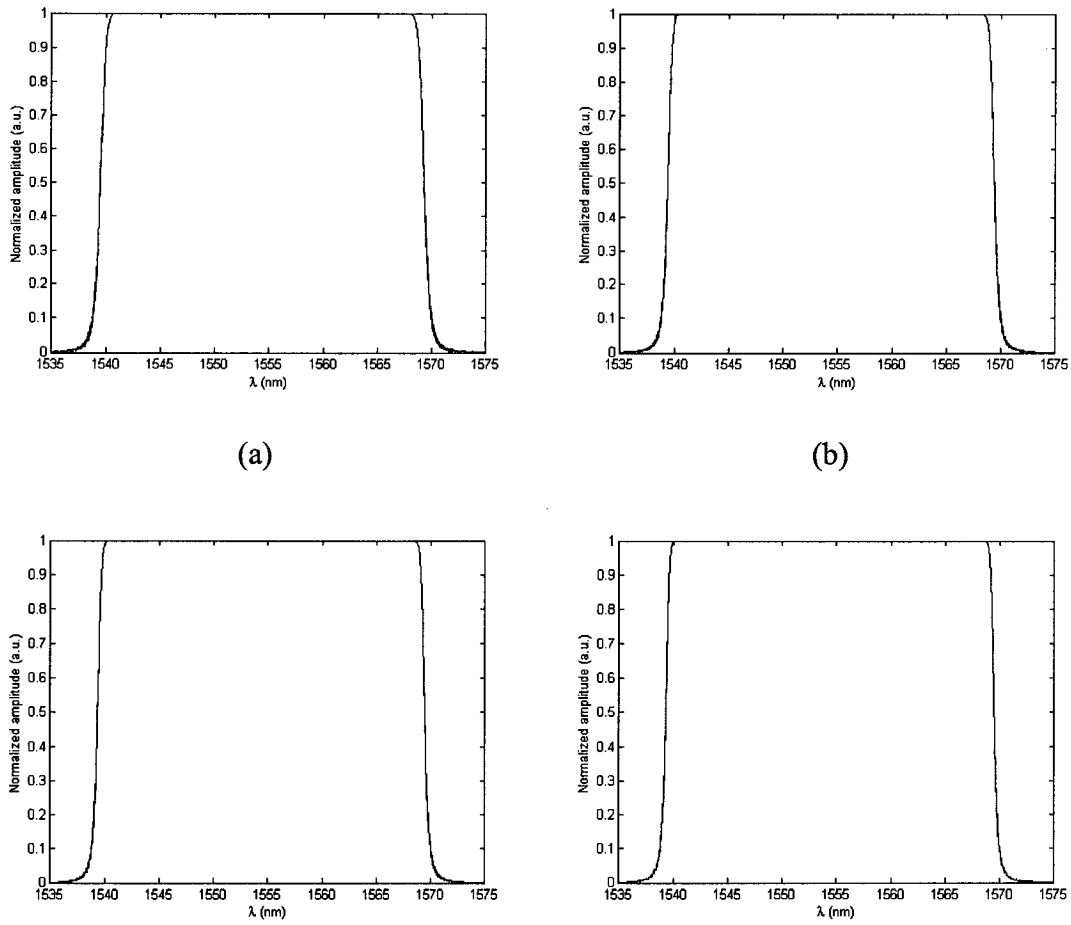

Fig. 5.18 Normalized amplitude of the microwave signal delayed by a chirped grating of length of (a) 10 mm, (b) 15 mm, (c) 20 mm and (d) 25 mm when ω_m = 18 GHz, an SSB modulation scheme is used and L = 25 km of single mode fiber.

When the length of the SMF is equal to 25 km, the same power penalty caused by the effects of the group delay ripple of the grating can be seen. On top of that, the effects of chromatic dispersion of the SMF can also be seen, which can be described similarly as the effects seen in Fig. 5.14. The difference is that in the case of 25 km of SMF with an electrical carrier frequency of 18 GHz, ten notches caused by the chromatic dispersion of the SMF can be

seen in the pass band of the chirped Bragg gratings. This worsens even more the overall operation of the beamformer as it reduces further the number of operable wavelength, thus the number of possible angles for the phased array antenna. Again, when an SSB modulation scheme is used, no power penalty is seen throughout the entire pass band of the chirped Bragg gratings.

When the single mode fiber has a length of 25 km, the angle of the main beam of the phased array antenna as a function of the optical carrier wavelength is displayed in Fig. 5.19.

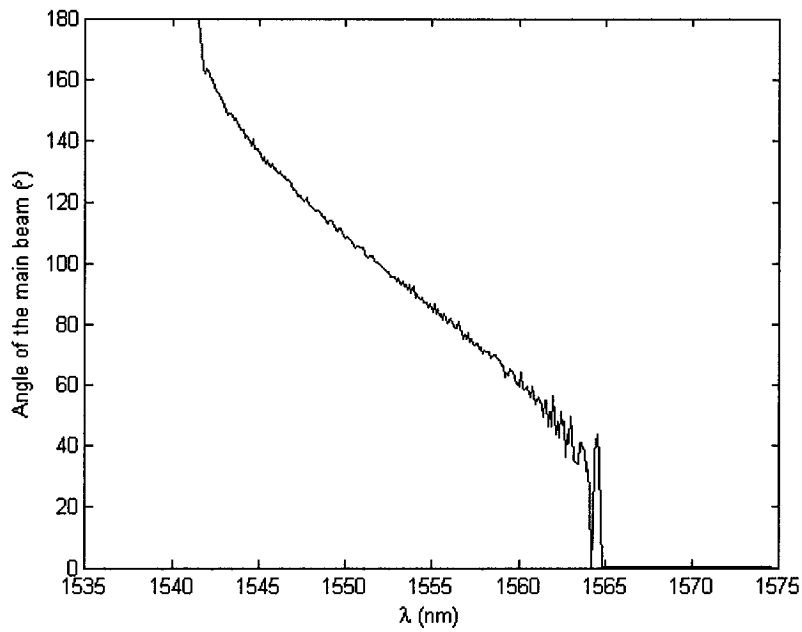

(a)

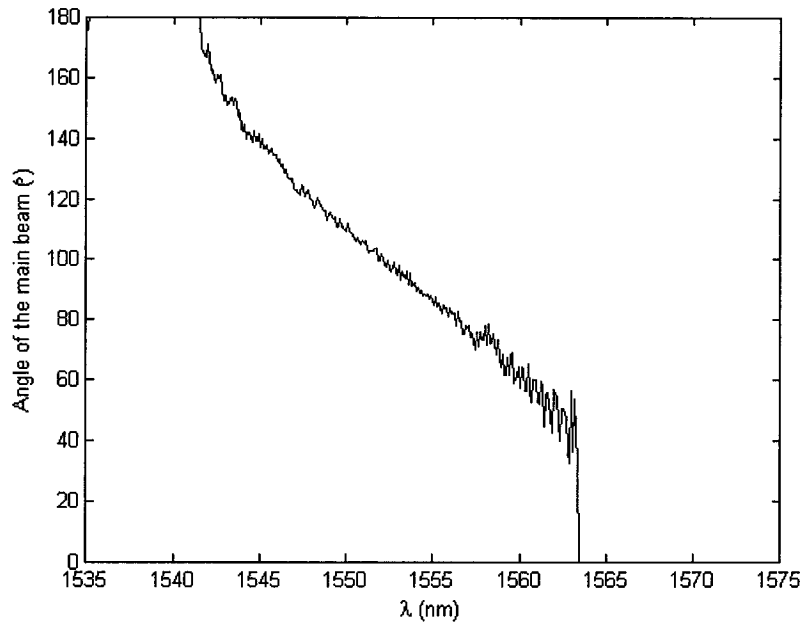

(b)

Fig 5.19 Angle of the main lobe of the phased array antenna when $\omega_m = 18$ GHz, $L = 25$ km and (a) double sideband- (b) single sideband- modulation is used.

If we analyze Figs. 5.13 (b), 5.16 (b) and 5.19 (b), we find that the curves are identical when an SSB modulation is used. Thus, the effects of chromatic dispersion are truly not affecting the operation of the beamformer in terms of the amplitude of the recovered microwave signal, but also in terms of the angle of the main lobe of the PAA for a given optical wavelength.

By studying the graphs presented in Fig 5.8 through Fig 5.19, we can arrive at the following conclusions:

1. The effects of the group delay ripple of the chirped gratings and the nonlinearity of the time delay responses as a function of the wavelength of the optical carrier are translated by an important power penalty at discrete wavelength for a fixed microwave carrier frequency when a double sideband modulation scheme is used.

2. The power of the recovered microwave signal is not affected by the group delay ripple when a single sideband modulation scheme is used.

3. The effects of the group delay ripple on the angle of the main lobe are not as significant when a double sideband modulation scheme is used that when a single sideband modulation scheme is used.

4. The effects of chromatic dispersion are very significant if a double sideband modulation scheme is used but are insignificant when a single sideband modulation scheme is used. The angle of the main lobe is not greatly affected by chromatic dispersion but the amplitude of the recovered microwave signal is greatly affected by the phenomenon.

Chapter 6

CONCLUSIONS AND FUTURE WORK

6.1 Conclusions

The three objectives of this research project were to design a waveguide-based Bragg grating prism for a true time-delay beamforming system, to realize such a waveguide Bragg prism composed of discrete Bragg gratings and to analyze the effects of chromatic dispersion on the performance of such a system. The first and last objectives have been successfully achieved, while the second objective would require another device to be made with adjusted grating center wavelengths in order to achieve a true waveguide Bragg grating prism. This could be achieved by illuminating the entire length of a grating with UV light in order to increase the average refractive index of the grating (the "dc" value) to shift the grating center to the desired value.

In Chapter 2, the theoretical models of phased array antennas were presented and the main equations characterizing these antennas were developed. The notions of true time delay and phase shifting were presented and the obvious advantages of the true time-delay method were listed. In the same chapter, the theory associated with Bragg gratings based on the coupled-mode theory was also introduced and simulation results of Bragg gratings were presented.

Chapter 3 detailed the true time-delay beamforming module used in this project. The theoretical models of the components of the beamformer were introduced. These components include the tunable laser source, the electro-optic modulator, the waveguide Bragg grating prism and the photodetector.

In Chapter 4, the experimental results of the implementation of the Bragg grating prism on integrated optical waveguide were presented. Fabrication issues were discussed and solutions to the problems encountered were detailed. In particular, the bi-directional coupling of the optical signal into and out of the planar optical waveguides to capture the reflection spectrum of the waveguide Bragg grating array was found to be problematic. Using a lensed fiber helped solving this problem. The Bragg grating prism realized consists of four delay lines each having three gratings appropriately positioned. The optical transmission and reflection spectrum of the delay lines were presented and the time delay progressions were measured using a network analyzer. Electrical characterization of the beamformer was also carried and the results were presented. Sources of problems and their respective solutions were discussed.

The effects of chromatic dispersion on a remotely controlled true time-delay beamforming module were investigated in Chapter 5. The simulation results of a photonic true time-delay technique using waveguide Bragg grating prism were presented. The Bragg grating prism was composed of chirped gratings of different lengths but of same total chirp in order to produce a true time-delay progression. Two modulation techniques were considered in the simulation. SSB modulation was shown to be well suited for broadband operations with little impact on the orientation of the mainlobe resulting from chromatic dispersion. When

DSB modulation was used, the effects of chromatic dispersion would lead to an important power penalty in the recovered microwave signal at discrete optical carrier frequencies when a fixed microwave carrier frequency was used.

6.2 Future work

In this research project, a discrete uniform Bragg grating prism was investigated and realized. The Bragg grating prism was composed of four delay lines, each having three uniform Bragg gratings. As previously stated, this configuration leads to a limited bandwidth in the microwave domain and only gives discrete beamforming capabilities. A chirped Bragg grating prism implemented in optical fibers has already been realized in the past [14] and offers a greater flexibility and more beamforming capabilities. Such a configuration could be implemented in planar integrated optical waveguides in order to benefit from the advantages of the waveguides over optical fiber, such as an increased stability with respect to environmental changes such as temperature and vibration and an overall smaller size.

Further integration of photonic components in the planar integrated optical waveguide could be pursued. Such components as the optical power splitter can be integrated instead of using external commercially available components. To achieve this integration, a photomask would need to be designed and realized specifically for this application.

The fabrication of a fully-integrated true time-delay beamformer would require some changes to the fabrication setup. A new phase mask holder would need to be designed and realized so that the entire plane where the wafer would be in close proximity to the phase mask would be free. Also, changes to the hydrogen loading system would need to be carried out in order to be able to load large wafers with hydrogen. Currently, the width of the wafer that can be used is limited by the diameter of the loading tubes to about 1 cm. The length of the tubes does not present a practical problem as they are several meters long.

Other contributions in this area include the development of a single-sideband modulation module allowing the elimination of the unwanted effects of chromatic dispersion present when a double sideband modulation scheme is used. Several configurations have already been proposed, but advances can still be made.

Further research concerning the optical source can be also carried out. One possible area of development involves the realization of a double wavelength laser. Using this configuration, the wavelength spacing of the laser would be equal to the wanted microwave carrier frequency. The modulating electrical signal would thus be at a baseband frequency, eliminating the need to have a microwave signal external-modulating the optical carrier. Using this scheme, the recovered electrical signal at the photodetector would be a modulated microwave signal.

BIBLIOGRAPHY

[1] O. Raz, R. Rotman, Y Danziger, and M. Tur, "Implementation of photonic true time delay using high-order-mode dispersion compensating fibers," IEEE Photonics Technology Letters, vol.16, no.5, pp.1367-1369, May 2004.

[2] D. Dolfi, D. Mongardien, S. Tonda, M. Schaller, and J. Chazelas, "Photonics for airborne phased array radars," IEEE International Conference on Phased Array Systems and Technology, pp.379-382, May 2000.

[3] R. A. Minasian and K. E. Alameh, "Optical-Fiber Grating-Based Beamforming Network for Microwave Phased Arrays," IEEE Trans. on Microwave Theory and Techniques, vol.45, no.8, pp.1513-1517, Aug. 1997.

[4] L. Xu, R. Taylor, and S. R. Forrest, "The use of optically coherent detection techniques for true-time delay phased array and systems," Journal of Lightwave Technology, vol.13, no.8, pp.1663-1678, Aug. 1995.

[5] Y. Chen and R. T. Chen, "A Fully Packaged True Time Delay Module for a K-band Phased Array Antenna System Demonstration," IEEE Photonic Technology Letters, vol.14, no.8, pp.1175-1177, Aug. 2002.

[6] D. N. McQuiddy, Jr., R. L. Gassner, P. Hull, J. S. Mason, and J.M. Bedinger, "Transmit/receive module technology for X-band active array radar," Proceedings of the IEEE, vol.79, no.3, pp.308-341, Mar. 1991

[7] R. Rotman, O. Raz, and M. Tur, "Requirements for True Time Delay Imaging Systems with Photonic Components," IEEE International Symposium on Phased Array Systems and Technology, pp.193-198, Oct. 2003.

[8] P. M. Freitag and S. R. Forrest, "A coherent optically controlled phased array antenna system," IEEE Microwave and Guided Wave Letters, vol.3, no.9, pp.293-295, Sept. 1993.

[9] W. Ng, A. A. Walston, G. L. Tangonan, J. J. Lee, I. L. Newberg, and N. Bernstein, "The first demonstration of an optically steered microwave phased array antenna using true-time-delay," IEEE Journal of Lightwave Technology, vol.9, no.9, pp.1124-1131, Sept. 1991.

[10] I. Y. Lee, K. H. Lee, D. Y. Kim, Y. Y. Kim, and J. H. Yea, "A novel compact multi line phase shifter for precise array antenna beam control," IEEE MTT-S International Microwave Symposium Digest , vol.3, pp.1773-1776, June 2004.

[11] R. S. Chu, K. M. Lee, and A. T. S Wang, "Multiband phased-array antenna with interleaved tapered-elements and waveguide radiators," Antennas and Propagation Society International Symposium, vol.3, pp.1616-1619, July 1996.

[12] S. Tang, R. T. Chen, B. Li, and J. Foshee, "Waveguides Take to the Sky," IEEE Circuits and Devices Magazine, vol.16, no.1, pp.10-16, Jan. 2000.

[13] S. S. Lee, Y. H. Oh, and S. Y. Shin, "Photonic microwave true-time delay based on a tapered fiber Bragg grating with resistive coating," IEEE Photonic Technology Letters, vol.16, no.10, pp.2335-2337, Oct. 2004.

[14] Y. Liu and J. P. Yao "Wideband true time-delay beamformer employing a tunable chirped fiber grating prism," Applied Optics, vol.42, no.13, pp.2273-2277, May 2003.

[15] Y. Wang, S. C. Tjin, J. Yao, J. P. Yao, L. He, and K. A. Ngoi, "Wavelength-switching fiber laser for optically controlled phased-array antenna," Optics Communications, Elsevier Science, vol.211, no.1-6, pp.147-151, Oct. 2002.

[16] Y. Liu, J. Yang, and J. P. Yao, "Continuous true-time-delay beamforming for phased array antenna using a tunable chirped fiber grating delay line," IEEE Photonics Technology Letters, vol.14, no.8, pp.1172 -1174, Aug. 2002.

[17] J. Yang, Y. Liu, S. Tjin, and J.P. Yao, "Continuous True-Time-Delay System Employing a Novel Tunable Chirped Fiber Grating Delay Line and a Sampled Grating Based Multiwavelength Fiber Laser," International Journal of Infrared and Millimeter Waves, vol. 23, no.8, pp.1241-1250, Aug. 2002.

[18] Y. Liu, J. P. Yao, and J. Yang, "Wideband true-time-delay unit for phased array beamforming using discrete-chirped fiber grating prism," Optics Communications, Elsevier Science, vol.207, no.1-6, pp.177-187, June 2002.

[19] B. Vidal, D. Madrid, J. L. Corral, V. Polo, A. Martinez, J. Hendrik den Besten, F. Soares, J. Marti, and M. K. Smit, "Photonic True-Time Delay Beamformer for Broadband Wireless Access Network at 40 GHz Band," IEEE MTT-S International Microwave Symposium Digest , vol.3, pp.1949-1952, June 2002.

[20] S.T. Winnall and D.B. Hunter, "A fibre Bragg grating based scanning receiver for electronic warfare applications," International Topical Meeting on Microwave Photonics, pp.211-214, Jan. 2002.

[21] G. Y. Lee, Y. B. Choi, J. D. Shin, B. G. Kim, and S. B. Lee, "Optical true time-delay feeder for linear phased-array antennas implemented with chirped fiber gratings," The 14th Annual Meeting of the IEEE Lasers and Electro-Optics Society, vol.1, pp.255-256, Nov. 2001.

[22] B. Ortega, J. L. Cruz, J. Capmany, M. V. Andrés, and D. Pastor, "Analysis of a Microwave Time Delay Line Based on a Perturbed Uniform Fiber Bragg Grating Operating at Constant Wavelength," Journal of Lightwave Technology, vol.18, no.3, pp.430-436, Mar. 2000.

[23] J. L. Corral, J. Marti, J. M. Fuster, and R. I. Laming, "True time-delay scheme for feeding optically controlled phased-array antennas using chirped-fiber gratings," IEEE Photonic Technology Letters, vol.9, no.11, pp.1529-1531, Nov. 1997.

[24] J. L. Corral, J. Marti, J. Capmany, R. I. Laming, and M. J. Cole, "True Time Delay Scheme For Continuous Optical Control Of Phased Array Antennas Employing Chirped Fiber Gratings," IEEE 27th European Microwave Conference and Exhibition, vol.2, pp.1228-1233, Sept. 1997.

[25] A. Molony, Z. Lin, J. A. R. Williams, I. Bennion, C. Edge, and J. Fells, "Fiber Bragg-grating true time-delay systems: discrete-grating array 3-b delay lines and chirped-grating 6-b delay lines," IEEE Trans. on Microwave Theory and Techniques, vol.45, no.8, pp.1527-1530, Aug. 1997.

[26] A. Molony, L. Zhang, J. A. R. Willams, I. Bennion, C. Edge, and J. Fells, "Fiber Bragg grating networks for time-delay control of phased-array antennas," Summaries of papers presented at the Conference on Lasers and Electro-Optics, pp.244-245, June 1996.

[27] L. Xu, R. Taylor, and S. R. Forrest, "True Time-Delay Phased-Array Antenna Feed System Based on Optical Heterodyne Techniques," IEEE Photonic Technology Letters, v.8, no.1, pp.160-162, Jan. 1996.

[28] I. Frigyes and A. J. Seeds, "Optically generated true-time delay in phased-array antennas," IEEE Trans. on Microwave Theory and Techniques, vol.43, no.9, pp.2378-2386, Sept. 1995.

[29] G.A. Ball, W. H. Glenn, and W. W. Morey, "Programmable fiber optic delay line," IEEE Photonic Technology Letters, vol.6, no.6, pp.741-743, Jun. 1994.

[30] R. D. Esman, M. Y. Frankel, J. L. Dexter, L. Goldberg, M. G. Parent, D. Stilwell, and D. G. Cooper, "Fiber-optic prism true time-delay antenna feed," IEEE Photonic Technology Letters, vol.5, no.11, pp.1347-1349, Nov. 1993.

[31] I. L. Newberg, C. M. Gee, G. D. Thurmond, and H. W. Yen, "Long microwave delay fiber-optic link for radar testing," IEEE Transactions on Microwave Theory and Techniques, vol.38, no.5, pp.664-666, May 1990.

[32] D. Dolfi, P. Joffre, J. Antoine, J. P. Huignard, D. Philippet, and P. Granger, "Experimental demonstration of a phased-array antenna optically controlled with phase and time delays," Applied Optics, vol.35, no.26, pp.5293-5300, Sept. 1996.

[33] D. Dolfi, P. Joffre, J. Antoine, J. P. Huignard, D. Philippet, P. Granger, and J. Chazelas, " Photonics for phased array radars," SPIE Optical Technology for Microwave Applications VII, vol.2560, pp.158-165, Oct. 1995.

[34] E. H. Monsay, K. C. Baldwin, and M. J. Caccuitto, "Photonic True Time Delay for High-Frequency Phased Array Systems," IEEE Photonic Technology Letters, v.6, no.1, pp.118-120, Jan. 1994.

[35] P. J. Matthews, M. Y. Frankel, and R. D. Esman, "A wide-band fiber-optic true-time-steered array receiver capable of multiple independent simultaneous beams," IEEE Photonics Technology Letters, vol.10, no.5, pp.722-724, May 1998.

[36] D. T. K. Tong and M. C. Wu, "Multiwavelength optically controlled phased-array antennas," IEEE Transactions on Microwave Theory and Techniques, vol.46, no.1, pp.108-115, Jan. 1998.

[37] K. Horikawa, I. Ogawa, and T. Kitoh, "Photonic Switched True Time Delay Beam Forming Network Integrated on Silica Waveguide Circuits," IEEE MTT-S International Microwave Symposium Digest, vol.1, pp.65-68, May 1995.

[38] W. Ng, A. Walson, G. Tangonan, J. J. Lee, and I. Newberg, "Optical steering of dual band microwave phased array antenna using semiconductor laser switching," Electronics Letters, vol.26, no.12, pp.791-793, June 1990.

[39] D. T. K. Tong and M. C. Wu, "Common transmit/receive module for multiwavelength optically controlled phased array antennas," Optical Fiber Communication Conference and Exhibit, pp.354-355, Feb. 1998.

[40] R. D. Esman, J. J. Monsma, J. L. Dexter, and D. G. Cooper, "Microwave true time-delay modulator using fibre-optic dispersion," Electronics Letters, vol.28, no.20, pp.1905-1908, Sept. 1992.

[41] J. Yao, J. Yang, and Y. Liu, "Continuous True-Time-Delay Beamforming Employing a Multiwavelength Tunable Fiber Laser Source," IEEE Photonic Technology Letters, vol.14, no.5, pp.687-689, May. 2002.

[42] J. Yang, Y. Liu, and J. Yao, "Wideband true-time-delay system using fiber Bragg grating prism incorporated with a wavelength tunable fiber laser source," International Topical Meeting on Microwave Photonics, pp.125-128, Jan. 2002.

[43] B. Ortega, J. L. Cruz, J. Capmany, M. V. Andrés, and D. Pastor, "Variable Delay Line for Phased-Array Antenna Based on a Chirped Fiber Grating," IEEE

Transactions on Microwave Theory and Techniques, vol.48, no.8, pp.1352-1360, Aug. 2000.

[44] J. J. Pan and Y. Shi, "Fiber Bragg grating for phased-array systems," IEEE Antennas and Propagation Society International Symposium, vol.2, pp.751-754, Jul. 1997.

[45] H. Zmuda, R. A. Soref, P. Payson, S. Johns, and E. N. Toughlian, "Photonic Beamformer for Phased Array Antennas Using a Fiber Grating Prism," IEEE Photonic Technology Letters, vol.9, no.2, pp.241-243, Feb. 1997.

[46] A. Molony, C. Edge, and I. Bennion, "Fibre grating time delay element for phased array antennas," Electronics Letters, vol.31, no.17, pp.1485-1486, Aug. 1995.

[47] J. M. Jouanno, J. Hubner, J. E. Pedersen, R. Kromann, T. Feuchter, and M. Kristensen, "Strong Bragg gratings for WDM devices in non-sensitised low-loss Ge-doped waveguides," Electronics Letters, vol.32, no.23, pp.2151-2152, Nov. 1996.

[48] R. C. Hansen, "Phased Array Antennas," John Wiley & Sons, Inc., New York, USA, 1998.

[49] T. Y. Yun and K. Chang, "A low-cost 8 to 26.5 GHz phased array antenna using a piezoelectric transducer controlled phase shifter," IEEE Transactions on Antennas and Propagation, vol.49, no.9, pp.1290-1298, Sept 2001.

[50] R. R. Romanofsky, J. T. Bernhard, F. W. van Keuls, F. A. Miranda, G. Washington, and C. Canedy, "K-band phased array antennas based on $Ba_{0.60}Sr_{0.40}$ TiO_3 thin-film phase shifters," IEEE Transactions on Microwave Theory and Techniques, vol.48, no.12, pp.2504-2510, Dec. 2000.

[51] W. T. Joines, "A Continuously Variable Dielectric Phase Shifter," IEEE Transactions on Microwave Theory and Techniques, vol.19, no.8, pp.729-732, Aug. 1971.

[52] K. O. Hill and G. Meltz, "Fiber Bragg Grating Technology Fundamentals and Overview," Journal of Lightwave Technology, vol.15, no.8, pp.1263-1276, Aug. 1997.

[53] B. S. Kawasaki, K. O. Hill, D. C. Johnson, and Y. Fujii, "Narrow-band Bragg reflectors in optical fibers," Optics Letters, vol.3, no.2, pp.66-68, Aug. 1978.

[54] K. O. Hill, Y. Fujii, D. C. Johnson, and B. S. Kawasaki, "Photosensitivity in optical fiber waveguides: application to reflection fiber fabrication," Applied Physics Letters, vol.32, no.10, pp.647-649, May 1978.

[55] G. Meltz, W. W. Morey, and W. H. Glenn, "Formation of Bragg gratings in optical fibers by a transverse holographic method," Optics Letters, vol.14, no.15, pp.823-825, Aug. 1989.

[56] R. Kashyap, "Fiber Bragg Gratings," Academic Press, California, USA, 1999.

[57] M. McCall, "On the application of coupled mode theory for modeling fiber Bragg gratings," Journal of Lightwave Technology, vol.18, no.2, pp.236-242, Feb. 2000.

[58] T. Erdogan, "Fiber Grating Spectra," Journal of Lightwave Technology, vol.15, no.8, pp.1277-1294, Aug. 1997.

[59] A. Carballar and M. A. Muriel, "Phase reconstruction from reflectivity in fiber Bragg gratings," Journal of Lightwave Technology, vol.15, no.8, pp.1314-1322, Aug. 1997.

[60] A. Yariv, "Coupled-mode theory for guided-wave optics," IEEE Journal of Quantum Electronics, vol.QE-9, no.9, Sept. 1973.

[61] H. G. Fröhlich and R. Kashyap, "Two methods of apodisation of fibre-Bragg-gratings," Optics Communications, vol.157, no.1-6, pp.273-281, Dec. 1998.

[62] R. Kashyap, A. Swanton, and D. J. Armes, "Simple technique for apodising chirped and unchirped fibre Bragg gratings," Electronics Letters, vol.32, no.13, pp.1226-1228, Jun. 1996.

[63] J. Albert, K. O. Hill, B. Malo, S. Theriault, F. Bilodeau, D. C. Johnson, and L. E. Erickson, "Apodisation of the spectral response of fibre Bragg gratings using a phase mask with variable diffraction efficiency," Electronics Letters, vol.31, no.3, pp.222-223, Feb. 1995.

[64] B. Malo, S. Thériault, D. C. Johnson, F. Bilodeau, J. Albert, and K. O. Hill, "Apodised in-fibre Bragg grating reflectors photoimprinted using a phase mask," IEEE Electronic Letters, vol.31, no.3, pp.223-225, Feb. 1995.

[65] M. Matsuhara and K. O. Hill, "Optical-Waveguide Band-Rejection Filters: Design," Applied Optics, vol.13, no.12, pp.2886-2888, Dec. 1974.

[66] K. O. Hill, "Aperiodic Distributed-Parameter Waveguides for Integrated Optics," Applied Optics, vol.13, no.8, pp.1853-1856, Aug. 1974.

[67] P. Fernandez, F. Alonso, J. C. Aguado, I. de Miguel, F. Gonzalez, J. Blas, J. Duran, R. Lorenzo, E. Abril, and M. Lopez, "Simulation and design tool for spectral characterization of fiber Bragg gratings," Proceedings of the 2002 4th International Conference on Transparent Optical Networks, vol.2, pp.57-60, Apr. 2002.

[68] J. Ciosmak and M. Marciniak, "Impact of apodisation on fiber Bragg grating reflection and phase responses," Proceedings of the 3rd International Conference on Transparent Optical Networks, pp.287-290, Jun. 2001.

[69] S. J. Mihailov, F. Bilodeau, K. O. Hill, D. C. Johnson, J. Albert, and A. S. Holmes, "Apodization Technique for Fiber Grating Fabrication with a Halftone Transmission Amplitude Mask," Applied Optics, vol.39, no.21, pp.3670-3677, Jul. 2000.

[70] V. Mizrahi and J. E. Sipe, "Optical properties of photosensitive fiber phase gratings," Journal of Lightwave Technologies, vol.11, no.10, pp.1513-1517, 1993.

[71] J. Capmany, M. A. Muriel, S. Sales, J. J. Rubio, and D. Pastor, "Microwave V-I transmission matrix formalism for the analysis of photonic circuits: application to fiber Bragg gratings," Journal of Lightwave Technology, vol. 21, no.12, pp.3125-3134, Dec. 2003.

[72] P. D. Lungu, "Transfer matrix method used for numerical simulation of the Bragg reflector at perpendicular incidence of the incident field," 1995 International Semiconductor Conference CAS'95, pp.613-616, Oct. 1995.

[73] M. Yamada and K. Sakuda, "Analysis of almost-periodic distributed feedback slab waveguide via a fundamental matrix approach," Applied Optics, vol. 26, no.16, pp. 3474-3478, 1987.

[74] F. Bilodeau, B. Malo, J. Albert, D. C. Jonson, and K. O. Hill, "Photosensitization of optical fiber and silica-on-silicon/silica waveguides," Optics Letters, vol.18, no.12, pp.953-955, Jun. 1993.

[75] S. J. Mihailov, C. W. Smelser, D. Grobnic, R. B. Walker, P. Lu. H. Ding, and J. Unruh, "Bragg gratings written in all-SiO/sub 2/ and Ge-doped core fibers with 800-nm femtosecond radiation and a phase mask," Journal of Lightwave Technology, vol.22, no.1, pp.94-100, Jan. 2004.

[76] K. O. Hill, B. Malo, F. Bilodeau, D. C. Johnson, and J. Albert, "Bragg gratings fabricated in monomode photosensitive optical fiber by UV exposure through a phase mask," Applied Physics Letters, vol.62, no.10, pp.1035-1037, Mar. 1993

[77] M. Gotoda, T. Nishimura, and Y. Tokuda, "A Widely Tunable SOA-Integrated DBR Laser by Combination of Sampled and Superstructure Gratings," Journal of Lightwave Technology, vol.23, no.7, pp.2331-2336, Jul. 2005.

[78] S. K. Oh, J. M. Lee, K. S. Kim, C. W. Lee, H. Ko, S. Park, and M. H. Park, "Fabrication of wavelength-tunable butt-coupled sampled grating DBR lasers using planar buried heterostructure," IEEE Photonics Technology Letters, vol.15, no.12, pp.1680-1682, Dec. 2003

[79] G. Liu, W. Wang, J. Zhang, X. Wang, W. Chen, and H. Zhu, "Wavelength tunable electroabsorption modulated DFB laser with thin film heater," Lasers and Electro-Optics Society 2000 Annual Meeting, vol.2, pp.504-505, Nov. 2000.

[80] A. Hsu, S. L. Chuang, and T. Tanbun-Ek, "Tunable dual-mode operation in a chirped grating distributed-feedback laser," IEEE Photonics Technology Letters, vol.12, no.8, pp.963-965, Aug. 2000.

[81] N. Chen, Y. Nakano, K. Okamoto, K. Tada, G. I. Morthier, and R. G. Baets, "Analysis, fabrication, and characterization of tunable DFB lasers with chirped gratings", IEEE Journal of Selected Topics in Quantum Electronics, vol.3, no.2, pp.541-546, Apr. 1997.

[82] Y. Tohmori, Y. Yoshikuni, H. Ishii, F. Kano, T. Tamamura, Y. Kondo, and M. Yamamoto, "Broad-range wavelength-tunable superstructure grating (SSG) DBR lasers," IEEE Journal of Quantum Electronics, vol.29, no.6, pp.1817-1823, Jun. 1993.

[83] J. D. Berger, Y. Zhang, J. D. Grade, H. Lee, S. Hrinya, H. Jerman, A. Fennema, A. Tselikov, and D. Anthon, "Widely tunable external cavity diode laser using a MEMS electrostatic rotary actuator," Digest of the LEOS Summer Topical Meetings, pp.41-42, Aug. 2001.

[84] M. Uemukai, T. Suhara, K. Yutani, N. Shimada, Y. Fukumoto, H. Nishihara, and A. Larsson, "Tunable external-cavity semiconductor laser using monolithically integrated tapered amplifier and grating coupler for collimation," IEEE Photonics Technology Letters, vol.12, no.12, pp.1607-1609, Dec. 2000.

[85] C. J. Chang-Hasnain, "Tunable VCSELs," IEEE/LEOS International Conference on Optical MEMS, pp.77-78, Aug. 2000.

[86] Y.M. Li, W. Yuen, G. S. Li, and C. J. Chang-Hasnain, "Top-emitting micromechanical VCSEL with a 31.6-nm tuning range," IEEE Photonics Technology Letters, vol.10, no.1, pp.18-20, Jan. 1998.

[87] E. C. Vail, G. S. Li, W. Yuen, and C. J. Chang-Hasnain, "High performance micromechanical tunable vertical cavity surface emitting lasers," Electronics Letters, vol.32, no.20, pp.1888-1889, Sept. 1996.

[88] J. Yang, S. C. Tjin, and N. Q. Ngo, "Multiwavelength Tunable Fiber Ring Laser Based on Sampled Chirp Fiber Bragg Grating," IEEE Photonics Technology Letters, vol.16, no.4, pp.1026-1028, Apr. 2004.

[89] J. Yang, J. P. Yao, Y. Liu, and S.C. Tjin, "Continuous true-time-delay beamforming employing a tunable multiwavelength fiber ring laser source with equally increased or decreased wavelength spacing," Optical Engineering, vol.42, no.1, pp.239-244, Jan. 2003.

[90] J. Yang, J. P. Yao, K. Zhou, and Y. Liu, "Wideband wavelength tunable fiber ring laser with flattened output power spectrum," Optics Communications, vol.210, no.3-6, pp.147-152, Sept. 2002.

[91] M. Bass and E. W. Van Stryland, "Fiber Optics Handbook," McGraw-Hill, New York, USA, 2002.

[92] H. Al-Raweshidy and S. Komaki, "Radio over Fiber Technologies for Mobile Communications Networks," Artech House, Maine, USA, 2002.

[93] F. T. S. Yu, S. Jutamulia, and S. Yin, "Introduction to information optics," Academic Press, San Diego, USA, 2001.

[94] G. Keiser, "Optical Fiber Communications," Third edition, McGraw-Hill, New York, USA, 2000.

[95] R. Scarmozzino, A. Gopinath, R. Pregla, and S. Helfert, "Numerical techniques for modeling guided-wave photonic devices," IEEE Journal of Selected Topics in Quantum Electronics, vol.6, no.1, pp.150-162, 2000.

[96] W. P. Huang and C. L. Xu, "Simulation of three-dimensional optical waveguides by a full-vector beam propagation method," IEEE Journal of Quantum Electronics, vol.29, no.10, pp.2639-2649, Oct. 1993.

[97] D. Yevick and B. Hermansson, "Efficient beam propagation techniques," IEEE Journal of Quantum Electronics, vol.26, no.1, pp.109-112, Jan. 1990.

[98] T. B. Koch, J. B. Davies, and D. Wickramasinghe, "Finite element/finite difference propagation algorithm for integrated optical device," Electronics Letters, vol.25, no.8, pp.514-516, Apr. 1989

[99] M. D. Feit and J. A. Jr. Fleck, "Light propagation in graded-index optical fibers," Applied Optics, vol.17, no.24, pp.3990-3998, Dec. 1978.

[100] A. Othonos and K. Kalli, "Fiber Bragg gratings: Fundamentals and applications in telecommunications and sensing," Artech House, Boston-London, 1999.

[101] H. Murata, K. Kaneda, and Y. Okamura, "38 GHz optical single-sideband modulation by using guided-wave electrooptic modulators with periodic polarization-reversal," IEEE Conference on Lasers and Electro-Optics, vol.2, May 2004.

[102] C. Marra, A. Nirmalathas, D. Novak, C. Lim, L. Reekie, J. A. Besley, and N. J. Baker, "Optical SSB Modulation using Fiber Bragg Gratings and the Impact of Grating Dispersion on Transmission Performance," IEEE International Topical Meeting on Microwave Photonics, pp.93-96, Jan. 2002.

[103] L. T. Nichols and R. D. Esman, "Single sideband modulation techniques and applications," IEEE Optical Fiber Communication Conference, vol.3, pp.332-334, Feb. 1999.

[104] G. H. Smith, D. Novak, and Z. Ahmed, "Technique for optical SSB generation to overcome dispersion penalties in fiber-radio systems," Electronics Letters, vol.33, no.1, pp.74-75, Jan. 1997.

[105] K. Yonenaga and N. Takachio, "A Fiber Chromatic Dispersion Compensation Technique with an Optical SSB Transmission in Optical Homodyne Detection Ssytems," IEEE Photonics Technology Letters, vol.5, no.8, pp.949-951, Aug. 1993.

[106] G. Meslener, "Chromatic dispersion induced distortion of modulated monochromatic light employing direct detection," IEEE Journal of Quantum Electronics, vol.20, no.10, pp.1208-1216, Oct. 1984.

[107] K. Hinton, "Dispersion compensation using apodized Bragg fiber gratings in transmission," Journal of Lightwave Technology, vol.16, no.12, pp.2336-2346, Dec. 1998.

[108] G. H. Smith, D. Novak, and Z. Ahmed, "Overcoming chromatic-dispersion effects in fiber-wireless systems incorporating external modulators," IEEE Transactions on Microwave Theory and Techniques, vol.45, no.8, part 2, pp.1410-1415, Aug. 1997.

[109] N. M. Litchinitser, B. J. Eggleton, and D. B. Patterson, "Fiber Bragg gratings for dispersion compensation in transmission: theoretical model and design criteria for

nearly ideal pulse recompression," Journal of Lightwave Technology, vol.15, no.8, pp.1303-1313, Aug. 1997.

[110] J. Park, A. F. Elrefaie, and K. Y. Lau, "Fiber chromatic dispersion effects on multichannel digital millimeter-wave transmission," IEEE Photonics Technology Letters, vol.8, no.12, pp.1716-1718, Dec. 1996.

[111] U. Gliese, S. Norskov, and T. N. Nielsen, "Chromatic dispersion in fiber-optic microwave and millimeter-wave links," IEEE Transactions on Microwave Theory and Techniques, vol.44, no.10, part 1, pp.1716-1724, Oct. 1996.

[112] E. Jaunart, P. Crahay, P. Megret, J. C. Froidure, M. Lamquin, and M. Blondel, "Chromatic dispersion modeling of single-mode optical fibers: a detailed analysis," Journal of Lightwave Technology, vol.12, no.11, pp.1910-1915, Nov. 1994.